University of Alberta

Eigenstructure Analysis

by

Sharareh Karmand ©

A thesis submitted to the Faculty of Graduate Studies and Research in partial fulfillment of the requirements for the degree of **Master of Science**

in

Geophysics

Department of Physics

Edmonton, Alberta
Spring 2007

Canada

to

Arash & *Kurosh*

for all glorious days and nights

Abstract

This thesis aims to address two major problems in geophysical data processing: a) noise attenuation and (b) spatia-temporal spectral analysis of geophysical wavefields.

In order to enhance the signal-to-noise ratio of multichannel time series I propose methods that exploit the ability of the Singular Value Decomposition to extract coherent information from multi-channel data. In particular, I describe techniques to improve the signal-to-noise ratio of 2D and 3D seismic data sets.

In the second part I developed an algorithm based on the multiple signal classification method to retrieve high resolution estimates of the frequency-wavenumber energy distribution of shear Alfvén waves recorded by the SuperDARN radars network. This method allows us to estimate phase velocity of shear Alfvén waves and retrieve information to constraint physical models that describe field line resonance (FLR) phenomena occurred in the Earth's magnetosphere.

Acknowledgements

I wish to acknowledge Prof. Mauricio D. Sacchi and Dr. Frances R. Fenrich for their patient, great scientific contributions and helpful advices during the course of this thesis.

I would also thank to other members of committee Prof. Zoltan Koles and Dr. Yu Jeffrey Gu for their careful reading of the thesis and useful suggestions.

I should also thank my friends Mostafa Naghizadeh, Sam Kaplan, Somnath Misra, Ebrahim Fathi for their fruitful discussions.

Finally, my special thank goes to my husband Vahid Rezania for his courage and support during my study.

Contents

List of Tables

List of Figures

List of symbols

Symbol	Description
$()^*$	Complex conjugate
$()^T$	Matrix transpose
$()^H$	Matrix transpose and complex conjugate
α	Slope of the event relative to the x-direction
β	Slope of the event relative to the y-direction
$\gamma(\tau)$	Autocovariance function
$\tilde{\gamma}(\tau)$	Estimated autocovariance function
Γ	Adiabatic index
λ	Eigenvalue $(= \sigma^2)$
ρ	Plasma density
ϵ	Least square error
Σ	Matrix of singular values
σ	Singular value
$\{\xi_\tau\}$	The lag window
$\mathbf{B}$	Magnetic field vector
B	Magnetic field strength
C_s	Adiabatic sound speed
$\mathbf{d}$	Trace vector
$E\{\ \}$	Expectation value
$\mathcal{E}$	Total energy
$\mathbf{e}$	Noise vector
$f(\omega)$	Periodogram
$\tilde{f}(\omega)$	Estimated periodogram
$\mathbf{I}$	Identity matrix
L	Number of events
M	Number of offset points

M_x	Number of x-offset points
M_y	Number of y-offset points
N	Number of time points
N_f	Nyquist frequency
p	Plasma pressure
$\mathbf{R}$	Data covariance matrix
$\widehat{\mathbf{R}}$	Smoothed covariance matrix
R_E	Earth's radius
SNR	Signal-to-noise ratio
$s(t)$	Signal
$\mathbf{U}$	The left singular matrix
$\widehat{\mathbf{U}}$	Smoothed matrix
$\mathbf{V}$	The right singular matrix
V_A	Alfven speed
$\mathbf{u}$	Eigenvector of $\mathbf{XX}^H$
$\mathbf{v}$	Eigenvector of $\mathbf{X}^H\mathbf{X}$
$w(t)$	Wavelet
$\mathbf{X}$	Data matrix
$\widetilde{\mathbf{X}}$	Reconstructed (estimated) data matrix
$\mathbf{X}_\omega$	Fourier transformed data matrix
$\widetilde{\mathbf{X}}_\omega$	Reconstructed Fourier transformed data matrix
x	x-offset
y	y-offset
$\mathbf{Y}$	Data matrix

Chapter 1

Introduction

Statistical methods for signal processing and data analyzing have a wide range of applications, such as economics, medical physics, geophysics, astrophysics, etc. However, the objectives are often the same, namely, the extraction of parameters of interest from noisy observations.

A very common feature of seismic or astrophysics time series that singles it out from those occurring in other fields, is its very poor quality. A typical large seismic survey may be carried out in a place that has varying conditions, such as environmental and demographic restrictions, weather conditions, etc., that can have a significant impact on the data quality. In order to get some physical information from the raw data a time series analysis is required. For example, implementing a Fourier transformation to analyze significant periodicity in the raw data, and enhancing or attenuating a particular frequency by applying deterministic filters.

No matter how our instruments are sophisticated and precise, the experimental measurements are never perfect. In general, any measurement is contaminated with two types of errors: random noise and systematic error. Random noise is statistical fluctuations in the measured data due to the precision limitations of the equipment. Random errors usually result from the experimenter's inability to take the same measurement in exactly the same way to get exact the same number. Random noise is unpredictable. Systematic errors, by contrast, are reproducible inaccuracies that are often due to a problem which persists throughout the entire experiment.

The quality of a signal is usually expressed by a quantity called the signal-to-noise ratio (SNR), which is the ratio of the amplitude of the signal to the standard deviation of the noise. The greater the ratio, the less noise in the observed data.

In data processing, enhancing the SNR is a central issue. The fact that really

distinguishes signal from random noise is that the noise is not reproducible. Random noise is not the same from one measurement to the next. The real signal, however, is at least partially reproducible. So by measuring the signal for several times and adding up all the measurements point-by-point, one can enhance the SNR ratio significantly. This is called ensemble averaging. In seismology, the measurements are usually done with an array of geophones (detectors) placed in a line (2D observation) or distributed in an area (3D observation). Note that each observation includes a time component. Adding all observations from each geophone in the array together will diminish the random noise and improve common signals among them. In seismology, this process is called stacking and it enhances the SNR of the data. In general situations, however, enhancing the SNR of a data structure is not a simple task. Several methods are known to enhance the signal-to-noise ratio, such as

- *Principal Components Analysis* (PCA) that attempts to determine a smaller set of synthetic variables or factors from the original set of variables and then reconstruct the data structure with the smaller set (Anderson, 1958).

- *Singular Value Decomposition* (SVD) that separates a matrix into its eigenimages in order to get matrices with rank 1 (Lanczos, 1961). The Singular Value Decomposition is a widely used technique that decomposes a matrix into several rank 1 matrices to expose many of the useful and interesting properties of the original matrix. We will discuss this method in more detail in Chapter 2.

- *Karhunen-Loeve Transformation* (KLT) that is the orthogonal transform for signal representation with minimum mean-square error (Hemon and Mace, 1978).

Since the above methods are based on the eigenvectors and eigenvalues of the covariance matrix of the data, they are usually called the eigenvector, eigenstructure or eigenimage methods. It is shown by several investigators that PCA, SVD and KLT have a very powerful noise reduction capabilities under the right conditions (Huang and Narendra, 1975; Andrews and Patterson, 1976; Jones and Levy, 1987; Done et al., 1991). This follows from the fact that the decomposed eigenimages can be used to map the observed data into two signal and noise subspaces that are orthogonal to each other. As a result, the whole data with greater SNR value can be recovered from the signal subspace. For a highly correlated data structure, for

example, a large percentage of the signal maps into one eigenimage (corresponding to the largest eigenvalue of data covariance matrix) only. Therefore, the whole data can be reconstructed with bigger SNR value using the information stored in this eigenimage.

The eigenimage techniques are frequently applied to a variety of seismic data processing problems. Following Hemon and Mace (1978) who were the first investigators that introduced and applied KLT to seismic data, the KLT transformation has been applied to one- and two-dimensional data compression by several authors. Levy et al. (1983) and Ulrych et al. (1983) extended the work done by Hemon and Mace (1978). Jones and Levy (1987) applied the KLT transformation to enhance stacked seismic sections and increase the SNR value by removing the information from the data that is incoherent from trace to trace. Freire and Ulrych (1988) used the KLT in a different manner to analyze vertical seismic profiling (VSP) data and separate downgoing and upgoing signals. Using the singular value decompositions, they introduced low-pass, band-pass and high-pass filters and showed that the contribution of the horizontally aligned downgoing waves in the time-shifted VSP section can be recovered using the low-pass filter. The uncorrelated noise component, however, can be filtered out by high-pass filter because it contributes to the last few eigenimages only. Interestingly, the separated upgoing waves are recovered after applying band-pass filters. Using SVD approach, Ulrych et al. (1988) and Freire and Ulrych (1990) studied several other problems including attenuation of multiple reflections.

Noise attenuation/suppression for 3D stacked data seismic sections is discussed through f-xy prediction method by Chase (1992) and through f-xy projection method by Ozdemir et al. (1999) and Soubaras (2000). Application of eigenimage decomposition on 3D data in the frequency domain (f-xy) is discussed by Trickett (2003). In his method, the data is transformed to the frequency domain using the Fourier transformation and then each constant-frequency slice is decomposed independently. After reconstructing the constant-frequency slice using the first few eigenimages (depending to the number of events) the data is transformed to the time domain by inverse Fourier transformation. The newly transformed data has greater SNR value compare to the original data structure.

Spatial and temporal analysis of a data structure is also considered as major issues in the data processing. Most of the observable phenomena in the empirical sciences have been collected through several receivers that are located at different

places. The so called multichannel time series is usually constructed by detecting one or more natural and/or artificial sources through out a period of time by several geophones/radars located at different positions. As a result, the gathered data are a function of time and spatial offset. Extracting signal properties such as frequency and wavenumber from a noisy data structure is not a simple task. Several statistical techniques are proposed to address precisely the following questions. For a data structure: how many sources are present in the data? What are the signals' frequencies? Where are they located? What are their spectral levels?

For a temporal analysis of a given time series, the discrete Fourier transform (DFT) usually provide the signals' frequency with acceptable resolutions through the power spectrum analysis. This is because of the fact that a time series is usually made of a large sample of time points, $N \sim \mathcal{O}(10^2 - 10^3)$. Therefore, for a time duration, there is enough information in the data structure to retrieve the signals' frequency in a precise manner.

For spatial analysis, however, the above argument may not be true. A multichannel time series is usually observed with a small number of detectors, $M \sim \mathcal{O}(10^1)$. Therefore, a spatial power spectrum using DFT will yield low resolution and then less accurate results due to the lack of data points. Implementing high resolution methods is the subject of array signal processing.

Array signal processing (or multichannel time series analysis) has been used for several decades in radar, sonar (SOund Navigation And Ranging) and seismic data analysis. A set of detectors that are spatially distributed at specific locations is usually considered as an array. These detectors receive and record incoming signals form sources in their field of view, see Figure 1.1.

Several techniques are proposed to analyze multichannel time series in order to provide higher spatial resolution. Capon (1969) first introduced the minimum variance method (also called maximum likelihood estimator) for a 2D problem (time-space) with high resolution in the spatial domain. The maximum entropy method proposed later by Burg (1975) that provided a high spatial resolution for 1D problems. Several extensions of the maximum entropy method to accommodate 2D problems were developed by Roucos and Childers (1980), Lim and Malik (1981), and McClellan (1982). Linear prediction method and maximum likelihood estimator are also proposed and studied for spectral analysis of 1D and 2D problems (Good, 1963; Schweppe, 1968; Hahn and Tretter, 1973; Frost and Sullivan, 1979; Jain and Raganath, 1978; Jackson and Chien, 1979; Kumaresan and Tufts, 1981; Wax and
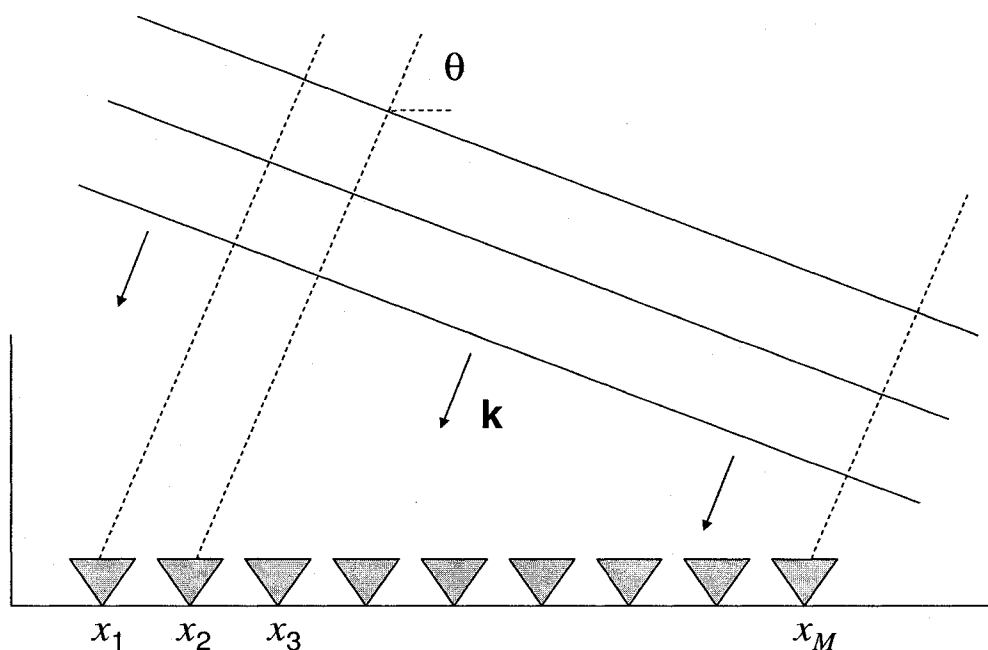
Figure 1.1: Schematic presentation of a linear array that records a down going plane wave with the wave vector **k**. x_m; $m = 1, \ldots, M$, represents the position of each detector from the coordinate's origin.

Kailath, 1983).

In case of narrow-band sources, however, the above methods failed to provide spectral densities with acceptable resolution. Narrow-band sources radiate within a small frequency band about a particular frequency, or class of frequencies. Since the frequency bandwidth is very small, the signal peaks merge together. To overcome such deficiency, in particular, Pisarenko (1972) developed a new method based on the eigenstructure of the covariance matrix of the observed data. The new method provides much better resolution than previous methods such as the minimum variance, maximum entropy, and linear prediction methods. Following Pisarenko's study, several investigators improved and extended his method from a uniform array, as considered by Pisarenko (1972), to a general array (Reddi, 1979; Schmidt, 1979; Bienvenu and Kopp, 1980; Schmidt, 1981; Bienvenu and Kopp, 1981; Johnson and Degraff, 1982; Kumaresan and Tufts, 1983; Schmidt, 1986). For example, Pisarenko (1972) and Schmidt (1979) developed their methods based on the eigenstructure of the covariance matrix in time domain, while Bienvenu and Kopp (1980, 1981) used the eigenstructure of the spectral density matrix, i.e. the covariance matrix in the

frequency domain. See also Pillai (1989) and Wax, Shan, and Kailath (1984) for detail and review about these methods.

Schmidt (1981, 1986) developed the eigenstructure method which is well suited for seismic data. This method that is called multiple signal classification (MUSIC) has shown a superior resolution over the other methods for seismic data (Goldstein and Archuleta, 1987). The term MUSIC addresses experimental and theoretical methods that are used to estimate the parameters of multiple wavefronts observed by an array of antennas, such as: number of signals, directions of signal arrival, polarizations, multiple frequency etc.

1.1 The scope of thesis

This thesis can be divided in two major sections: In the first section we discuss the possible enhancement of the signal-to-noise ratio of a data structure using the eigenimage decomposition method.

In chapter 2 we introduce the singular value decomposition (SVD) of a matrix that is known as one of the powerful tools in the SNR enhancement. The SVD analysis is basically an eigenanalysis technique that extracts a set of eigenvectors and their associated eigenvalues from a designated data structure. Similar to other statistical methods the main purpose of the SVD is to simplify a dataset by reducing dimensionality while retaining the characteristics of the dataset. We first review the mathematical framework of the SVD in a very general manner that is applicable to an arbitrary complex data structure. Following the definition, the eigenimage filtering based on the magnitude of the singular values of the data matrix is presented. At the end, we discuss briefly the relationship between the SVD and the other statistical methods such as principal component analysis (PCA) and Karhunen-Loeve Transformation (KLT).

In chapter 3 we examine the SVD capability in enhancing SNR value with synthetic data. At first we synthesize a seismic section that includes three reflected events from zero dip layers. We show that after moveout correction the SVD analysis is very efficient in recovering the data structure with less noise. However, the SVD recovery is fairly poor on the same data if no moveout correction was carried. Therefore, the results are still noisy. To continue we introduce a synthesized poststack 3D data structure with three events (three layers). In general we assume that each layer can have different dips relative to the x- and y-direction. We show that a direct

application of the SVD would not be able to recover the data structure very well. In this regard following Trickett (2003), we apply the eigenimage decomposition in the frequency domain rather than time domain. For linear events, we discuss that the Fourier transformed data has similar properties to the eigenimage decomposition. The latter method is then called *f-xy* eigenimage decomposition. After reconstructing the frequency domain data with greater SNR value, the reconstructed data is then transformed to the time domain.

In the second part of this thesis we discuss the spatial and temporal analysis for a time series.

As we discussed earlier, due to the small number of detectors, the total number of gathered data points in spatial dimensions is smaller than that of in temporal dimension by one (at least) order of magnitude. In chapter 4, following Schmidt (1981, 1986), we introduce the eigenstructure based method called multiple signal classification (MUSIC). This method has shown a superior resolution over the other methods for seismic data (Goldstein and Archuleta, 1987). The idea behind the MUSIC is to separate the data structure into two orthogonal signal and noise subspaces. Therefore, any arbitrary vector that is orthogonal to the noise subspace would be equal to a linear combination of the signal's eigenvectors. By browsing through a pool of possible eigenvectors, one can determine the signals' wave vector in high resolution. For more general situations, however, some smoothing procedures need to be done prior to the MUSIC power estimation. We apply the MUSIC method to the synthetic data that we introduced in chapter 3.

Spatial and temporal analysis of real space data observed by a high frequency(HF) radar is the subject of Chapter 5. The Super Dual Auroral Radar Network (Super-DARN) is a network of HF radars that monitors ionospheric plasma convection over the majority of the northern and southern polar regions. The pulsations in the Earth's magnetic and electric field are often detected with these radars. In particular, observation of field line resonances by SuperDARN radar are common. Field line resonances are standing wave mode oscillations that transport energy from the outer magnetosphere in to the ionosphere. The observed quantity is the doppler velocity vector of the bulk flow in the ionospheric plasma. We first discuss the temporal analysis of the data using the periodogram calculation (Chatfield, 1991). The spatial-temporal analysis is also carried out on the data using both 2D DFT and the MUSIC methods.

Chapter 6 is devoted for conclusion and further discussions. List of symbols and

some definition are given in appendices A and B, respectively.

Chapter 2

Singular value decomposition

As we discussed earlier, enhancing the signal-to-noise ratio (SNR) is an important issue in data processing. The SNR which is the ratio of the amplitude of the signal to the standard deviation of the noise, represents the quality of the signal in the data structure. As a result, the greater the ratio, the less noise in the observed data.

Practically, the SNR enhancing is not a easy task. Several methods are proposed in order to separate the signals from the random noises, such as Principal Components Analysis (PCA), Singular Value Decomposition (SVD), and Karhunen-Loeve Transformation (KLT).

Singular value decomposition is known as one of the powerful tools in the SNR enhancement. However, it has several other applications in time series analysis such as filtering, detecting and estimating common structures (Ulrych, Sacchi and Freire, 1999).

The SVD method is basically an eigenanalysis technique that extracts a set of eigenvectors and their associated eigenvalues from a designated data structure. Similar to other statistical methods the main purpose of SVD is to simplify a dataset by reducing dimensionality while retaining characteristics of the dataset.

In this chapter we first review the mathematical framework of the SVD in more detail. The procedure that is given here is very general and is valid for an arbitrary complex data structure. Eigenimage filtering of a data structure based on the magnitude of the singular values is presented in section 2.2 The other statistical methods such as PCA and KLT and their relationship to the SVD are briefly discussed in sections 2.3 to 2.5. Section 2.6 is devoted to final remarks.

2.1 Mathematical framework of SVD theory

Basically, the singular value decomposition is an orthogonal transformation or an expansion of a matrix with rank r in terms of matrices with rank-1 (Lanczos, 1961). See appendix A for definition of the matrix rank. The singular value decomposition of a $M \times N$ (without loss of generality we assume that $M < N$) complex data matrix $\mathbf{X}$ composed of M traces with N data points per trace can be written as (Lanczos, 1961)

$$\begin{aligned} \mathbf{X} &= \mathbf{U}\Sigma\mathbf{V}^H, \\ &= \sum_{i=1}^{r} \sigma_i \mathbf{u}_i \mathbf{v}_i^H, \end{aligned} \tag{2.1}$$

where $r \leq M$ is the rank of the matrix $\mathbf{X}$ (number of linearly independent rows or columns of a matrix). Here $()^H \equiv ()^{*T}$ indicates complex conjugate and matrix transpose. $\mathbf{U}$ is a $M \times N$ orthonormal matrix consisting N left singular vectors $\mathbf{u}_i$ as its columns and $\mathbf{V}$ is a $N \times N$ orthonormal matrix consisting N right singular vectors $\mathbf{v}_i$ as its columns. The eigen decomposition of the data structure $\mathbf{X}$, equation (2.1), is schematically shown in Figure 2.1. Multiplying $\mathbf{X}$ by $\mathbf{X}^H$ once from right

$$\begin{aligned} \mathbf{X}\mathbf{X}^H &= (\mathbf{U}\Sigma\mathbf{V}^H)(\mathbf{V}\Sigma\mathbf{U}^H) \\ &= \mathbf{U}\Sigma^2\mathbf{U}^H, \end{aligned} \tag{2.2}$$

and once from left

$$\begin{aligned} \mathbf{X}^H\mathbf{X} &= (\mathbf{V}\Sigma\mathbf{U}^H)(\mathbf{U}\Sigma\mathbf{V}^H) \\ &= \mathbf{V}\Sigma^2\mathbf{V}^H, \end{aligned} \tag{2.3}$$

indicates that $\mathbf{u}_i$ is the ith eigenvector of the matrix $\mathbf{X}\mathbf{X}^H$

$$\mathbf{X}\mathbf{X}^H = \mathbf{U} \begin{pmatrix} \lambda_1 & & & & 0 \\ & \ddots & & & \\ & & \lambda_r & & \\ & & & \ddots & \\ 0 & & & & 0 \end{pmatrix} \mathbf{U}^H, \tag{2.4}$$
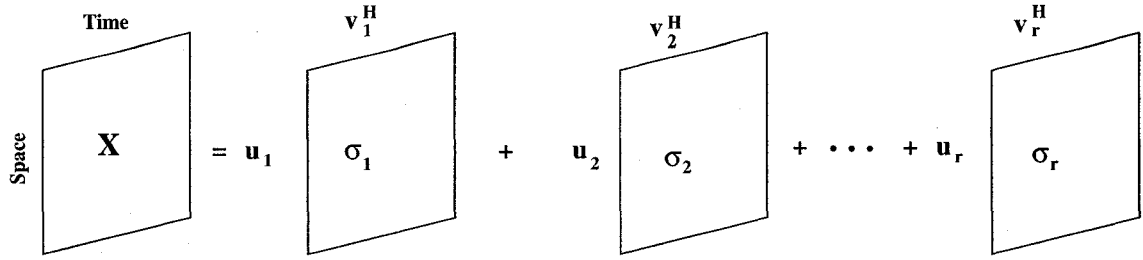
Figure 2.1: Eigenimage decomposition of the data matrix $\mathbf{X}$ into the sum of weighted eigenimages. From Ulrych, Sacchi and Freire (1999).

and $\mathbf{v}_i$ is the ith eigenvector of the matrix $\mathbf{X}^H\mathbf{X}$

$$\mathbf{X}^H\mathbf{X} = \mathbf{V} \begin{pmatrix} \lambda_1 & & & & 0 \\ & \ddots & & & \\ & & \lambda_r & & \\ & & & \ddots & \\ 0 & & & & 0 \end{pmatrix} \mathbf{V}^H. \tag{2.5}$$

Here λ_i are the eigenvalues of matrix $\mathbf{XX}^H$ or $\mathbf{X}^H\mathbf{X}$. Σ is a $N \times N$ diagonal complex matrix of the complex singular values σ_i $(\sigma_i\sigma_i^* = \lambda_i)$

$$\Sigma = \begin{pmatrix} \sigma_1 & & & & 0 \\ & \ddots & & & \\ & & \sigma_r & & \\ & & & \ddots & \\ 0 & & & & 0 \end{pmatrix} \tag{2.6}$$

that are usually ordered decreasingly, i.e. $|\sigma_1| \geq |\sigma_2| \geq \ldots \geq |\sigma_r|$ (Lanczos, 1961). The number of nonzero singular values depends on the rank of the matrix $\mathbf{X}$. Equation (2.1) is usually referred as the singular value decomposition of $\mathbf{X}$ and has wide range of applications in data processing in the last three decades, see Gerbarands (1981) and references therein.

The square of the singular values σ_i represent the variance or autocorrelation of the matrix $\mathbf{X}$. Therefore, in the SVD method, the first eigenvector is extracted such that it accounts for a maximum amount of variance in the data, corresponding to

the first and largest singular value, σ_1. Then a residual data matrix

$$\mathbf{X}_{\text{res}} = \mathbf{X} - \sigma_1\mathbf{u}_1\mathbf{v}_1^H, \tag{2.7}$$

is calculated to extract the second eigenvector. The procedure is repeated until there are no significant singular values left. Therefore, the variance accounted for by each eigenvector is measured by its eigenvalue. As a result, by examining the eigenvalues (or equivalently singular values) and their relative magnitudes one can estimates the number of significant factors or components in the data matrix $\mathbf{X}$.

Based on the above property of the SVD, Andrews and Hunt (1977) introduced the outer dot product $\mathbf{u}_i\mathbf{v}_i^H$ as the ith eigenimage of the matrix $\mathbf{X}$. Due to orthonormality of the eigenvectors $\mathbf{u}_i$ and $\mathbf{v}_i$, the calculated eigenimages form an orthonormal basis that can be used to reconstruct $\mathbf{X}$ according to (2.1). However, as seen from equation (2.1), the contribution of each eigenimage to the construction of $\mathbf{X}$ is weighted by the magnitude of corresponding singular value. Since the singular values are always in descending order, the greatest contributions in the representation of $\mathbf{X}$ are contained in the first few eigenimages. If all M traces that compose the data matrix $\mathbf{X}$ are linearly independent, then $r = M$ which means that all σ_i are nonzero. So all the eigenimages are required in order to reconstruct $\mathbf{X}$ perfectly. On the other hand, if all traces are linearly dependent the matrix $\mathbf{X}$ has rank one and then can be reconstructed by using only the first eigenimage of $\mathbf{X}$, $\sigma_1\mathbf{u}_1\mathbf{v}_1^H$. In practice, however, the data matrix $\mathbf{X}$ may be reconstructed from the first $p < r$ eigenimages depending on the linear dependence which exists among the traces:

$$\widetilde{\mathbf{X}} \simeq \sum_{i=1}^{p} \sigma_i\mathbf{u}_i\mathbf{v}_i^H \; ; \qquad p < r, \tag{2.8}$$

where $\widetilde{\mathbf{X}}$ is the reconstructed data matrix. In this case, the reconstruction error ϵ, the least square error, can be calculated by

$$
\begin{aligned}
\epsilon &= \|\mathbf{X} - \widetilde{\mathbf{X}}\|^2 \\
&= \|\sum_{i=1}^{r} \sigma_i\mathbf{u}_i\mathbf{v}_i^H - \sum_{i=1}^{p} \sigma_i\mathbf{u}_i\mathbf{v}_i^H\|^2 \\
&= \|\sum_{i=p+1}^{r} \sigma_i\mathbf{u}_i\mathbf{v}_i^H\|^2,
\end{aligned}
\tag{2.9}
$$

where $||\mathbf{A}||^2 = \text{tr}(\mathbf{A}\mathbf{A}^H)$ for any matrix $\mathbf{A}$ and tr denotes trace of the matrix. Simplifying equation (2.9), one finds

$$
\begin{aligned}
\epsilon &= \text{tr}\left[\left(\sum_{i=p+1}^{r}\sigma_i\mathbf{u}_i\mathbf{v}_i^H\right)\left(\sum_{j=p+1}^{r}\sigma_j\mathbf{u}_j\mathbf{v}_j^H\right)^H\right] \\
&= \text{tr}\left(\sum_{i=p+1}^{r}\sum_{j=p+1}^{r}\sigma_i\sigma_j^*\mathbf{v}_i^H\mathbf{u}_i\mathbf{u}_j^H\mathbf{v}_j\right) \\
&= \sum_{i=p+1}^{r}\sigma_i^2,
\end{aligned}
\tag{2.10}
$$

where in the last step we use the identity $\text{tr}(\mathbf{AB}) = \text{tr}(\mathbf{BA})$ and the orthonormality conditions that require $\mathbf{v}_i^H\mathbf{v}_j = \delta_{ij} = \mathbf{u}_i\mathbf{u}_j^H$. Equation (2.10) shows that the error in reconstructing data structure $\mathbf{X}$ using the first p eigenvectors is simply adding together the unused $(r - p)$ eigenvalues $(\lambda_i = \sigma_i\sigma_i^*)$ of the covariance matrix $\mathbf{XX}^H$. As a result, the larger the p the smaller the error.

2.2 Filtering a data structure using eigenimages

For large data structures like seismic time series, the computation of the full decomposition would be a time consuming task. This is particularly due to the large temporal dimension N. However, in most cases we are interested to recover a part of data that can be done by using only a few eigenimages. As a result, instead of computing the full decomposition of the data structure, one can reduce the problem to compute few eigen-decompositions.

Using the above idea, Freire and Ulrych (1988) decomposed the data matrix $\mathbf{X}$ in terms of the ranges of their singular values by introducing low-pass $\mathbf{X}_{\text{LP}}$, band-pass $\mathbf{X}_{\text{BP}}$ and high-pass $\mathbf{X}_{\text{HP}}$ eigenimages:

$$
\begin{aligned}
\mathbf{X} &= \mathbf{X}_{\text{LP}} + \mathbf{X}_{\text{BP}} + \mathbf{X}_{\text{HP}},
\end{aligned}
$$

$$
\mathbf{X}_{\text{LP}} = \sum_{i=1}^{p-1}\sigma_i\mathbf{u}_i\mathbf{v}_i^H,
\tag{2.11}
$$

$$
\mathbf{X}_{\text{BP}} = \sum_{i=p}^{q}\sigma_i\mathbf{u}_i\mathbf{v}_i^H,
\tag{2.12}
$$

$$
\mathbf{X}_{\text{HP}} = \sum_{i=q+1}^{r}\sigma_i\mathbf{u}_i\mathbf{v}_i^H,
\tag{2.13}
$$

where $1 < p \leq q < r$. It is interesting to note that the low-pass image is constructed by highly correlated traces (corresponding to the larger singular values) while the high-pass image is constructed by highly uncorrelated traces (corresponding to the smaller singular values). As a result, the band-pass image is constructed by rejecting those extremes, the highly correlated as well as highly uncorrelated traces. p and q are chosen based on the relative magnitudes of the singular values. By plotting the eigenvalues $\lambda_i = \sigma_i^2$ as a function of the index i, one can estimate p and q. Therefore, depending which part of the data is of more more interest, a filtered decomposition may be performed. As an application, Freire and Ulrych (1988) used the filtered decomposition to separate the down going and up going waves in a vertical seismic profile.

2.3 Principal Components Analysis

Principal components analysis (PCA) is a statistical technique that is used to simplify a dataset by reducing dimensionality of the data matrix (Anderson, 1958; Gnanadesikan, 1977). A multivariate data structure often has a very large number of variables that makes its analysis very difficult. In PCA the number of variables is reduced by taking linear combinations of the variables and discarding the combinations with small variances. In other words, the object of the PCA is to find n uncorrelated parameters $W_1, W_2, \cdots, W_n$ from a combination of n observable $X_1, X_2, \cdots, X_n$ data (Anderson, 1958). If the original dataset is non-correlated, then $W_i = X_i$, otherwise

$$W_i = \sum_{j=1}^{n} U_{ij} X_j, \tag{2.14}$$

or in matrix form

$$\mathbf{W} = \mathbf{U}^H \mathbf{X}, \tag{2.15}$$

where U_{ij} are the eigenvectors of the covariance matrix $\mathbf{R} = \mathbf{X}\mathbf{X}^H$ with property $\mathbf{U}\mathbf{U}^H = \mathbf{I}$ where $\mathbf{I}$ is the identity matrix. The so called principal components W_i are also ordered so that W_1 is the largest amount of variation, W_2 is the second largest amount of the variation and so on, i.e. $\text{Var}(W_1) \geq \text{Var}(W_2) \geq \cdots \geq \text{Var}(W_n)$, where $\text{Var}(W_i)$ denotes the variance of W_i. See equation (B.2) for definition of the variance. For an arbitrary dateset, the best result of principal component analysis can be obtained when the variance of most components W_i are so small to be negligible

(Anderson, 1958).

A simple way to calculate the principal components is to use the covariance matrix of $\mathbf{X}$, i.e. $\mathbf{R} = \mathbf{X}\mathbf{X}^H$. The largest eigenvalue is related to dimensions that have the strongest correlation/energy in the dataset. Note that $\text{Var}(W_i) = \lambda_i$ are the eigenvalues of the covariance matrix $\mathbf{R}$ and we have $\lambda_1 \geq \lambda_2 \geq \cdots \geq \lambda_n$. Therefore, the largest eigenvalue represents the direction or dimension in which the data has the largest variation.

2.4 The Karhunen-Loeve Transform

Similar to SVD and PCA methods, Karhunen-Loeve Transform (KLT) is looking for an optimal way to single out the signals from a data structure (Hemon and Mace, 1978).

Consider a $M \times N$ complex $\mathbf{X}$ matrix and a $M \times M$ orthogonal transformation $\mathbf{K}$ (i.e $\mathbf{K}^H\mathbf{K} = \mathbf{K}\mathbf{K}^H = \mathbf{I}$). The matrix $\mathbf{X}$ can be transformed to a new matrix (representation) $\mathbf{Y}$ ($m \times N$) by applying $\mathbf{K}^H$ as

$$\mathbf{Y} = \mathbf{K}^H\mathbf{X}. \tag{2.16}$$

Calculating the covariance matrix $\mathbf{X}\mathbf{X}^H$ as

$$\mathbf{X}\mathbf{X}^H = \mathbf{K}\mathbf{Y}\mathbf{Y}^H\mathbf{K}^H, \tag{2.17}$$

where $\mathbf{X}$ is replaced from equation (2.16), $\mathbf{X} = \mathbf{K}\mathbf{Y}$. It is very difficult to find the transformation matrix $\mathbf{K}$ in general. One way is to approximate $\mathbf{K}$ such that the mean-square error between $\mathbf{X}$ and the reconstructed one $\mathbf{Y} = \mathbf{K}\mathbf{X}$ is minimized, i.e. $\min(||\mathbf{X} - \mathbf{K}\mathbf{Y}||^2)$. Interestingly, the minimization condition will be satisfied by choosing the transformation matrix $\mathbf{K}$ such that the matrix $\mathbf{Y}\mathbf{Y}^H$ contains the eigenvalues matrix of $\mathbf{X}\mathbf{X}^H$, i.e.

$$\mathbf{Y}\mathbf{Y}^H = \begin{pmatrix} \lambda_1 & & 0 \\ & \ddots & \\ 0 & & \lambda_M \end{pmatrix}. \tag{2.18}$$

See Ahmed and Rao (1975) for details. In this case the transformation matrix $\mathbf{K}$ is called the Karhunen-Loeve transform. Obviously, the transformation matrix $\mathbf{K}$ is

the eigenvector matrix of the covariance matrix $\mathbf{XX}^H$.

2.5   Relationships between PCA, SVD and KLT

In the last three sections we discussed SVD, PCA and KLT techniques that are used for different seismic data problems. It is interesting to see what relation holds among them. This has been subject of a long term debate among the experts. Anderson (1975) stated that the SVD and the PCA are very similar but the SVD and the KLT are not identical. Ahmed and Rao (1975) discussed that in the context of data compression the KLT and the PCA are similar. Taylor (1977) studied the SVD and the PCA and concluded these are identical techniques.

To elaborate the relationships, we start from the SVD decomposition of a data matrix $\mathbf{X}$, equation (2.1),

$$\mathbf{X} = \mathbf{U\Sigma V}^H. \tag{2.19}$$

Calculating the covariance matrix $\mathbf{XX}^H$ and using the orthonormality of $\mathbf{V}$, one finds

$$\begin{aligned} \mathbf{XX}^H &= \mathbf{U\Sigma V}^H\mathbf{V\Sigma U}^H \\ &= \mathbf{U\Sigma}^2\mathbf{U}^H, \end{aligned} \tag{2.20}$$

where $\mathbf{\Sigma}^2$ is $\mathbf{XX}^H$'s eigenvalues matrix. Comparing equations (2.17) and (2.20), we find that $\mathbf{K} = \mathbf{U}$ or in other words the matrix $\mathbf{U}$ obtained by the SVD technique is the Karhunen-Loeve transform matrix with $\mathbf{Y} = \mathbf{\Sigma V}^H$. As a result, the SVD decomposition of the matrix $\mathbf{X}$, equation (2.19), can be considered as the Karhunen-Loeve transform of the matrix $\mathbf{X}$

$$\begin{aligned} \mathbf{X} &= \mathbf{U}\,(\mathbf{\Sigma V}^H) \\ &= \mathbf{KY}. \end{aligned} \tag{2.21}$$

It is interesting to note that in the KLT technique, the matrix $\mathbf{Y}$ is the representation of the original data matrix $\mathbf{X}$ in the coordinate system made of principal axes. It means that elements of the matrix $\mathbf{Y}$ are the principal components of the data structure $\mathbf{X}$. This shows that the KLT and PCA are similar. Therefore, we conclude that all three methods, PCA, SVD and KLT are similar.

2.6 Summary

In this chapter we reviewed the mathematical framework of the SVD. Any complex valued data structure can be decomposed to its eigenimages weighted by singular values. Interestingly, the first few eigenimages are often enough to reconstruct the data structure with less noise. This is because the highly uncorrelated structures such as random noise are presented mostly in the eigenimages with smaller singular values. Several preparations such as stacking may be needed before applying the SVD. In the next chapter, we provide some synthetic data structures in order to see how the SVD method can handle the various situations.

Chapter 3

Singular value decomposition: application to seismic data

In this chapter we present different synthetic data to see how the SVD works. Specifically we are interested in 3D data structure that is recorded in layers with nonzero dips. In section 3.2 we will discuss the SNR enhancement on data with zero dip events. We first consider a three-event data with moveout correction. Then we apply the SVD on the same data structure but with no moveout correction to demonstrate the SVD ability to increase SNR. In Section 3.4 we introduce a poststack 3D data structure with three events (three layers). More generally we consider that each layer can have different dips relative to the x- and y-direction. We will show that a direct application of the SVD was not able to recover the data structure. In this regard *f-xy* eigenimage decomposition is introduced in section 3.5. Further discussions and concluding remarks are presented in section 3.6.

3.1   Seismic surveys

Any seismic survey consists of three main stages, (a) data acquisition, (b) data processing and (c) interpretation. In the data acquisition phase, several seismic waves are generated synthetically and then detected after passing through the region of study. The most common form of seismic data acquisition is the reflection seismic survey. A reflection seismic survey typically involves generating hundreds to thousands of seismic shots (as sources) at different locations. After passing through the region of study, the generated energy by each shot is detected by geophones

and/or hydrophones (known as receivers) located at different distances from the source positions. Each receiver generates a trace, a sequence of observations at different time that is recorded for further analysis. A main goal in seismic data processing is to improve the low signal-to-noise ratio (SNR) of the observed seismic data. To achieve this goal, in data acquisition phase, one would use as many receivers per shot as possible and then collect the data. These data are usually processed using the common mid-point (CMP) method. In CMP processing, seismic traces are grouped into CMP gathers on the basis of shared source-receiver midpoint bins. Velocity functions are calculated for selected CMP gathers based on arrival time variations as a function of source-receiver offset for a few reflection events in the gather. CMP velocity functions are then interpolated throughout a survey area to construct a velocity model of the layer. This velocity model is used to perform normal move-out (NMO) corrections throughout the survey. NMO is a non-linear stretching of the seismic time axis to remove the travel time component due to source-receiver offset. NMO is applied to each trace in a gather so that the reflection travel times on all traces approximate that of a trace with zero source-receiver offset (a coincident source and receiver). After NMO, all the traces in a CMP gather can be summed, or stacked. As a result, reflection events on the different traces will sum constructively, producing a single trace with a SNR that is much higher than that of the individual prestack traces. By repeating this procedure for all CMP gathers in the survey, the prestack data set is replaced by a much smaller poststack data set but with higher signal quality.

3.2 Synthetic data: events with zero dips

3.2.1 Flat Events

In this section, we apply the SVD method to a simple case, a $M \times N$ data structure $\mathbf{X}$ consisting $M = 20$ traces that are composed of three horizontal (parallel to the x-axis) events. Each trace contains $N = 450$ time samples. This data can be considered as the observation of three horizontal seismic reflections by 20 geophones placed along the x-axis after moveout corrections. See Figure 3.1a. The data are also contaminated with uncorrelated noise of standard deviation of 10% of the maximum amplitude $\sigma = \max(\mathbf{X})/10$, which corresponds to signal-to-noise ratio, SNR= 10 db.

The SNR is defined as

$$SNR = \max(\mathbf{X})/\sigma. \tag{3.1}$$

Figure 3.1b shows the reconstructed data $\widetilde{\mathbf{X}}$ using only one eigenimage, i.e.

$$\widetilde{\mathbf{X}} = \sigma_1 \mathbf{u}_1 \mathbf{v}_1^T, \tag{3.2}$$

where $()^T$ indicates matrix transpose. It is clear that the original event is completely recovered. Furthermore, the reconstructed data is less noisy compared with the original one, see Figure 3.1(a).

Subtracting the raw data from the reconstructed one, i.e. its first eigenimage, gives

$$\mathbf{X} - \widetilde{\mathbf{X}} = \sum_{i=p}^{M} \sigma_i \mathbf{u}_i \mathbf{v}_i^T, \tag{3.3}$$

where $p = 2$ and $M = 20$. As seen in Figure 3.1(c), the result more or less is just the noise. The above observation can be explained by finding the singular values of the data matrix. Statistically speaking, each singular value represents the variance of the data stored in the corresponding eigenimage. In Figure 3.2, we plot the singular values for the above data structure. As shown, the first singular value is much larger than the others. This means that the first eigenimage contains a data with the largest variance.

These results can be also explained by noting that the singular values σ_i are the square root of the eigenvalues $\lambda_i = \sigma_i^2$ of the covariance matrix $\mathbf{X}\mathbf{X}^T$. Physically speaking, eigenvector analysis decomposes the system into normal modes (or eigenstates) with equal or different eigenvalues in which each eigenvalue represents the fraction of energy of the system in the corresponding mode. Therefore, the total energy of the system can be calculated as

$$\mathcal{E} = \sum_{i=1}^{r} \sigma_i^2. \tag{3.4}$$

For the above data structure, it is easy to see that approximately 64% of the total energy is stored in the first eigenstate, i.e.

$$\frac{\mathcal{E}_1}{\mathcal{E}} = \frac{\sigma_1^2}{\sum_{i=1}^{M} \sigma_i^2} \approx 64\%. \tag{3.5}$$

As a result, one would expect to see most of the signal in the first eigenimage.
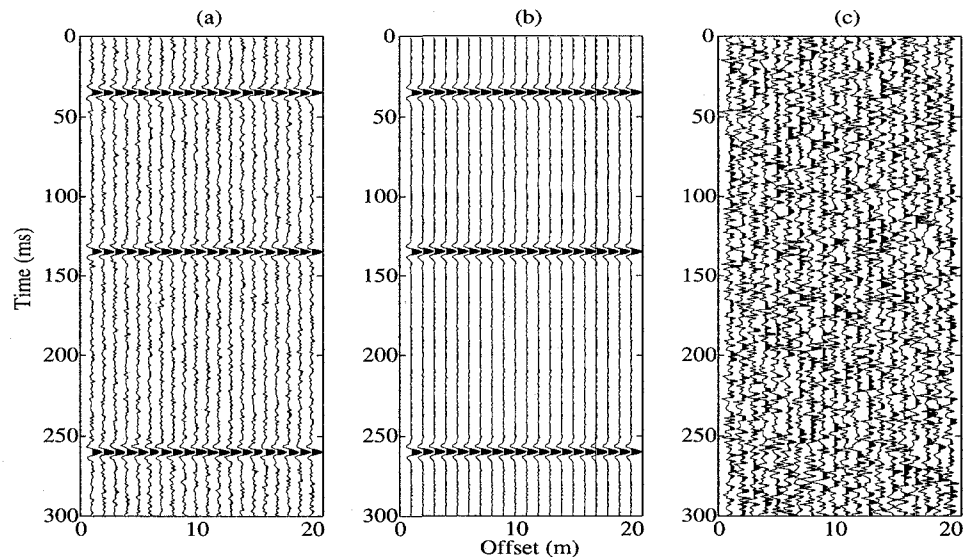
Figure 3.1: (a) A data matrix $\mathbf{X}$ composed of three events and contaminated with an uncorrelated noise with standard deviation of 10% of maximum amplitude. Note that only first 300 time samples are shown.(b) Reconstructed matrix $\widetilde{\mathbf{X}}$ in t-x domain using the first eigenimage only, equation (3.2). Comparing with (a), the reconstructed data clearly has less noise. (c) Original data subtracted by reconstructed data, $\mathbf{X} - \widetilde{\mathbf{X}}$. See equation (3.3). Note that amplitudes in (c) were scaled.
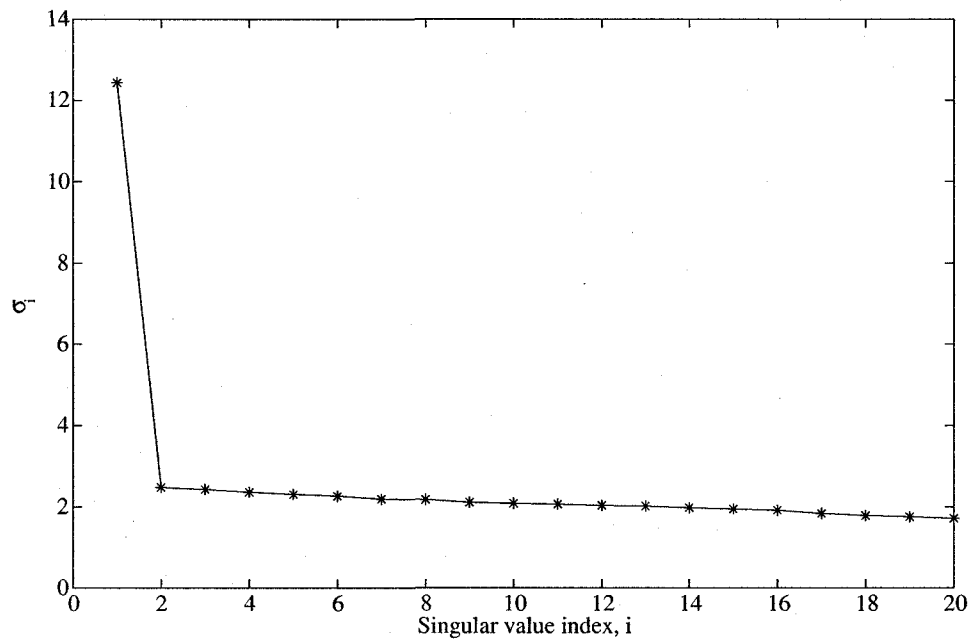
Figure 3.2: Singular values, σ_i, for the moveout corrected event data structure. Figure 3.1(a). The first singular value is approximately 5 times larger than the second one.
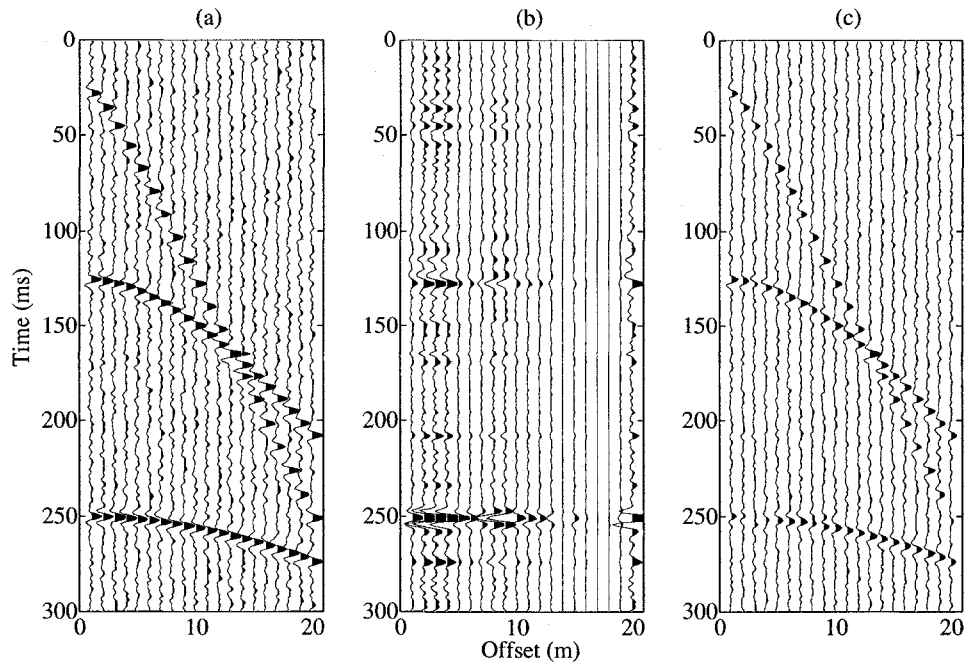
Figure 3.3: (a) Same as Figure 3.1(a) with no moveout correction. (b) Reconstruction of the data matrix in t-x domain using the first eigenimage. (c) The residual, original data, Figure 3.3(a), subtracted by reconstructed data given by Figure 3.3(b). See equation (3.6).

3.2.2 Hyperbolic Events

The data structure that we studied in section (3.2.1) can be considered as the moveout correction of a more realistic data. In this section, we would like to consider a data structure with no moveout correction in the t-x domain to examine the efficiency of the SVD method.

Similar to the last section, we consider a real $M \times N$ data structure $\mathbf{X}$ consisting $M = 20$ traces that are composed of three hyperbolic events which are corresponding to a direct observation of three reflectors by 20 geophones placed along the x-axis in a seismic section. Each trace contains $N = 450$ time samples. The data are also contaminated with uncorrelated noise of standard deviation of 10% of the maximum amplitude $\sigma = \max(\mathbf{X})/10$, i.e. SNR= 10. Figure 3.3(a) represents a data structure, $\mathbf{X}$, with three parabolic events.
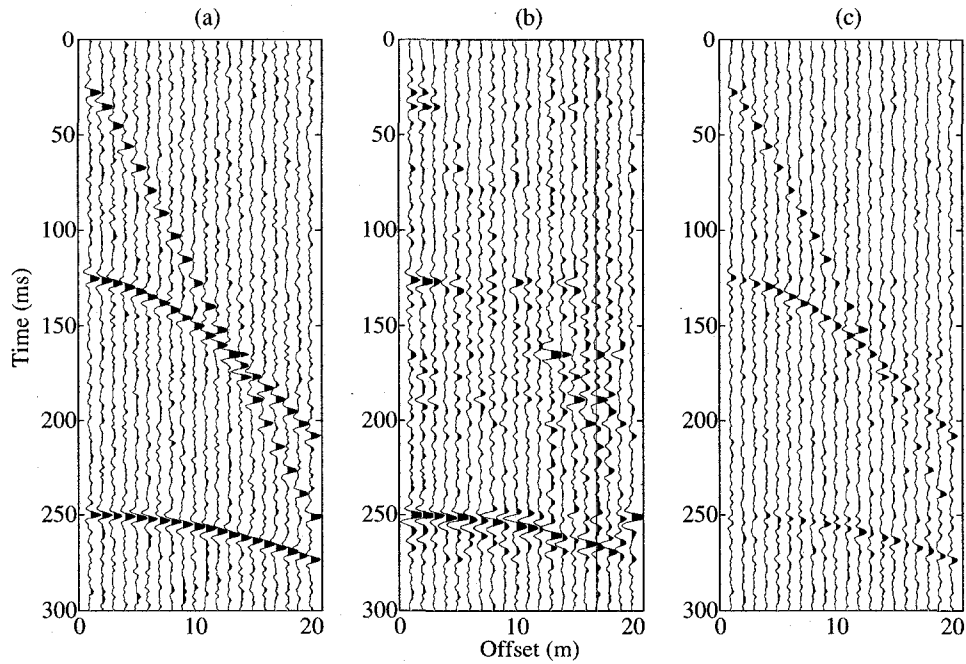
Figure 3.4: (a) Same as Figure 3.3(a). (b) Reconstruction of the data matrix in t-x domain using the first 5 eigenimages. (c) The residual, original data, Figure 3.4(a), subtracted by reconstructed data given by Figure 3.4(b). See equation (3.6).

Figure 3.5: (a) Same as Figure 3.3(a). (b) Reconstruction of the data matrix in t-x domain using the first 10 eigenimages. (c) The residual, original data, Figure 3.5(a), subtracted by reconstructed data given by Figure 3.5(b). See equation (3.6).

Applying the SVD method, we reconstruct the above data using the first eigen-image only, the first 5 eigenimages, and the first 10 eigenimages. Figures 3.3(b), 3.4(b) and 3.5(b) demonstrate the reconstruction of the data using 1 eigenimage, 5 eigenimages and 10 eigenimages, respectively. It is clear, even after using 10 eigen-images, the events are not fully recovered. As a result, one would expect to see a fraction of the events on the residual data, i.e.

$$\mathbf{X} - \sum_{i=p}^{q} \sigma_i \mathbf{u}_i \mathbf{v}_i^T = \sum_{i=q+1}^{M} \sigma_i \mathbf{u}_i \mathbf{v}_i^T, \tag{3.6}$$

as shown in Figures 3.3(c)-3.5(c). Here $p = 1$, $q = 10$ and $M = 20$. These results, however, would be expected since the change in singular value magnitude is more gradual in this case compared to the flat event data, see Figure 3.6. Interestingly, the fraction of energy stored in the first eigenimage is approximately 12% of the total energy:

$$\frac{\mathcal{E}_1}{\mathcal{E}} = \frac{\sigma_1^2}{\sum_{i=1}^{M} \sigma_i^2} \approx 12\%, \tag{3.7}$$

that is ~ 5 times smaller than what we found in equation (3.5) for the correlated data.

It is necessary to note that the whole event can be fully recovered by adding more eigenimages to the reconstructed data. But this makes the eigenimage analysis more or less useless because by adding more eigenimages, the reconstructed data becomes more noisy. This can be seen by comparing Figures 3.3(c)-3.5(c). The more eigenimages that we use, the more noises appear in the reconstructed data. In order to avoid the above problem one must perform the moveout correction on the original data initially to increase correlation among traces. In the following section we will apply the eigenimage decomposition on a real seismic data gathered in the district of western Canadian sedimentary basin.

3.3 Real data: removing ground roll

One of the common problem in the analysis of a real shot gather is the presentation of the surface waves in the data. Every shot produces three type of seismic waves: air waves, body waves, and surface waves. Body waves are compressional waves that
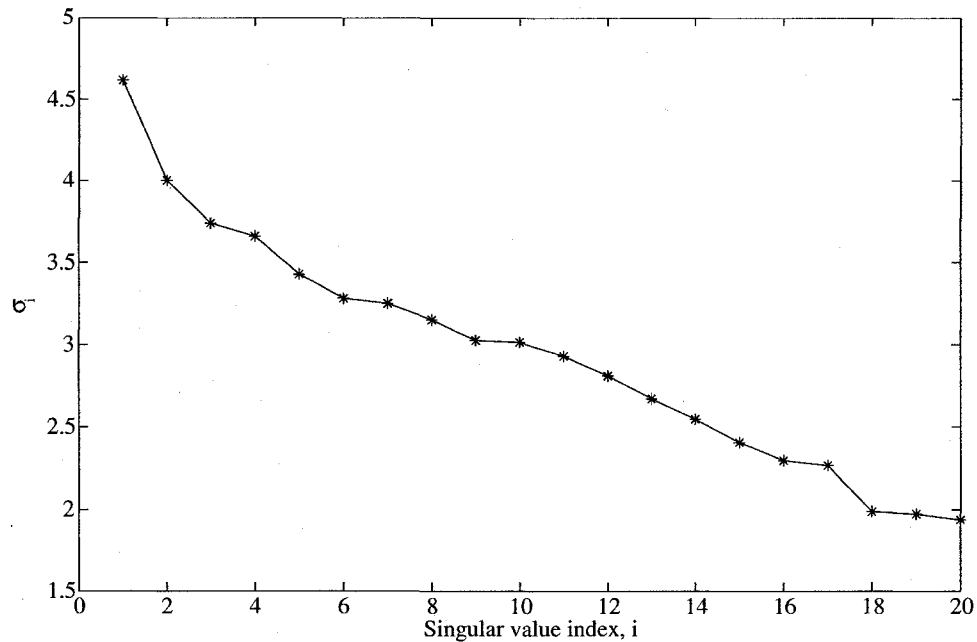
Figure 3.6: Singular values, σ_i for the hyperbolic event data structure, Figure 3.3(a). In contrast with Figure 3.2, the singular values are changing gradually in this case.

travel within a layer and reflect from interfaces. Reflections are usually recognized by their hyperbolic travel times. In seismology, surface wave refers to perturbations that propagate close to the surface of the Earth. The amplitude of surface waves decreases rapidly in deeper layers. Based on the particle motion, the surface wave is usually classified into Love wave and Rayleigh wave. Love waves have transverse motion that produce horizontal shifting in the Earth's surface. In contrast, the Rayleigh wave have both transverse and longitudinal motions. In the Rayleigh waves, the particle moves in a vertical circle or ellipse moving in the direction of propagation. These waves are generated by the interaction of P- and S- waves at the Earth's surface.

Ground roll (source generated noise of surface wave) is type of Rayleigh waves that propagate along the free surface and characterized by their low frequencies, low velocities and strong amplitudes. These waves which are typically recorded as wiggles by each geophone are due to the ground motion caused by the shot (Yilmaz, 1999).

Several methods are proposed for removing or attenuating the ground roll, such as stacking, muting, band-pass frequency filtering, and eigenimage decomposition
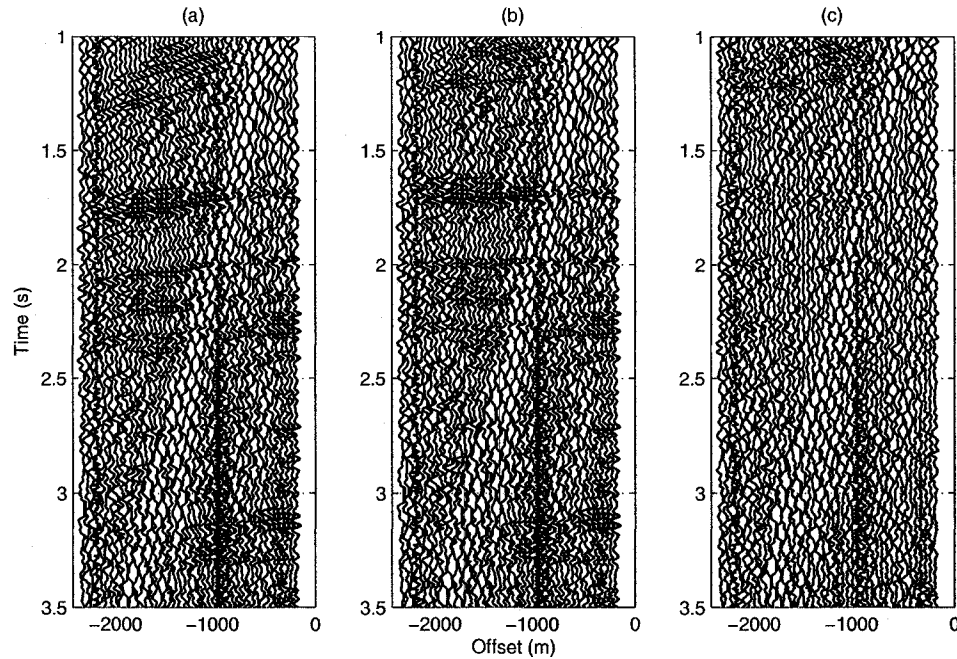
Figure 3.7: (a) A typical seismic shot gather. Hyperbolic events represent reflections from underlying layers and linear events produced by surface waves (ground roll). (b) Moveout corrected data. (c) Moveout corrected data after removing the reflected events using SVD.

(Ulrych, Sacchi and Freire, 1999; Yilmaz, 1999). Here we would like to attenuate the surface waves using the eigenimage decomposition. The data that we are going to use is recorded in the district of the western Canadian sedimentary basin.

The Western Canadian Sedimentary Basin (WCSB) is a vast sedimentary basin with an area about 1.4 million km^2. It is mainly located in southwestern Manitoba, southern Saskatchewan, Alberta, northeastern British Columbia and the southwest corner of the Northwest Territories. The basin consists of a 6 km thick massive wedge of sedimentary rock under the Rocky Mountains in the west that thins to zero as it extends to the Canadian Shield in the east. This sedimentary basin is one of the largest reserves of petroleum, natural gas and coal in the world (Mossop and Shetsen, 1994).

Figure 3.7(a) represents a typical seismic shot gather that is taken from a region of the Western Canadian Sedimentary Basin. The data is recorded by 45 geophones, each separated by 50 m. Each trace contains 1000 time points with a time interval of .004 sec. Reflections from different layers are shown as hyperbolic events. These
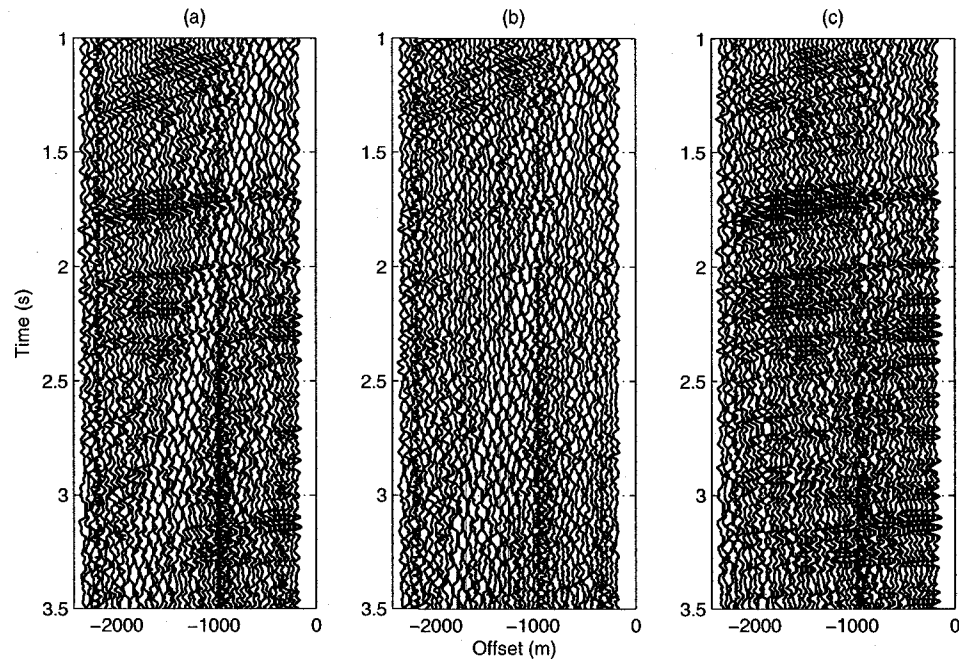
Figure 3.8:   (a) The original shot gather. (b) The separated surface waves using SVD decomposition. (c) The pure (hyperbolic) reflected events.

events are also contaminated by some (sloped) linear events produced by surface waves.

In order to single out the reflected signals from those surface waves, we use the eigenimage decomposition. Since the reflected events are hyperbolic we need to perform a moveout correction prior to the eigenimage decomposition, see section 3.2.2. Figure 3.7(b) shows WCSB data after the moveout correction. It is clear that the reflected events are now more or less flattened. We separate the surface waves from the reflected events by employing the eigenimage decomposition and subtracting the first 10 eigenimages from the moveout corrected data. The result is shown in Figure 3.7(c) that has no significant reflected events. Therefore, Figure 3.7(c) more or less contains surface waves and noise. Inverting moveout procedure on the Figure 3.7(c) and subtracting it from the original data, Figure 3.7(a), one can get the reflected events with no ground roll. This procedure is shown in Figure 3.8. Figure 3.8(a) again represents the original shot gather while Figure 3.8(b) demonstrates the the ground roll and noise portion of the data (after implementing the eigenimage decomposition and inverse moveout procedure). Figure 3.8(c) shows the (hyperbolic) reflected events with no sign of ground roll.

So far we have shown that SVD method works very efficiently on enhancing signal to noise ratio of data structures composed of flat events in t-x domain. However, as we will discuss in the next section, there are some shortcomings with eigenimage analysis in t-x domain, specifically, when the data structure is composed of dip events.

3.4 Synthetic data: linear dipping events

In previous sections, we discussed the application of the SVD method for a data structure in t-x domain. We specifically demonstrated the efficiency of enhancing signal to noise ratio of SVD method for both (hyperbolic event) and (flat event) data. We concluded that in t-x domain, the SVD analysis on the flat data is more efficient and reliable.

The above analysis, however, was restricted to events with zero dips. In reality, however, the layers' interface has significant dips relative to the horizontal direction. In this section we would like to consider a poststack data composed of several events with nonzero dips. See Figure 3.9(a).

Although, the eigenimage analysis is able to recover and enhance the signal-to-noise ratio of the flat events data (zero dips) with a few eigenimages in the t-x domain, it fails when the events have dips. This can be seen in Figures 3.9(b)-3.11(b), as we applied SVD on the data in Figure 3.9(a). Figures 3.9(b)-3.11(b) show the reconstruction of the data using 1 eigenimage, 5 eigenimages and 10 eigenimages, respectively. Similar to the hyperbolic events, the events are not fully recovered even after using 10 eigenimages. Therefore, the residual will carry a fraction of the events as shown in Figures 3.9(c)-3.11(c). The change in singular value magnitudes is also gradual, see Figure 3.12.

In the next section we will show that in the case of nonzero dips data, the SVD analysis could be more efficient in f-x (frequency) domain rather than t-x domain. This was first introduce by Trickett (2003) who performed the SVD analysis on a stacked 3D seismic volume in the f-xy domain. He showed that in this domain, the SVD analysis performs equally well on flat or dipping events.

Transforming data to the f-x domain also reduces the rank of the data matrix. As we mentioned, the eigenimage analysis is very sensitive to the rank of the data matrix. The higher the rank, the more uncorrelated traces in data. As a result, one
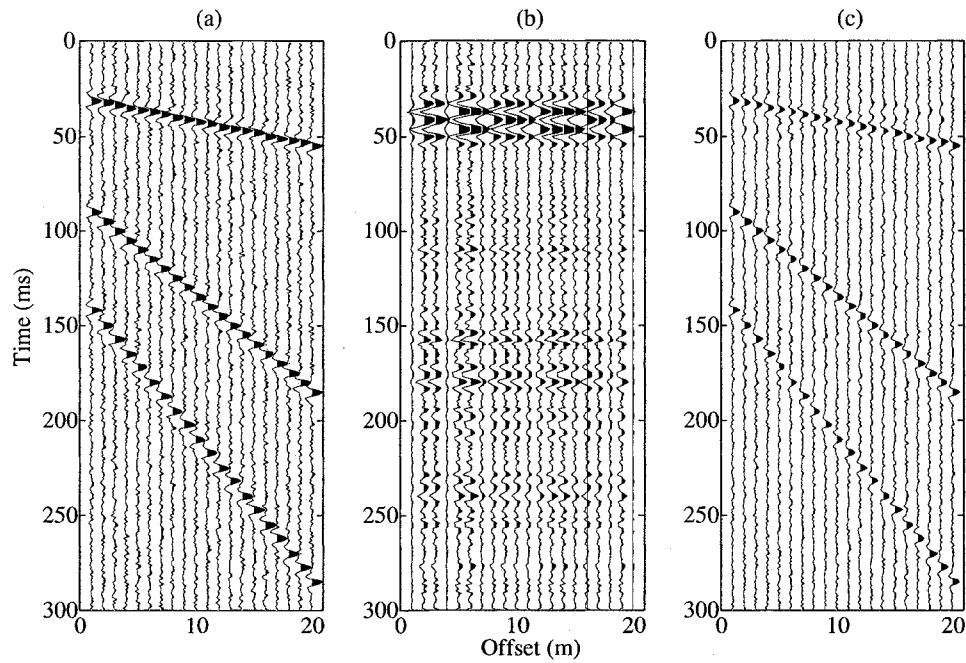
Figure 3.9: (a) Data matrix composed from three events with nonzero dips. The data is also contaminated with an uncorrelated noise with standard deviation of 10% of maximum amplitude. (b) Reconstruction of the data matrix in t-x domain using the first eigenimage. (c) The residual, original data, Figure 3.9(a), subtracted by reconstructed data given by Figure 3.9(b).
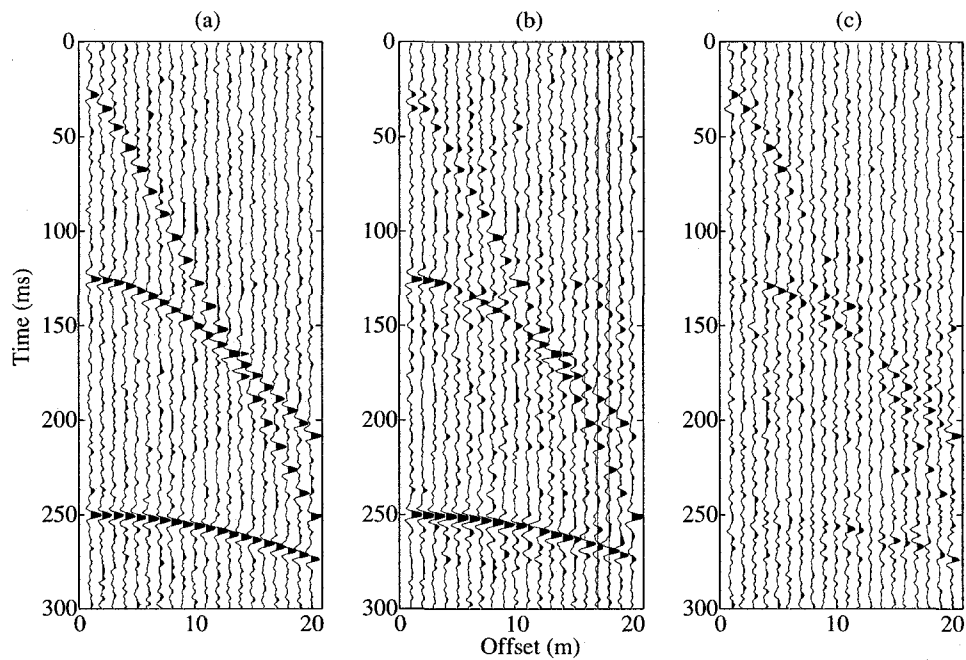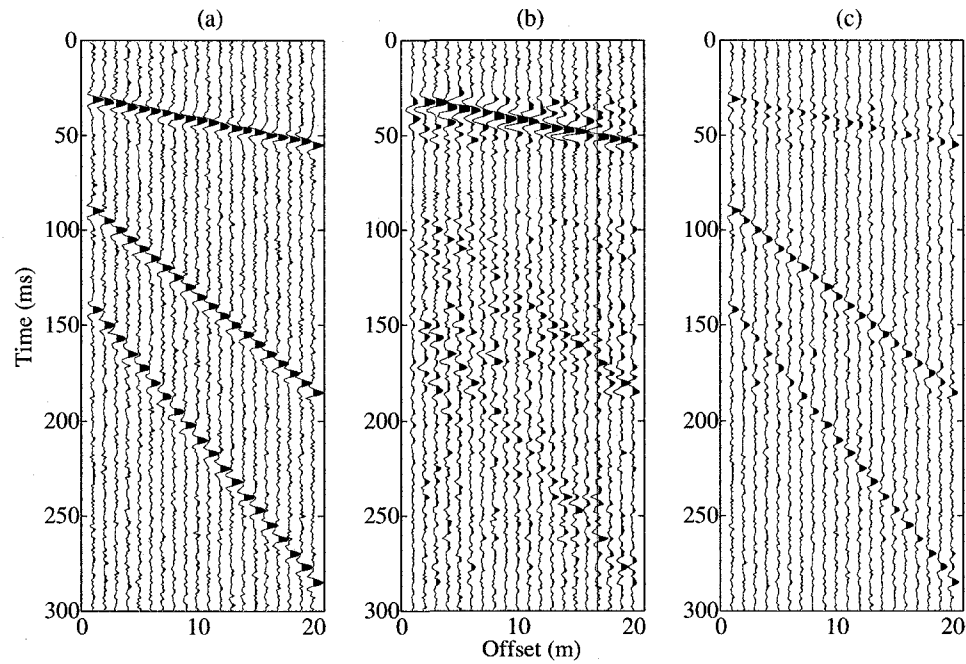
Figure 3.10: (a) Same as Figure 3.9(a). (b) Reconstruction of the data matrix in t-x domain using the first 5 eigenimages. (c) The residual, original data, Figure 3.10(a), subtracted by reconstructed data given by Figure 3.10(b).
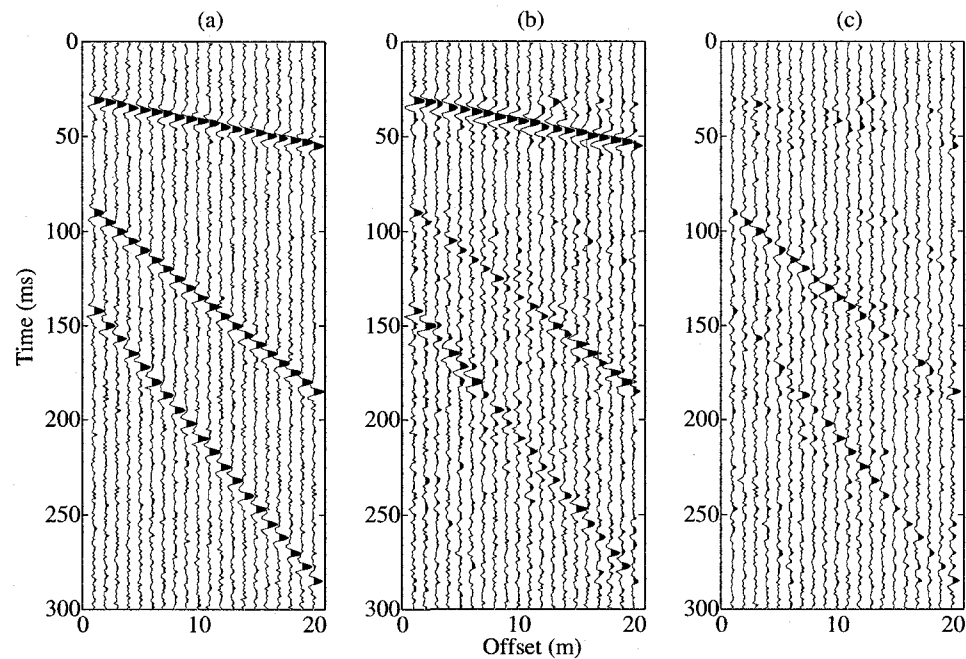
Figure 3.11: (a) Same as Figure 3.9(a). (b) Reconstruction of the data matrix in t-x domain using the first 10 eigenimages. (c) The residual, original data, Figure 3.11(a), subtracted by reconstructed data given by Figure 3.11(b).
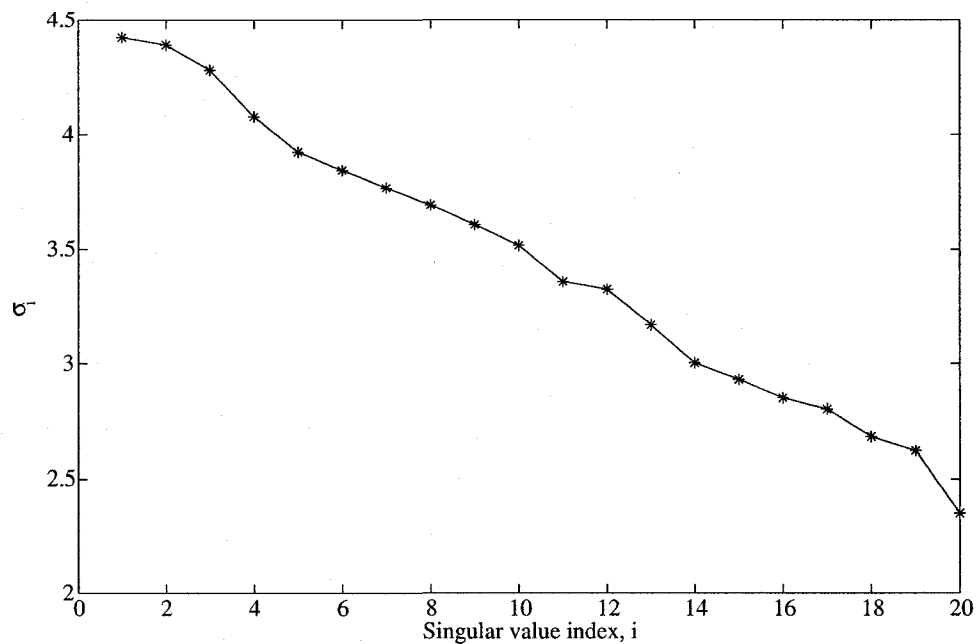
Figure 3.12: Singular values, σ_i for the three events data structure with nonzero dips, Figure 3.9(a). Similar to Figure 3.6, the singular values are changing gradually.

would expect the eigenimage analysis performs more effectively in reconstructing the data in the *f-x* domain.

In the frequency domain one can perform a *f-xy* analysis to enhance signal to noise ratio such as *f-xy* prediction (Chase, 1992) and *f-xy* projection (Ozdemir et al., 1999) which are 3D methods.

3.5   *F-xy* eigenimage analysis

In this section following Trickett (2003), we first show how the eigenimage analysis can be performed in a 3D manner in the *f-xy* domain. Basically, in the *f-xy* domain, each slice with constant frequency is processed independently.

Consider a 3-dimensional seismic section consisting of L events such that each event has a constant dip across the section. Let **X** be a $M_x \times M_y \times N$ 3D data matrix that is composed from $M_x \times M_y$ traces. Any trace **d** is a $N \times 1$ ($t = 0, 1, 2, \cdots, N-1$) column vector that can be represented as

$$\mathbf{d} = [d(0), d(1), \cdots, d(N-1)]^T. \tag{3.8}$$

Therefore, the $(k, \ell)^{\text{th}}$ component of structure $\mathbf{X}$ is a $N \times 1$ column vector $\mathbf{d}_{k\ell}$,

$$\mathbf{d}_{k\ell} = [d_{k\ell}(0), d_{k\ell}(1), \cdots, d_{k\ell}(N_t - 1)]^T, \tag{3.9}$$

where $k = 1, 2, \cdots, M_x$ and $\ell = 1, 2, \cdots, M_y$. We define $\mathbf{d}_{k\ell}$ as the $(k, \ell)^{\text{th}}$ trace of $\mathbf{X}$. Note that in general $M_x \neq M_y$, however, in numerical analysis we assume that $M_x = M_y = M$ for simplicity. Figure 3.13 shows an example of a volume section composed of three planes representing the three events. Each plane has nonzero directional cosines (dips) with the x- and y- axes. Therefore, each plane can be specified mathematically by

$$t = t_{0m} + \alpha_m x + \beta_m y, \qquad m = 1, 2, 3. \tag{3.10}$$

Here t_{0m} represents the cross section of the mth plane with the t-axis, α_m and β_m are corresponding directional cosines in x and y directions, respectively. The travel time of a seismic signal can be also found by equation (3.10). In this case (x, y) represent the location of the corresponding geophone.

For a 3D seismic volume made of L planes, each trace is composed by L events (or signals), say, s_m, $m = 1, 2 \cdots, L$. The magnitude of the signal for the mth event can be represented as

$$s_m(t) = a_m w(t - \tau_m), \tag{3.11}$$

where a_m is the amplitude of the mth signal reflected from m^{th} layer and $t = 0, 1, 2, \cdots, N - 1$. Here $w(t)$ is the wavelet and $\tau_m = t_{0m} + \alpha_m x + \beta_m y$.

It is obvious that each signal s_m would have a contribution to every single trace $\mathbf{d}_{k\ell}$ of the 3D structure $\mathbf{X}$. Therefore, the $(k, \ell)^{\text{th}}$ trace can be found by adding all individual signals

$$d_{k\ell}(t) = \sum_{m=1}^{L} s_{mk\ell}(t), \quad t = 0, 1, 2, \cdots, N - 1, \tag{3.12}$$

where $d_{k\ell}(t)$ is the component of the trace $\mathbf{d}_{k\ell} = [d_{k\ell}(0), d_{k\ell}(1), \cdots, d_{k\ell}(N - 1)]^T$ and

$$s_{mk\ell}(t) = a_m w(t - \tau_{mk\ell}), \tag{3.13}$$

$$\tau_{mk\ell} = t_{0m} + \alpha_m x_k + \beta_m y_\ell. \tag{3.14}$$

Here a_m is the amplitude of mth signal and (x_k, y_ℓ) is the position of $(k, \ell)^{\text{th}}$ geophone.
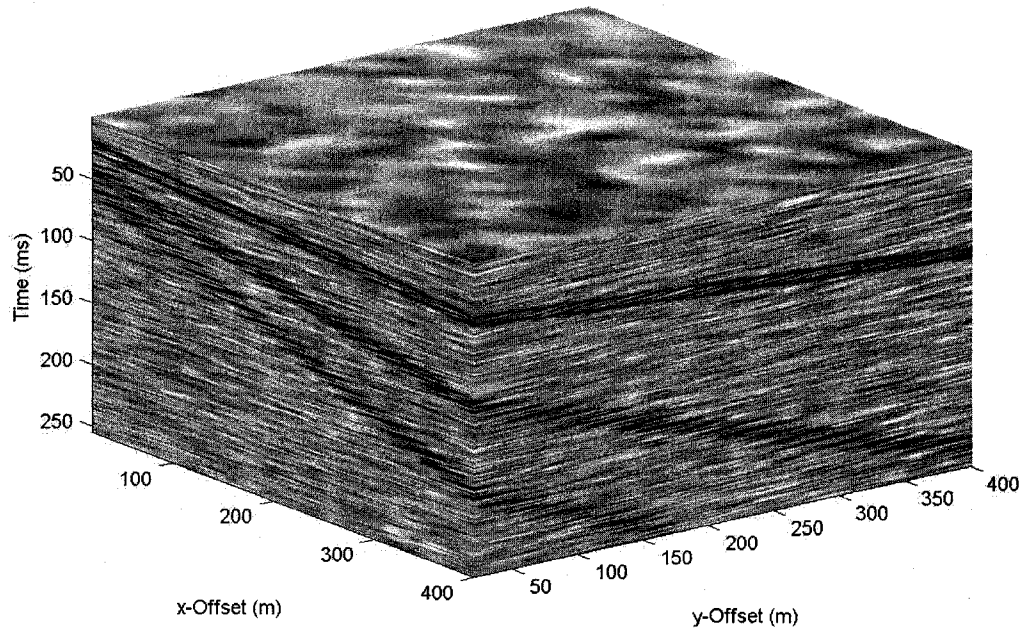
Figure 3.13: 3D view of a seismic section with three events (layers). Each plane may have different dips (α, β) relative to $x-$ and $y-$ axes.

Without loss of generality, we assume that the data structure **X** is a poststack data that means all the moveout corrections and stacking are already done on the data. In order to see how we can apply SVD on these data, let us first transform the signal s_m from time domain to frequency domain using Fourier transform:

$$s_m(t) = \frac{1}{2\pi} \sum_{j=1}^{N_f} s_m(\omega_j) e^{i\omega_j t}, \tag{3.15}$$

where $N_f = 2^{n-1}$ such that $n = \lceil \log_2(N) \rceil$ and $\lceil \; \rceil$ is the nearest integer function. Here we assign ω_{N_f} as the Nyquist frequency. Inserting equation (3.15) into equation (3.12), one finds

$$d_{k\ell}(t) = \sum_{m=1}^{L} \left(\frac{1}{2\pi} \sum_{j=1}^{N_f} s_{mk\ell}(\omega_j) e^{i\omega_j t} \right)$$

$$= \frac{1}{2\pi} \sum_{j=1}^{N_f} \left(\sum_{m=1}^{L} s_{mk\ell}(\omega_j) \right) e^{i\omega_j t}. \tag{3.16}$$

Recalling the Fourier transformation of $d_{k\ell}(t)$

$$d_{k\ell}(t) = \frac{1}{2\pi} \sum_{j=1}^{N_f} d_{k\ell}(\omega_j) e^{i\omega_j t}, \tag{3.17}$$

one concludes that (by combining equations 3.16 and 3.17)

$$d_{k\ell}(\omega_j) = \sum_{m=1}^{L} s_{mk\ell}(\omega_j), \quad j = 1, 2, \cdots, N_f. \tag{3.18}$$

Equation (3.18) states that similar to the time domain, every trace of the data structure in the frequency domain can also be found by adding all individual Fourier transformed signals $s_{mk\ell}(\omega_j)$. However, this has no new information by itself. One step further is to calculate the Fourier transform of the wavelet $w(t - \tau_{mk\ell})$ that is

$$
\begin{aligned}
w(t - \tau_{mk\ell}) &= \frac{1}{2\pi} \sum_{j=1}^{N_f} w(\omega_j) e^{i\omega_j(t - \tau_{mk\ell})} \\
&= \frac{1}{2\pi} \sum_{j=1}^{N_f} w(\omega_j) e^{i\omega_j t} e^{-i\omega_j \tau_{mk\ell}},
\end{aligned} \tag{3.19}
$$

and inserting it into equations (3.13) and (3.15) that leads to

$$s_{mk\ell}(\omega) = a_m w(\omega) e^{-i\omega \tau_{mk\ell}}, \tag{3.20}$$

where we drop the index j for simplicity. Inserting equation (3.20) into equation (3.18) and using the definition of $\tau_{mk\ell}$, equation (3.14), one finds the component of $(k, \ell)^{\text{th}}$ trace in the frequency domain as

$$
\begin{aligned}
d_{k\ell}(\omega) &= \sum_{m=1}^{L} a_m w(\omega) e^{-i\omega t_{0m}} e^{-i\omega \alpha_m x_k} e^{-i\omega \beta_m y_\ell} \\
&= \sum_{m=1}^{L} A_m(\omega) u_{mk}(\omega) v_{m\ell}(\omega),
\end{aligned} \tag{3.21}
$$

where $A_m(\omega) = a_m w(\omega) \exp(-i\omega t_{0m})$, u_{mk} and $v_{m\ell}$ are the kth and ℓ^{th} components of $\mathbf{u}_m$ and $\mathbf{v}_m$ vectors, respectively,

$$u_{mk} = [\mathbf{u}_m]_k = \exp(-i\omega \alpha_m x_k), \tag{3.22}$$

$$v_{m\ell} = [\mathbf{v}_m]_\ell = \exp(-i\omega \beta_m y_\ell). \tag{3.23}$$

Note that ω runs from ω_1 to ω_{N_f}, the Nyquist frequency. For a fixed frequency, ω, equation (3.21) can be written as

$$d_{k\ell} = \sum_{m=1}^{L} A_m u_{mk} v_{m\ell},$$ (3.24)

where $k = 1, 2, \cdots, M_x$ and $\ell = 1, 2, \cdots, M_y$. As a result, $d_{k\ell}$ is the $(k, \ell)^{\text{th}}$ component of a $M_x \times M_y$ matrix $\mathbf{X}_\omega$ that can be written as

$$\mathbf{X}_\omega = \sum_{m=1}^{L} A_m \mathbf{u}_m \mathbf{v}_m^T, \quad \omega = \omega_1, \ldots, \omega_{N_f},$$ (3.25)

where $\mathbf{u}_m = [u_m(x_1), \cdots, u_m(x_{M_x})]^T$ and $\mathbf{v}_m = [v_m(y_1), \cdots, v_m(y_{M_y})]^T$. Comparing with definition of SVD for a matrix, equation (2.1), one can interpret equation (3.25) as the singular value decomposition of $\mathbf{X}_\omega$ into two vectors $\mathbf{u}_m$ and $\mathbf{v}_m$ with singular value A_m. Therefore, equation (3.25) says that at each frequency the data matrix $\mathbf{X}_\omega$ can be written as the sum of its eigenimages. It is clear that the matrix decomposition (3.25) naturally follows from the Fourier transformation properties and so it treats any poststack data with zero or nonzero dip events in the same manner.

Starting from the first frequency and carrying procedure (3.25) along to the whole spectrum, ω_1 to ω_{N_f}, one can reconstruct the whole section using the calculated $\mathbf{X}_\omega$

$$\mathbf{X}_\omega = [\mathbf{X}_{\omega_1}, \mathbf{X}_{\omega_2}, \cdots, \mathbf{X}_{\omega_{N_f}}]^T.$$ (3.26)

As the final step, an inverse Fourier transform is required to obtain the original data in time domain, *t-xy*, i.e. $\mathbf{X} = \text{DFT}^{-1}(\mathbf{X}_\omega)$.

In practice, however, the matrix $\mathbf{X}_\omega$ with size $M_x \times M_y$, can be reconstructed by adding few of its eigenimages:

$$\widetilde{\mathbf{X}}_\omega \simeq \sum_{m=1}^{K} A_m \mathbf{u}_m \mathbf{v}_m^T,$$ (3.27)

where $K < L$. This approximation will be made again for each frequency in the spectrum to obtain the whole matrix $\widetilde{\mathbf{X}}$:

$$\widetilde{\mathbf{X}} = \text{DFT}^{-1}([\widetilde{\mathbf{X}}_{\omega_1}, \widetilde{\mathbf{X}}_{\omega_2}, \cdots, \widetilde{\mathbf{X}}_{\omega_{N_f}}]^T),$$ (3.28)

and after an inverse Fourier transformation the approximated matrix $\widetilde{\mathbf{X}}$ will be recovered in *t-xy* domain. It is interesting to note that the amount of attenuated noise can be increased by increasing the grid size, $M_x \times M_y$, and also decreasing K the number of summed eigenimages.

In order to see how efficient the *f-xy* method is, we return to the example that we discussed in section (3.4). Recalling Figure 3.9a that was a seismic section in *t-x* domain consists of three events with nonzero dips. As we found out there, the SVD method was not very efficient in recovering those events even after adding 10 eigenimages together, see Figure 3.11(b).

Here we consider a 3D seismic volume, $\mathbf{X}$, observed by $M_x \times M_y = 20 \times 20$ geophones that are distributed in a *xy*-plane. The data contains ~ 300 time samples and consists of thee events with nonzero dips, see Figure 3.13. Intersecting this volumetric data with a *y*-constant plane would produce a data very similar to Figure 3.9(a).

We now first transform data from *t-xy* domain to *f-xy* domain using Fourier transformation in time coordinate. Then we apply the SVD decomposition on the transformed data at a fixed frequency, ω, and calculate the approximated data $\widetilde{\mathbf{X}}_\omega$ using the first few eigenimages:

$$\widetilde{\mathbf{X}}_\omega = \sum_{i=1}^{K} \sigma_i \mathbf{u}_i \mathbf{v}_i^\dagger, \qquad (3.29)$$

where $K \ll \text{rank}(\widetilde{\mathbf{X}}_\omega)$. By calculating $\widetilde{\mathbf{X}}_\omega$ for all ω from ω_1 to ω_{N_f}, the Nyquist frequency, the 3D reconstructed matrix $\widetilde{\mathbf{X}}$ would be obtained. Finally we transform back to the *t-xy* domain. The result is reported in Figures 3.14-3.16 and 3.17.

Figure 3.14(a) represents the cross section of the original 3D data. In Figures 3.14(b), 3.15(b) and 3.16(b) we plot the reconstructed data using equation (3.29) for $K = 1, 2$ and 3, respectively. As shown, all three events are not fully recovered in panels 3.14(b) and 3.15(b), however, panel 3.16(b) contains almost the whole data. This can be seen through panels 3.14c)-3.16(c) that show the residuals for panels 3.14(b)-3.16(b), respectively. The efficiency of the *f-xy* analysis can be understood by plotting the singular values as function of the singular value index. In Figure 3.18(a) we plot the singular values in terms of the singular value indices at each frequency. It is clear that for all frequencies, the first three singular values are significantly larger than the others. This means that the most part of the observed signal is carried by the first three eigenimages. This fact is plotted in Figure 3.18(b)
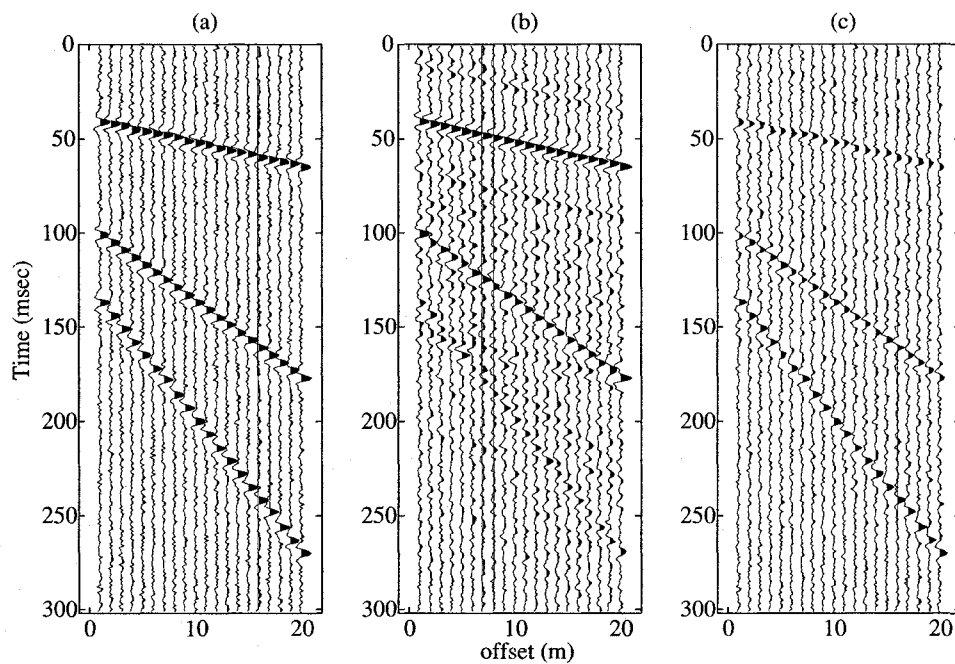
Figure 3.14: (a) The cross section of 3D data matrix composed from three events with nonzero dips. The data is also contaminated with an uncorrelated noise with standard deviation of 10% of maximum amplitude. (b) Reconstruction of the data matrix using *f-xy* method with the first eigenimage. See equation (3.29). (c) The residual, original data, panel (a), subtracted by reconstructed data given in panel (b).
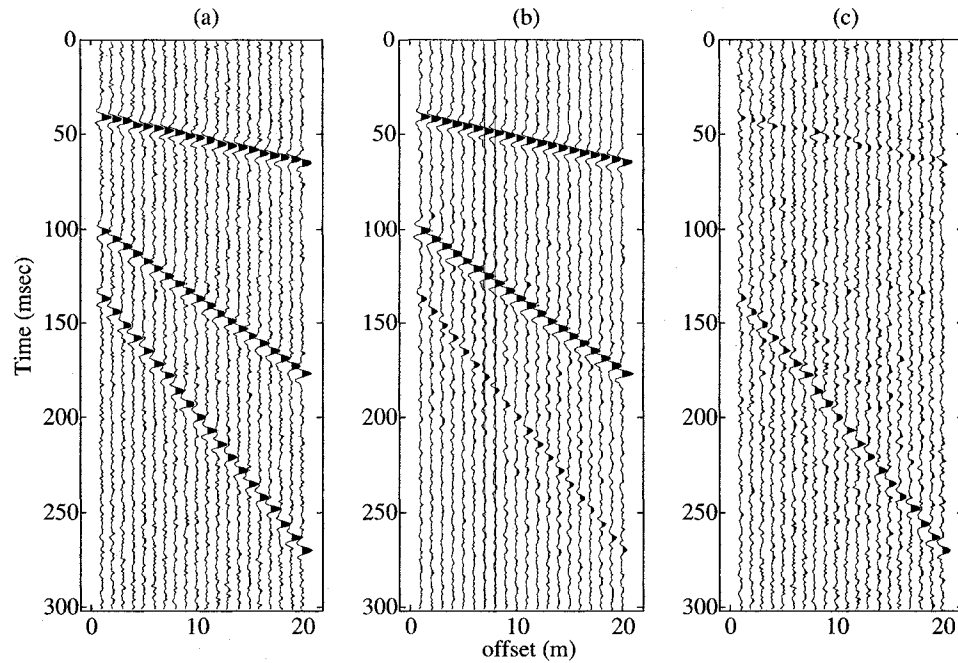
Figure 3.15: (a) Same as Figure 3.14(a). (b) Reconstruction of the data matrix using *f-xy* method with the first 2 eigenimages. (c) The residual, original data, panel (a), subtracted by reconstructed data given in panel (b).
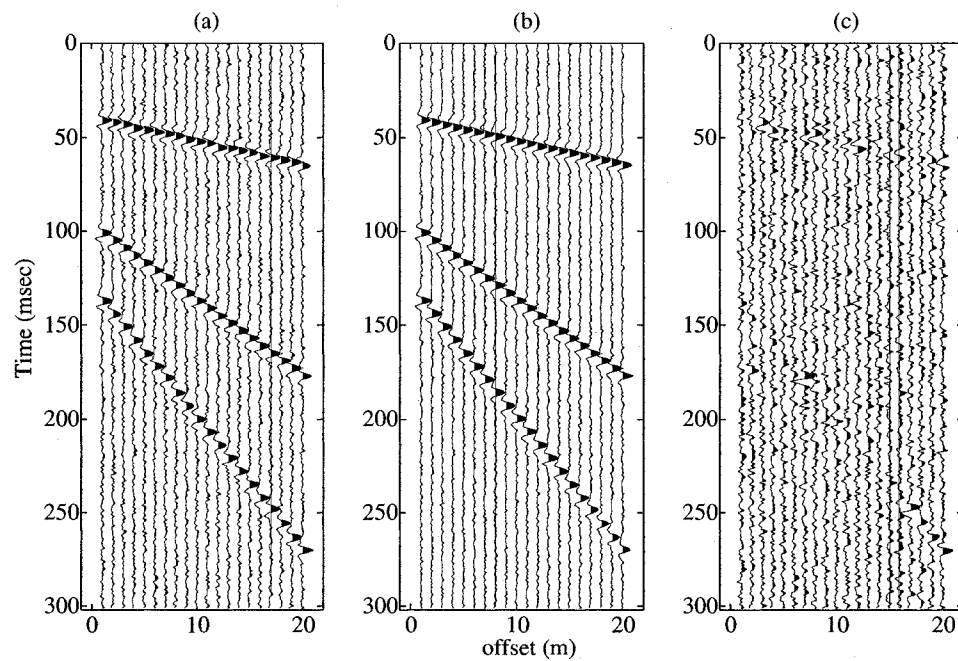
Figure 3.16: (a) Same as Figure 3.14(a). (b) Reconstruction of the data matrix using *f-xy* method with the first 3 eigenimages. (c) The residual, original data, panel (a), subtracted by reconstructed data given in panel (b).
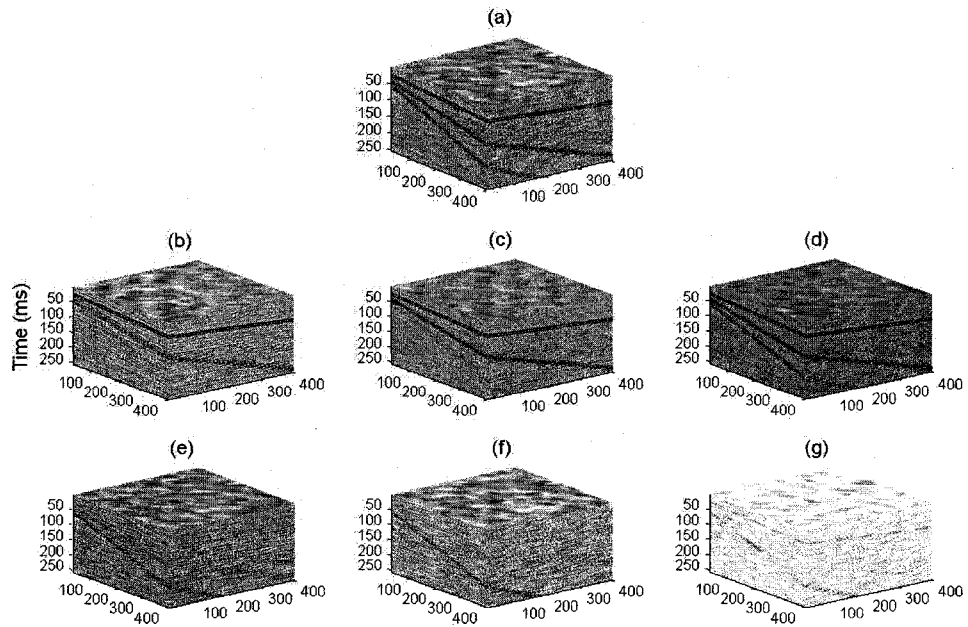
Figure 3.17: (a) 3D view of data matrix composed from three events with nonzero dips. The data is also contaminated with an uncorrelated noise with standard deviation of 10% of maximum amplitude. The left and the right axes are x-offset and y-offset in meters, respectively. (b) Reconstruction of the data matrix using *f-xy* method with the first eigenimage, (c) the first 2 eigenimages and (d) the first 3 eigenimages. See equation (3.29). (e) The residual, original data, panel (a), subtracted by reconstructed data given in panel (b). (f) subtracted by panel (c). (g) subtracted by panel (d).
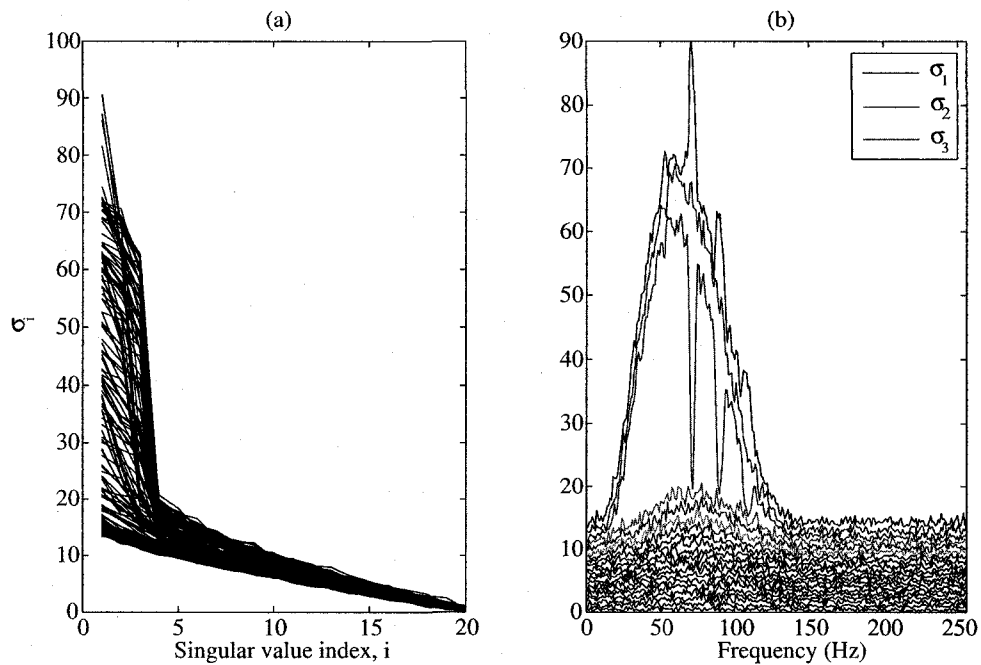
Figure 3.18: (a) The magnitude of the singular values σ as function of the singular value index for each frequency. (b) The magnitude of the singular values σ_i as function frequency.

that demonstrates the magnitude of singular values as function of frequency. As shown, the first three singular values (plotted in blue, green and red, respectively) dominate over a wide frequency range.

Figure 3.19 depicts the relative energy as function of frequency, see equation (3.30). Panels a, b and c represent the relative energy stored in the first eigenimage $(\mathcal{E}_1/\mathcal{E})$, the first two eigenimages $(\mathcal{E}_2/\mathcal{E})$ and the first three eigenimages $(\mathcal{E}_3/\mathcal{E})$, where

$$\frac{\mathcal{E}_k}{\mathcal{E}} = \frac{\sum_{i=1}^{k} \sigma_i^2}{\sum_{i=1}^{M_x} \sigma_i^2} \tag{3.30}$$

and $k = 1, 2$ and 3. As shown in Figure 3.19, the first three eigenimages contains a large fraction of the signals' energy. As a result, one would expect to reconstruct more or less the whole signal by adding the first three eigenimages as shown in Figure 3.16(b).

The efficiency of the *f-xy* analysis can also be examined by comparing Figure 3.16(b) with Figure 3.11(b). Here, the all three events are recovered after adding 3 eigenimages, while in Figure 3.11(b) the recovery wasn't successful even after adding 10 eigenimages.
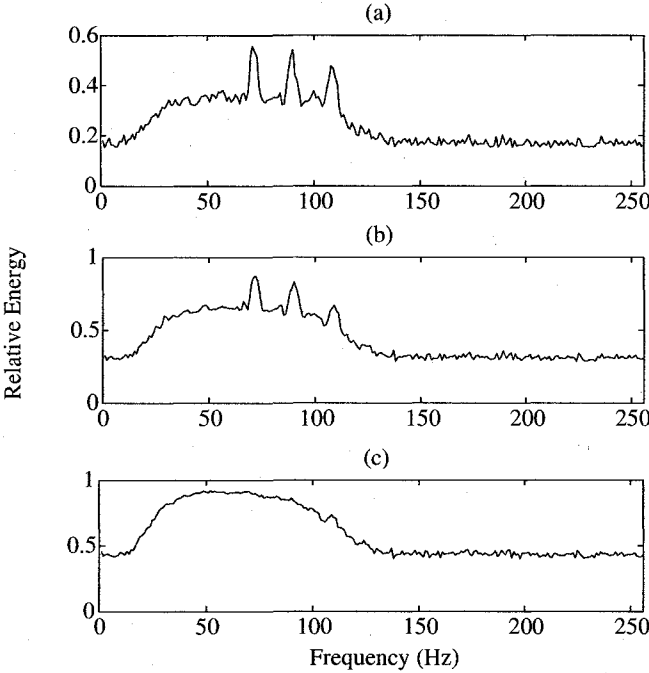
Figure 3.19: (a) The relative energy stored in the first eigenimage $(\mathcal{E}_1/\mathcal{E})$ (b) in the first two eigenimages $(\mathcal{E}_2/\mathcal{E})$ and (c) in the first three eigenimages $(\mathcal{E}_3/\mathcal{E})$, where E_k/E is given by equation (3.30).

3.6 Summary

In this chapter we demonstrated the SVD analysis on several synthetic data. We first considered a 2D (x-t) seismic section with three zero dip layers. We showed that after moveout correction, the SVD directly enhances the signal-to-noise (SNR) of data even with the first eigenimage. However, the SNR enhancement will be poor if no prior moveout correction applied. In section 3.4 we considered a poststack 3D data structure with three events (three layers). In general we assumed that each layer has different dip relative to the x and y directions. We demonstrated that a direct application of the SVD would not able to recover the data structure and so enhance the SNR. Following Trickett (2003), we introduced the f-xy eigenimage decomposition. In this method we first transform the data from t-xy domain to f-xy domain. In the frequency domain, we showed that the data matrix can be written as sum of the product of three matrices, similar to the SVD decomposition:

$$\mathbf{X}_\omega = \sum_{m=1}^{L} A_m \mathbf{u}_m \mathbf{v}_m^T. \tag{3.31}$$

See equation (3.25) for more detail. Such separability enabled us to reconstruct the data in the f-xy domain with the first few eigenimages. Then, we transformed the reconstructed data to the t-xy domain. The reconstructed data in the t-xy domain shows a fairly good SNR enhancement, see Figure 3.17. The flow chart for applying f-xy eigenimage decomposition is given in Figure 3.20.
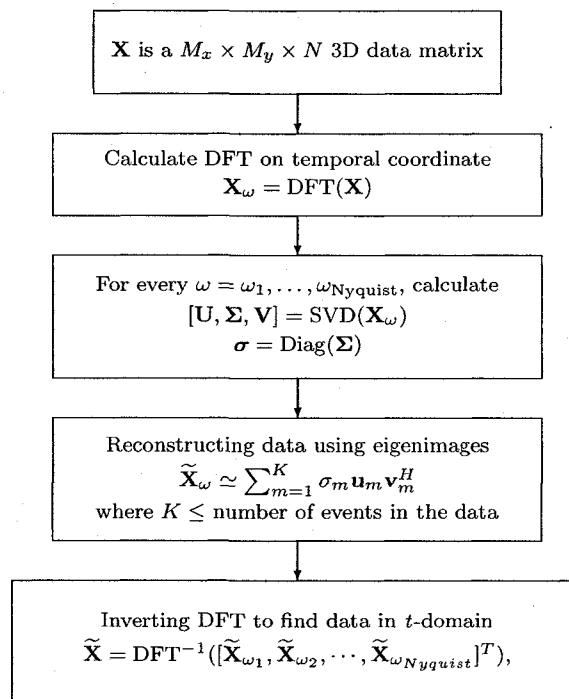
Figure 3.20: Flow chart of f-xy eigenimage decomposition.

The flow chart contains the following boxes:

X is a $M_x \times M_y \times N$ 3D data matrix

Calculate DFT on temporal coordinate
$$\mathbf{X}_\omega = \text{DFT}(\mathbf{X})$$

For every $\omega = \omega_1, \ldots, \omega_{\text{Nyquist}}$, calculate
$$[\mathbf{U}, \mathbf{\Sigma}, \mathbf{V}] = \text{SVD}(\mathbf{X}_\omega)$$
$$\sigma = \text{Diag}(\mathbf{\Sigma})$$

Reconstructing data using eigenimages
$$\widetilde{\mathbf{X}}_\omega \simeq \sum_{m=1}^{K} \sigma_m \mathbf{u}_m \mathbf{v}_m^H$$
where $K \leq$ number of events in the data

Inverting DFT to find data in t-domain
$$\widetilde{\mathbf{X}} = \text{DFT}^{-1}([\widetilde{\mathbf{X}}_{\omega_1}, \widetilde{\mathbf{X}}_{\omega_2}, \cdots, \widetilde{\mathbf{X}}_{\omega_{Nyquist}}]^T),$$

Chapter 4

Spatial and temporal analysis

For a temporal analysis of a given time series, the discrete Fourier transform (DFT) usually provides signal frequencies with acceptable resolutions. This is because of the fact that a time series is usually made of a large sample of time points, $N \sim \mathcal{O}(10^2 - 10^3)$. For spatial analysis, however, this may not be true. A multichannel time series is usually observed with a small number of detectors, $M \sim \mathcal{O}(10^1)$. As a result, a spatial DFT spectrum will yield low resolution and then less accurate results.

Array signal processing (or multichannel time series analysis) has been used for several decades in radar, sonar and seismic data analysis. A set of detectors that are spatially distributed at specific locations is usually considered as an array. These detectors receive and record incoming signals from sources in their field of view. Several techniques are proposed to analyze multichannel time series in order to provide higher spatial resolution. Schmidt (1981, 1986) developed the eigenstructure method called multiple signal classification (MUSIC) that is suitable for radar data.

The idea behind the MUSIC method is to separate the data structure into two orthogonal signal and noise subspaces. Therefore, any arbitrary eigenvector that is orthogonal to the noise subspace would be equal to a signal's eigenvector or to a linear combination of signal's eigenvectors. By browsing through a pool of possible eigenvectors, one can determine the signals' wave vector in high resolution. For more general situations, however, some smoothing procedures need to be done prior to the MUSIC power estimation.

In this chapter, following Schmidt (1986), Goldstein and Archuleta (1987) and Pillai (1989), we introduce MUSIC method in more detail. To illustrate its capability, we then apply the method on our seismic synthetic data set and compare with

DFT results.

4.1 The multichannel data structure: single source

Consider an array of M detectors that observe M samples of a quantity $\mathbf{Y}^H = [Y_1^*, Y_2^*, \cdots, Y_M^*]$ at a time t, where $t = 0, 1, \ldots, N - 1$. Here $()^H \equiv ()^{*T}$ indicates complex conjugate and matrix transpose. For example, Y_k represent a seismic time series or the variation of oil price during a year. Introducing a zero-mean parameter $\mathbf{X}^H = [X_1^*, X_2^*, \cdots, X_M^*]$, such that

$$X_k = Y_k - E\{Y_k\}, \quad k = 1, \cdots, M, \tag{4.1}$$

where $E\{\ \}$ represents the expectation value. For a single source problem, X_k can be written as

$$X_k = a_k s + e_k, \quad k = 1, \cdots, M, \tag{4.2}$$

where a_k is the amplitude of the arrived signal s in the kth detector. The variable s represent the signal wavefront that is common in all observed channels (detectors) and e_k $(k = 1, \cdots, M)$ are stationary, uncorrelated noise. For example for a plane wave wavefront $s \sim \exp(i\mathbf{k} \cdot \mathbf{x} - i\omega t)$ where $\mathbf{k}$ is the wave vector and ω is the angular frequency of the signal.

Since the noise is uncorrelated, one can write

$$E\{e_k\} = 0, \tag{4.3}$$

$$E\{e_j e_k\} = \sigma^2 \delta_{jk}, \tag{4.4}$$

$$E\{e_k s\} = 0, \tag{4.5}$$

where δ is the Kronecker delta function and σ^2 is the noise intensity. In general, the amplitude $a_k(\theta)$ which is also called mode amplitude, depends on the kth detector, i.e. it's position to the origin of the system, and direction of the arrived signal at kth detector, θ. The mode amplitude a_k can be zero, positive and/or negative complex value and may differ from channel to channel. Measuring the mode vector one can retrieve the incident angle of the signal to each detector.

The vectorial form of equation (4.2) can be written as

$$\mathbf{X} = \mathbf{a}s + \mathbf{e}, \tag{4.6}$$

where $\mathbf{X}^H = [X_1^*, \cdots, X_M^*]$ and $\mathbf{a}^H = [a_1^*, \cdots, a_M^*]$. The signal s is again the signal that is common in all channels, and $\mathbf{a}$ is the mode vector. The goal in MUSIC is to calculate angle of arrival, θ, wavenumber, or frequency of the signal from the eigenstructure of covariance matrix of the data

$$\mathbf{R} = E\{\mathbf{X}\mathbf{X}^H\}. \tag{4.7}$$

Seismic time series collected by M detectors from a single natural and/or artificial source is an example of the model (4.6). Radar data that observed by an array of antennas is another example of model (4.6). We will back to the radar data in Chapter 5.

Model (4.6) is restricted to a single signal s in all M components of the $\mathbf{X}$. In other words, all components of the vector $\mathbf{X}$ are common in one pattern. For most empirical data, however, this is not the case. In general, two or more signals are present in the $\mathbf{X}$ vector, e.g., $\mathbf{X} = \mathbf{a}_1 s_1 + \mathbf{a}_2 s_2 + \mathbf{e}$ where $\mathbf{a}_1$ and $\mathbf{a}_2$ are the amplitude vectors. In the next section we generalize the method for L signals presented in data.

4.2 Generalized Model for X

Assume that there are L signals ($L < M$) in the data. Introducing a $L \times 1$ vector $\mathbf{s}^H = [s_1^*, \cdots, s_L^*]$ as the signal vector. Therefore, for each component X_k ($k = 1, \cdots, M$) one needs L weighting coefficients a_{ki}, $i = 1, \cdots, L$ such that

$$\begin{aligned} X_k &= a_{k1}s_1 + a_{k2}s_2 + \cdots + a_{kL}s_L + e_k, \\ &= \sum_{i=1}^{L} a_{ki}s_i + e_k, \end{aligned} \tag{4.8}$$

or in compact form

$$\mathbf{X} = \mathbf{A}\mathbf{s} + \mathbf{e}; \tag{4.9}$$

where $\mathbf{A}$ is $M \times L$ ($L < M$) matrix:

$$\begin{pmatrix} X_1 \\ X_2 \\ \vdots \\ X_M \end{pmatrix} = \begin{pmatrix} a_{11} & a_{12} & \cdots & a_{1L} \\ a_{21} & a_{22} & \cdots & a_{2L} \\ \vdots & \vdots & \ddots & \vdots \\ a_{M1} & a_{M2} & \cdots & a_{ML} \end{pmatrix} \begin{pmatrix} s_1 \\ s_2 \\ \vdots \\ s_L \end{pmatrix} + \begin{pmatrix} e_1 \\ e_2 \\ \vdots \\ e_M \end{pmatrix} \tag{4.10}$$

The quantity a_{ki} is function of the array element locations and the angles of arrival. That is, $a_{ki}(\theta_i)$ is the response to the ith signal arrived at the kth detector by an angle of θ_i. As we mentioned before, the general interest in MUSIC is to calculate angles of arrival, θ, wavenumbers, or frequencies of the signals from the eigenstructure of covariance matrix of the data

$$
\begin{aligned}
\mathbf{R} &= E\{\mathbf{XX}^H\} \\
&= E\{(\mathbf{As}+\mathbf{e})(\mathbf{As}+\mathbf{e})^H\} = E\{(\mathbf{As}+\mathbf{e})(\mathbf{s}^H\mathbf{A}^H+\mathbf{e}^H)\} \\
&= E\left\{\mathbf{Ass}^H\mathbf{A}^H + \mathbf{Ase}^H + \mathbf{es}^H\mathbf{A}^H + \mathbf{ee}^H\right\} \\
&= E\{\mathbf{Ass}^H\mathbf{A}^H\} + E\{\mathbf{Ase}^H\} + E\{\mathbf{es}^H\mathbf{A}^H\} + E\{\mathbf{ee}^H\} \\
&= \mathbf{A}E\{\mathbf{ss}^H\}\mathbf{A}^H + \mathbf{A}E\{\mathbf{se}^H\} + E\{\mathbf{es}^H\}\mathbf{A}^H + E\{\mathbf{ee}^H\} \\
&= \mathbf{A}E\{\mathbf{ss}^H\}\mathbf{A}^H + \sigma^2\mathbf{I},
\end{aligned}
\tag{4.11}
$$

where $\mathbf{I}$ is the $M \times M$ identity matrix. In the last step we use result of equations (4.3) to (4.5). As a result, the $M \times M$ covariance matrix $\mathbf{R}$ can be written as

$$
\mathbf{R} = \mathbf{APA}^H + \sigma^2\mathbf{I},
\tag{4.12}
$$

where $\mathbf{P} = E\{\mathbf{ss}^H\}$ is a $L \times L$ matrix. The covariance matrix $\mathbf{P}$ is usually assumed to be nonsingular (as we assumed here) which is true for uncorrelated signals. For highly correlated signals (coherent signals), however, $\mathbf{P}$ is singular and the following procedure would need to be modified slightly. Two signals are coherent if one is scaled version of the other one. In other words, they change simultaneously (same phase). See Pillai (1989) for more detail on the case of coherent signals.

The positive definite covariance matrix $\mathbf{R}$ can be written as

$$
\mathbf{R} = \mathbf{APA}^H + \sigma^2\mathbf{I} = \mathbf{U\Lambda U}^H,
\tag{4.13}
$$

where $\mathbf{U}$ is the unitary matrix of eigenvectors and $\mathbf{\Lambda} = \text{diag}\{\lambda_1, \lambda_2, \ldots, \lambda_M\}$ is a diagonal matrix of eigenvalues that are ordered descendingly, i.e. $\lambda_1 \geq \lambda_2 \geq \ldots \geq \lambda_M > 0$. Furthermore, from equation (4.12), it is clear that any vector that is orthogonal to $\mathbf{A}$ is an eigenvector of $\mathbf{R}$ with eigenvalue σ^2

$$
\mathbf{Rv} = \sigma^2\mathbf{v}, \quad \text{if} \quad \mathbf{A}^H\mathbf{v} = 0.
\tag{4.14}
$$

In fact, there are $M - L$ of such vectors that are linearly independent. This can be understood by noting that the $M \times M$ matrix $\mathbf{APA}^H$ is a singular matrix with rank L which is smaller than M. This means that the first L eigenvalues of the matrix $\mathbf{APA}^H$ are nonzero and the rest $M - L$ eigenvalues are zero. Furthermore, since $\mathbf{APA}^H$ is singular, its determinant must be equal to zero, i.e.

$$||\mathbf{APA}^H|| = ||\mathbf{R} - \sigma^2\mathbf{I}|| = 0. \tag{4.15}$$

From the RHS of equation (4.15) it is clear that equation (4.15) holds if and only if σ^2 is equal to one of eigenvalues of the covariance matrix $\mathbf{R}$. However, the product of $\mathbf{APA}^H$ is nonnegative definite and requires σ^2 to be equal to the minimum eigenvalue of the data covariance matrix $\mathbf{R}$:

$$\sigma^2 = \lambda_{\min}. \tag{4.16}$$

As a result, the form of the diagonal matrix $\mathbf{\Lambda}$ will be

$$\mathbf{\Lambda} = \begin{pmatrix} \lambda_1 & & & & & & 0 \\ & \ddots & & & & & \\ & & \lambda_L & & & & \\ & & & \sigma^2 & & & \\ & & & & \ddots & & \\ 0 & & & & & \sigma^2 \end{pmatrix}, \tag{4.17}$$

$$\underbrace{\hphantom{\lambda_L}}_{L} \underbrace{\hphantom{\sigma^2\sigma^2}}_{M-L}$$

Since the matrix $\mathbf{APA}^H$ has rank $L < M$, the minimum eigenvalue $\lambda_{\min}$ will repeat $M - L$ times. This is clear by noting that equation (4.12) requires the eigenvalues of $\mathbf{R}$ and $\mathbf{APA}^H = \mathbf{R} - \lambda_{\min}\mathbf{I}$ to differ by $\lambda_{\min}$. Since the $M - L$ eigenvalues of $\mathbf{APA}^H$ are zero, then according to equation (4.17), the $M - L$ eigenvalues of $\mathbf{R}$ must be $\lambda_{\min}$, i.e.

$$\lambda_1 \geq \lambda_2 \geq \ldots \geq \lambda_L > \overbrace{\lambda_{\min} = \ldots = \lambda_{\min}}^{q=M-L}. \tag{4.18}$$

Therefore, the number of incident signals can be estimated from

$$L = M - q, \tag{4.19}$$

where q represents the multiplicity of the smallest eigenvalue, $\lambda_{\min}$. In practice,

however, the values of q and L are approximate, because for practical data the eigenvalues of the covariance matrix $\mathbf{R}$ will be

$$\lambda_1 \geq \lambda_2 \geq \ldots \geq \lambda_L \geq \lambda_{L+1} \geq \lambda_{L+2} \geq \ldots \geq \lambda_M. \tag{4.20}$$

So, if the number of incident signals are not known, at one point we should estimate L.

4.2.1 The signal and noise subspaces

The $M \times M$ covariance matrix of the data, $\mathbf{R}$, has M eigenvectors, $\mathbf{u}_k$, that satisfy

$$\mathbf{R}\mathbf{u}_k = \lambda_k \mathbf{u}_k, \quad k = 1, \ldots, M. \tag{4.21}$$

Combining equation (4.12) with (4.21), one finds

$$(\mathbf{A}\mathbf{P}\mathbf{A}^H + \sigma^2 \mathbf{I})\mathbf{u}_k = \lambda_k \mathbf{u}_k, \tag{4.22}$$

or

$$\mathbf{A}\mathbf{P}\mathbf{A}^H \mathbf{u}_k = (\lambda_k - \sigma^2)\mathbf{u}_k,$$
$$= \begin{cases} (\lambda_k - \sigma^2)\mathbf{u}_k & \text{if } k \leq L \\ 0 & \text{if } k > L \end{cases} \tag{4.23}$$

Therefore, the M dimensional Hilbert space that is spanned by M eigenvectors of $\mathbf{R}$ can be divided in two subspaces: the signal subspace and the noise subspace, i.e.

$$\mathbf{R} = \mathbf{U}_S \mathbf{\Lambda}_S \mathbf{U}_S^H + \mathbf{U}_N \mathbf{\Lambda}_N \mathbf{U}_N^H, \tag{4.24}$$

where $\mathbf{\Lambda}_S = \text{diag}\{\lambda_1, \lambda_2, \ldots, \lambda_L\}$ and $\mathbf{\Lambda}_N = \sigma^2 \mathbf{I}$. Equation (4.23) shows that the noise subspace has an interesting property that is

$$\mathbf{A}\mathbf{P}\mathbf{A}^H \mathbf{u}_k = 0, \quad k = L+1, \ldots, M, \tag{4.25}$$

or

$$\mathbf{A}^H \mathbf{u}_k = 0, \quad k = L+1, \ldots, M. \tag{4.26}$$
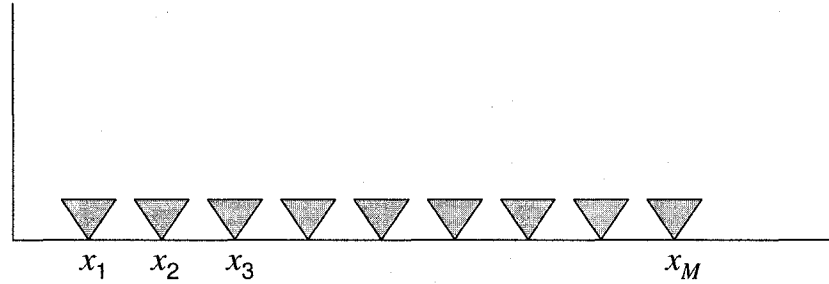
Figure 4.1: A linear array that all the detectors are placed along a line. x_m; $m = 1, \ldots, M$, represents the position of each detector from the coordinate's origin.

The above equation states that the eigenvectors associated with noise subspace are orthogonal to the incident signal vectors. The property (4.26) is the key property in the theory of MUSIC. To determine the signal characteristics, one needs to search for vectors a which have minimum projection in the noise subspace.

For a linear array, as shown in Figure 4.1, the mode vector a may be chosen as

$$\mathbf{a}(k) = \frac{1}{\sqrt{M}}[e^{ikx_1}, e^{ikx_2}, \ldots, e^{ikx_M}]^T, \qquad (4.27)$$

where k represents the wavenumber with value $k = \omega \cos(\theta)/v$, where ω is the wave frequency, v is the velocity of wave in the medium and θ specifies direction of wave propagation. Here x_m, $m = 1, \ldots, M$, is the position of each detector from the coordinate's origin. Depending on the quantity if interest, the above method can be performed to determine the signal's wavenumber k and/or signal's arrival directions θ. For signal arrival angles, one may write equation (4.27) as

$$\mathbf{a}(\theta) = \frac{1}{\sqrt{M}}[e^{i\cos(\theta)d_1}, e^{i\cos(\theta)d_2}, \ldots, e^{i\cos(\theta)d_M}]^T, \qquad (4.28)$$

where $d_j = x_m/(\lambda/2\pi)$ and λ is the signal wavelength. For an uniform linear array where $d_m = m\, d$, the mode vector, equation (4.28), simplifies to

$$\mathbf{a}(\theta) = \frac{1}{\sqrt{M}}[e^{i\phi}, e^{2i\phi}, \ldots, e^{iM\phi}]^T, \qquad (4.29)$$

where $\phi = d\cos(\theta)$ and d is the normalized distance (by $\lambda/2\pi$) between each detector. Introducing the noise matrix

$$\mathbf{U}_N = [\mathbf{u}_{L+1}, \ldots, \mathbf{u}_M],\tag{4.30}$$

the power in MUSIC is defined by some investigators as (Schmidt, 1986; Pillai, 1989)

$$P_{\text{MUSIC}} = \frac{1}{\mathbf{a}^H \mathbf{U}_N \mathbf{U}_N^H \mathbf{a}},\tag{4.31}$$

or

$$P_{\text{MUSIC}} = \frac{\mathbf{a}^H \mathbf{a}}{\mathbf{a}^H \mathbf{U}_N \mathbf{U}_N^H \mathbf{a}},\tag{4.32}$$

as defined by others (Iwata et al., 2001; Krim and Viberg, 1996). Equivalently one can find vectors $\mathbf{a}$ that lie in the signal subspace, i.e. that have maximum projection in the signal subspace. However, finding the minimum projection onto the noise subspace provides a more precise measurement of the incident signal's characteristic (Pillai, 1989).

4.3 Smoothing

In a more general scenario where sources are not completely uncorrelated, the MUSIC spectrum may fail to resolve the signal wavenumbers and/or arrival angles with acceptable resolutions. This can be understood by noting that if there are ℓ ($< L$) coherent signals in the data, the signal covariance matrix $\mathbf{P}$ will be singular with multiplicity ℓ. This results in $\mathbf{a}(k)^H \mathbf{U}_N \neq 0$ for any k that reduces the resolving power of MUSIC for closely spaced and/or correlated signals (Krim and Proakis, 1994).

One way to get around this problem is the so called forward-backward averaging of the data covariance matrix. The idea is to induce a phase difference among those coherent signals in order to de-correlate them. For uniform linear array the phase difference can be induced by multiplying the mode vector by $e^{-i(M+1)\phi}$, i.e.

$$\begin{aligned}
\mathbf{a}_B(\theta) &= e^{-i(M+1)\phi}[e^{i\phi}, e^{2i\phi}, \ldots, e^{iM\phi}]^T/\sqrt{M}, \\
&= [e^{-iM\phi}, \ldots, e^{-2i\phi}, e^{-i\phi}]^T/\sqrt{M},
\end{aligned}\tag{4.33}$$
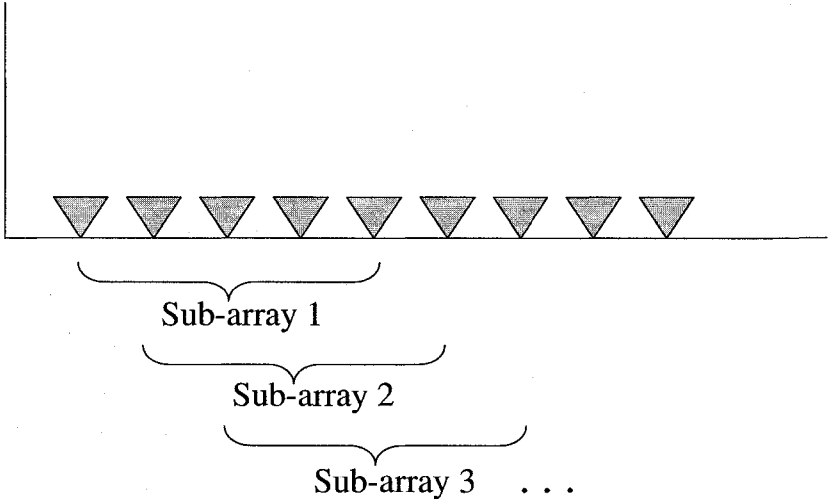
Figure 4.2: Schematic presentation of spatial smoothing technique: splitting the array into several identical subarrays.

where $\mathbf{a}_B(\theta)$ represents the backward mode vector. See Krim and Proakis (1994) for example. The backward covariance matrix will be then

$$\mathbf{R}_B = \mathbf{A}\mathbf{\Phi}^{-(M+1)}\mathbf{P}\mathbf{\Phi}^{-(M+1)}\mathbf{A}^H + \sigma^2\mathbf{I}, \tag{4.34}$$

where $\mathbf{\Phi}$ is a $L \times L$ diagonal matrix with element $e^{i\phi_l}$, $l = 1, \ldots, L$ and ϕ_l is the phase for the lth signal.

In more general approach, however, the forward-backward covariance matrix is calculated by

$$\mathbf{R}_{FB} = \frac{1}{2}(\mathbf{X}_F\mathbf{X}_F^H + \mathbf{X}_B\mathbf{X}_B^H), \tag{4.35}$$

where

$$\mathbf{X}_F = [X_1, X_2, \ldots, X_M]^T, \tag{4.36}$$

$$\mathbf{X}_B = [X_M, X_{M-1}, \ldots, X_1]^H. \tag{4.37}$$

The forward-backward smoothing is very efficient when there are only two coherent signals in the data. In a more general cases, however, where more than two correlated sources are present, forward-backward averaging fails to increase resolutions (Wiener, 1949). A more efficient way that is called spatial smoothing technique first introduced for uniform linear array by Wiener (1949) and then extended for more general configurations by Evans et al. (1982), Shan et al. (1985) and Friedlander and Weiss (1992). Such spatial smoothing induces a random phase modulation that de-correlates the coherent signals. The technique is to split the array into a number of overlapping subarrays as shown in Figure 4.2. Then a covariance matrix for each subarray will be calculated and averaged over all of them:

$$\widehat{\mathbf{R}} = \sum_{j=1}^{M-K+1} \mathbf{X}_j\mathbf{X}_j^H/(M - K + 1), \tag{4.38}$$

where $\widehat{\mathbf{R}}$ represents the smoothed covariance matrix and

$$\mathbf{X}_j = [X_j, X_{j+1}, \ldots, X_{j+K-1}]^T. \tag{4.39}$$

Here K ($\leq M$) represents the number of detectors in the subarrays. For example, in Figure 4.2, $K = 5$. The value for K is arbitrary and can be chosen based on the data. We note that the smoothed covariance matrix $\widehat{\mathbf{R}}$ has dimension K (i.e. a

$K \times K$ matrix) rather than M. As a result, the noise matrix (4.30) will be modified as

$$\widehat{\mathbf{U}}_{N} = [\mathbf{u}_{L+1}, \ldots, \mathbf{u}_{K}], \quad K \leq M. \tag{4.40}$$

Therefore, the MUSIC power will reduce to

$$P_{\text{MUSIC}} = \frac{1}{\mathbf{a}^{H} \widehat{\mathbf{U}}_{N} \widehat{\mathbf{U}}_{N}^{H} \mathbf{a}}, \tag{4.41}$$

or

$$P_{\text{MUSIC}} = \frac{\mathbf{a}^{H} \mathbf{a}}{\mathbf{a}^{H} \widehat{\mathbf{U}}_{N} \widehat{\mathbf{U}}_{N}^{H} \mathbf{a}}. \tag{4.42}$$

In summary, in order to apply the MUSIC method on multichannel time series, one may follow the flow chart shown in Figure 4.3.

4.4 Synthetic data

In this section we are going to examine the MUSIC method on the seismic synthetic data that we introduced in a previous chapter. We consider a seismic section consisting of 3 events such that each event has a constant dip across the section. The data is observed by 20 geophones distributed uniformly in the x-axis (with 20 m apart) where each receiver records $\sim$ 300 time samples.

In order to show how the smoothing procedure is important, we calculate the MUSIC power spectrum for different subarrays. Results are shown in Figure 4.4. Figures 4.4(a) to 4.4(d) represent the calculated power spectrum (in dB units) after spatial smoothing with twelve ($K = 8$), eight ($K = 12$), four ($K = 8$), and two ($K = 18$) subarrays, respectively. It is clear that an optimum value for K should be chosen in order to get the best results. The bigger subarray, Figure 4.4(d), would produce a very noisy result while the smaller subarray, Figure 4.4(a), is lacking a good resolving power. The latter can be understood from the fact that for a small subarray the effective aperture of the array is reduced, since the subarrays are smaller than the original array. This is known as a shortcoming with spatial smoothing in array signal processing (Krim and Proakis, 1994). We note that in the above analysis, we first transform the data from time domain to the frequency domain using 1-D DFT. Then a spectral smoothing is applied on the frequency domain by applying a Hamming window with length $\ell = 15$, see equation (4.43) below for more detail.

$$\mathbf{X} = [X_1, X_2, \ldots, X_M]$$

Calculating the covariance matrix, $\widehat{\mathbf{R}}$,
using the smoothing procedure

$$\widehat{\mathbf{R}} = \sum_{j=1}^{M-K+1} \mathbf{X}_j \mathbf{X}_j^H / (M - K + 1)$$

$$\mathbf{X}_j = [X_j, X_{j+1}, \ldots, X_{j+K-1}]^T, \quad K \leq M$$

Calculating eigenvalues and eigenvectors of $\widehat{\mathbf{R}}$

$$\mathbf{U} = \text{Eigenvector}(\widehat{\mathbf{R}})$$

Choosing L (= number of signals)
in order to make noise matrix

$$\mathbf{U}_N = [\mathbf{u}_{L+1}, \ldots, \mathbf{u}_K]^T$$

Introducing

$$\mathbf{a}(k) = [\exp(ikx_1), \exp(ikx_{L+2}), \ldots, \exp(ikx_M)]^T, \quad -k_{\max} \leq k \leq k_{\max}$$

Calculating MUSIC power

$$P(k) = \mathbf{a}^H \mathbf{a} (\mathbf{a}^H \mathbf{U}_N \mathbf{U}_N^H \mathbf{a})^{-1}$$

Plot $P(k)$ for $-k_{\max} \leq k \leq k_{\max}$
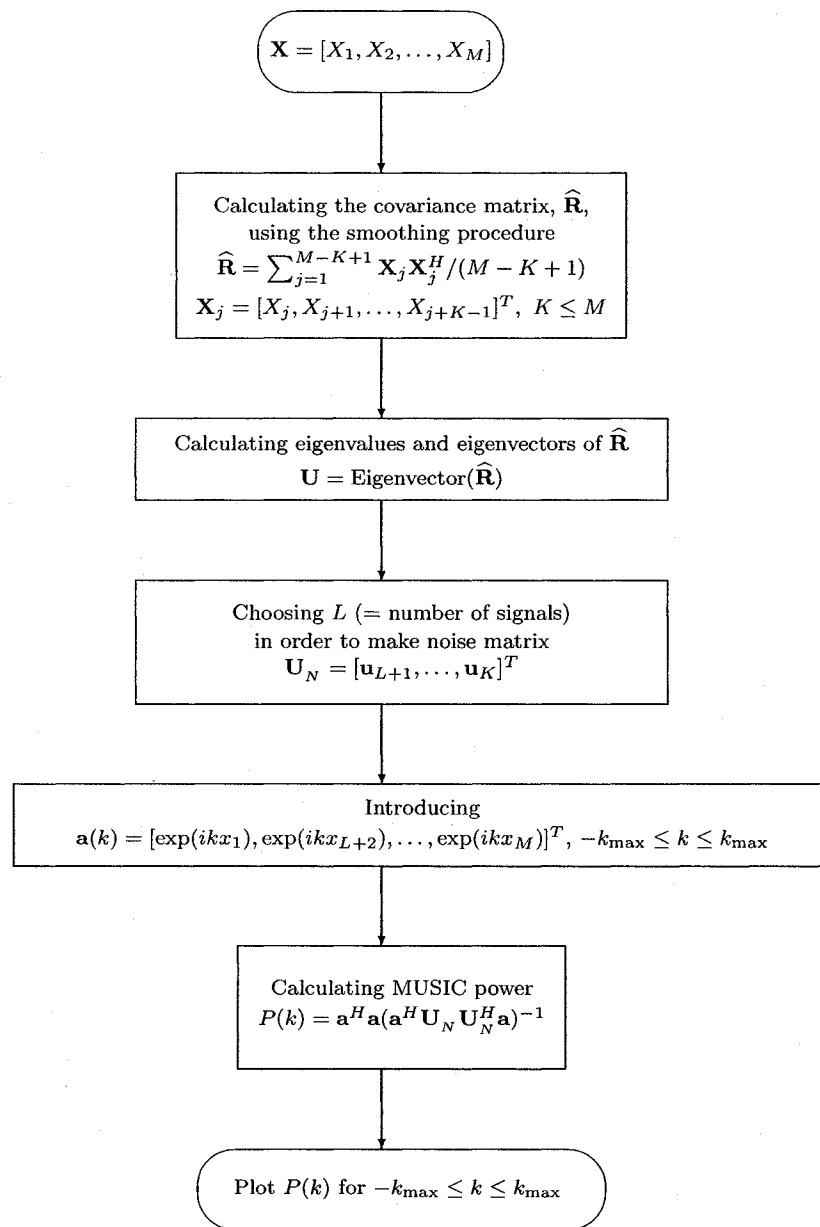
Figure 4.3: Flow chart of implementing MUSIC method.
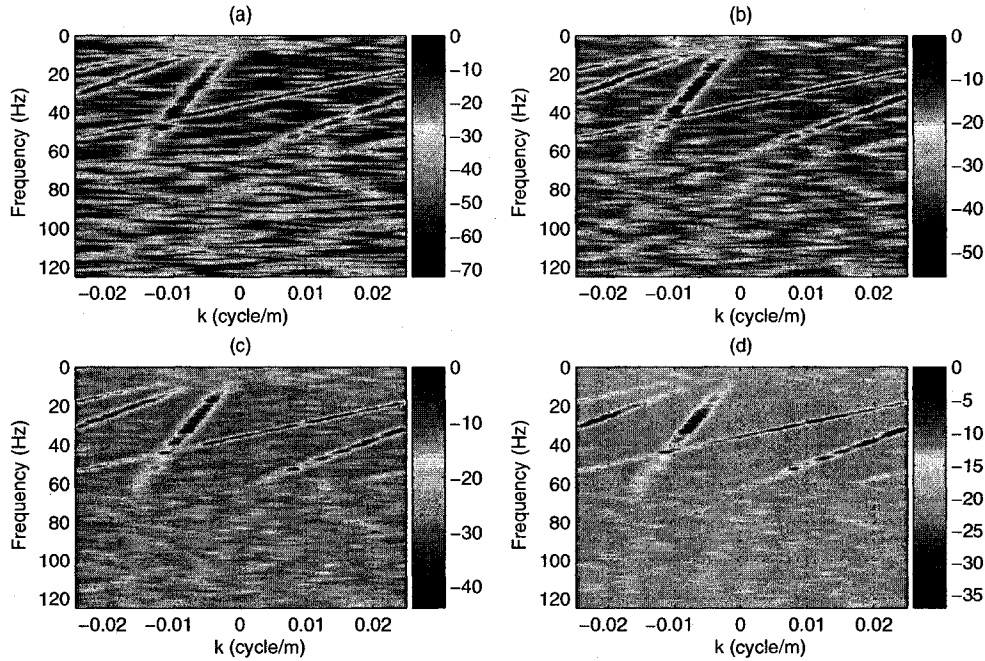
Figure 4.4: MUSIC power spectra (in dB units) of the synthetic seismic section. The spatial smoothing is implemented with different subarrays: (a) twelve subarrays or $K = 8$, (b) eight subarrays or $K = 12$, (c) four subarrays or $K = 16$ and (d) two subarrays or $K = 18$. For all cases $L = 4$. See equation (4.40).

Using such windowing functions is required to reduce the effects of the leakage that occurs during a Fourier analysis of the data. It is well known that there are some leakage amounts to spectral information from the DFT that are appearing at the wrong frequencies. If one could perform a Fourier analysis on a signal that runs on forever, the results would represent the exact frequencies and their amplitudes as they present in the signal. Such analysis, however, is impossible. Therefore, one has to truncate the data at some point. A sharp truncation of the data causes the leakage in the power spectrum. Although the leakage cannot be eliminated completely, by applying a smooth windowing one can minimize its effect. As a result, windowing will enhance the ability of an DFT to extract spectral data from signals.

It is necessary to note that Figure 4.4 shows six obvious lines while the original data structure is constructed from three linear events. This is due to the temporal/spatial aliasing. Aliasing is an artifact that usually happens when a continues signal being sampled. In general the sampling frequency differs from the signal frequency that causes the high frequency components aliased with low frequency ones during signal reconstruction. However, a closer look reveals that there are only three lines with distinct slopes. Each slope represent the phase velocity of the signal,
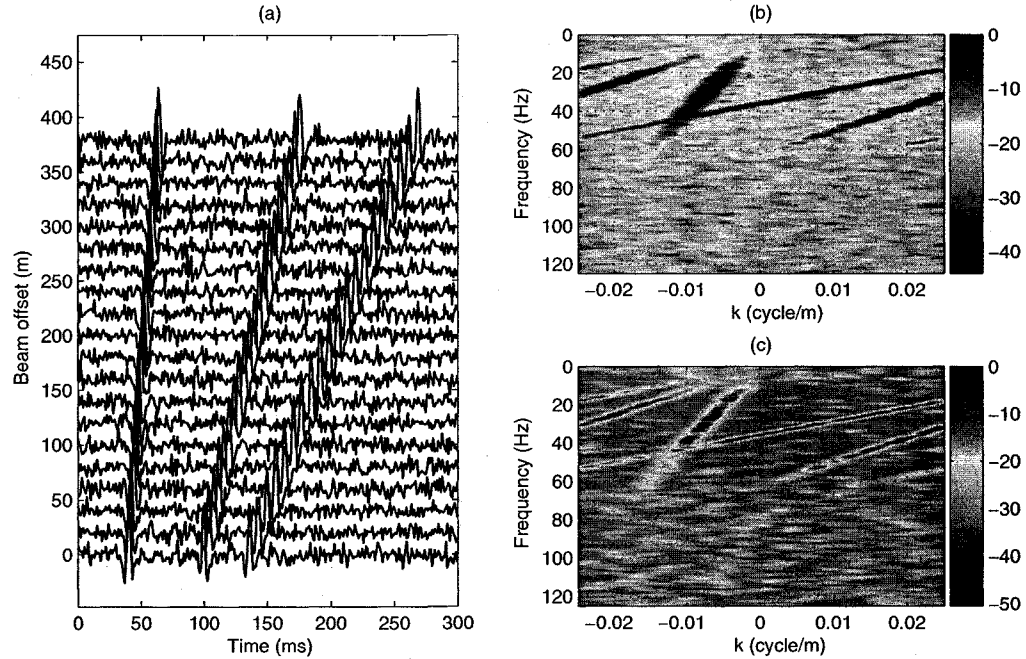
Figure 4.5: Comparing the 2D periodogram (in dB units) calculated by DFT with that of produced by MUSIC. (a) Representing the seismic section with three events. (b) DFT power spectrum. (c) The spatially smoothed MUSIC power spectrum ($K = 14$).

$v = \omega/k$, where $\omega = 2\pi f$ is the angular frequency. Therefore, there are only three true signals in Figure 4.4.

Finally, we would like to compare the power spectrum produced by MUSIC with one that is calculated by DFT. Figure 4.5(a) shows the synthetic seismic section containing three events with nonzero dips. In Figure 4.5(b), we plot the 2D periodogram of the section calculated by 2D DFT. The computed 2D periodogram then smoothed with by Hamming window with length $\ell = 15$:

$$w(j + 1) = 0.54 - 0.46\cos(2\pi\frac{j}{\ell - 1}); \quad j = 0, 1, \ldots, \ell - 1. \tag{4.43}$$

See Chatfield (1991) for more detail. We will discuss this point further in the next chapter. The MUSIC power spectrum that is spatially smoothed with six subarrays ($K = 14$), is shown in Figure 4.5(c). Similar to Figure 4.4, the frequency domain is calculated by 1-D DFT and smoothed by a Hamming window with length $\ell = 15$. Clearly the MUSIC method provides results with better resolution and less noise.

4.5 Summary

In this chapter we introduced the MUSIC method for spatial analysis. As we discussed earlier, Fourier analysis would not provide the result with acceptable resolution due to the small number of data points in the spatial coordinate (same as number of detectors). The MUSIC method is based on a set of eigenvectors of the data covariance matrix with corresponding eigenvalues that are more or less equal to the noise level in the input data. Unlike the DFT method, the MUSIC method can be used for data with a low signal-to-noise ratio to obtain very high frequency resolution.

As a final remark, in Figure 4.6 we present the flow chart for f-k analysis of a given data $\mathbf{X}$ in t-x domain, implementing the MUSIC method on spatial coordinate along with DFT on the temporal coordinate.

$$\mathbf{X} = [X_1, X_2, \ldots, X_M] \text{ in } (t, x) \text{ domain}$$

Transforming
$$\mathbf{X}_\omega = [X_1, X_2, \ldots, X_M]$$
from (t, x) domain to (ω, x) domain

Calculating the covariance matrix, $\widehat{\mathbf{R}}_\omega$,
using the smoothing procedure
$$\widehat{\mathbf{R}}_\omega = \sum_{j=1}^{M-K+1} \mathbf{X}_{\omega j} \mathbf{X}_{\omega j}^H / (M - K + 1)$$
$$\mathbf{X}_{\omega j} = [X_j, X_{j+1}, \ldots, X_{j+K-1}]^T, \ K \leq M$$

Calculating eigenvalues and eigenvectors of $\widehat{\mathbf{R}}_\omega$
$$\mathbf{U}_\omega = \text{Eigenvector}(\widehat{\mathbf{R}}_\omega)$$

Choosing L (= number of signals)
in order to make noise matrix
$$\mathbf{U}_{\omega_N} = [\mathbf{u}_{L+1}, \ldots, \mathbf{u}_K]^T$$

Introducing
$$\mathbf{a}(k) = [\exp(ikx_1), \exp(ikx_{L+2}), \ldots, \exp(ikx_M)]^T, \ -k_{\max} \leq k \leq k_{\max}$$

Calculating MUSIC power
$$P(k, \omega) = \mathbf{a}^H \mathbf{a} (\mathbf{a}^H \mathbf{U}_{\omega_N} \mathbf{U}_{\omega_N}^H \mathbf{a})^{-1}$$
for $-k_{\max} \leq k \leq k_{\max}$ and $1 \leq \omega \leq \omega_{\text{Nyquist}}$

Implementing spectral smoothing
using Hamming window, W
$$P(k, \omega) = \text{conv2}(w, P(k, \omega))$$

Plot $P(k, \omega)$ for $-k_{\max} \leq k \leq k_{\max}$
and $1 \leq \omega \leq \omega_{\text{Nyquist}}$

Figure 4.6: Flow chart of implementing MUSIC method with spectral smoothing.

Chapter 5

Spatial and temporal analysis: Application to real radar data

The Super Dual Auroral Radar Network (SuperDARN) is a network of high frequency (HF) radars that monitors ionospheric plasma convection of the northern and southern polar regions. This network currently consists of 9 radars in the northern hemisphere and 6 radars in the southern hemisphere. The operating frequency of the SuperDARN radars is between 8 and 20 MHz. The network records the Doppler velocity of ionospheric plasma along the radar beam.

The pulsations in the Earth's magnetic and electric field are often detected with these radars.

This chapter investigates the spatial and temporal analysis of a field line resonance event recorded by a single radar of SuperDARN.

5.1   Field Line Resonance

During dark nights near the north or south pole, a varying colorful light explores a wide area of the sky. This so called aurora is well known as the interaction of the Earth's magnetosphere with the solar wind. The ionized and magnetized gas outflow from the Sun, travels as a wind and affects the planetary environments by transporting energy into their magnetospheres.

The solar wind that originates from the solar corona, is a neutral plasma composed of protons and electrons with densities on the order of 10 cm^{-3} at the Earth. The solar wind plasma carries the Sun's magnetic field that has an average strength
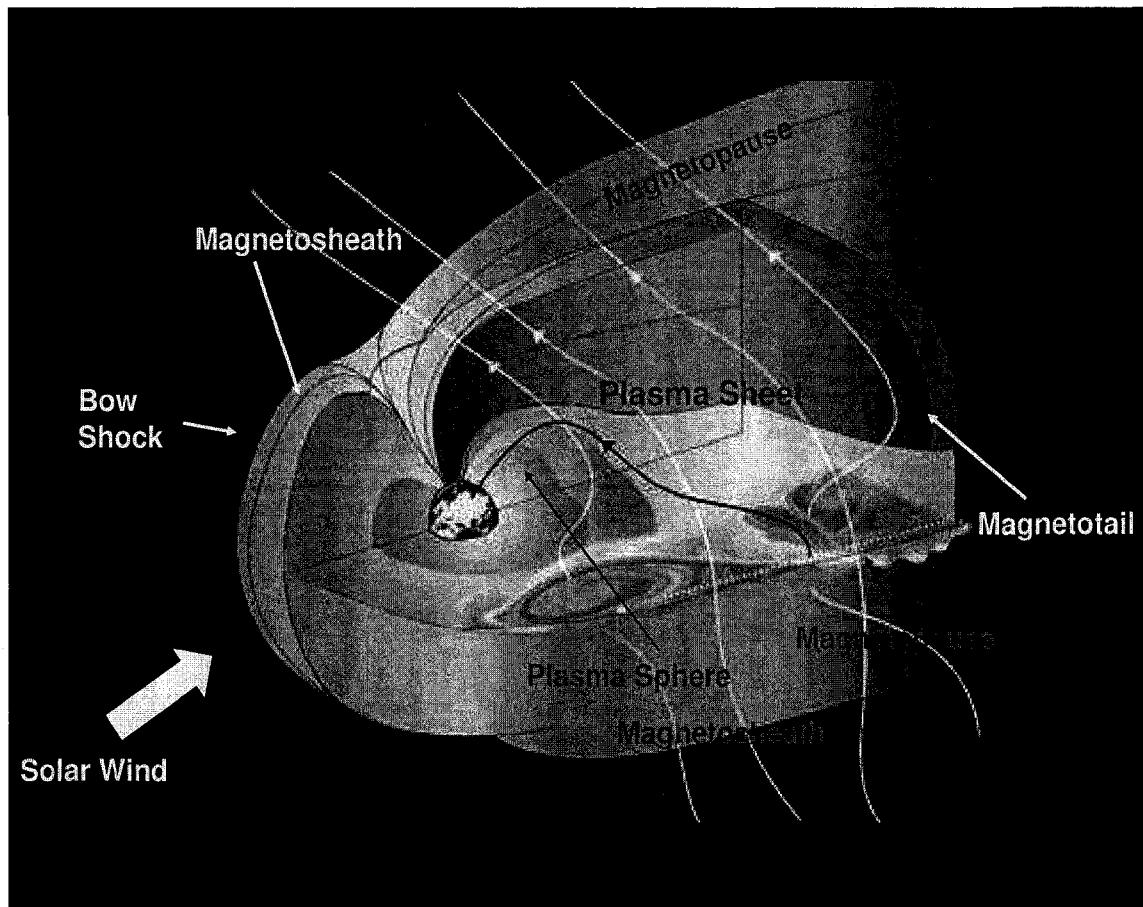
Figure 5.1: Three dimensional cutway view of the Earth's magnetosphere interacting with the solar wind. (From European Space Exploration, http://www.esa.int).

of 6 nT at the Earth. The solar wind speeds up as it moves away from the Sun, typically reaching to 400 km/s at the Earth. This is much higher than local sound speed ($C_s = \sqrt{\Gamma p/\rho} \sim 50$ km/s) and Alfvén speed ($V_A = \sqrt{B^2/(\mu_0\rho)} \sim 40$ km/s). Here B is the magnetic field strength, p is the plasma pressure, ρ is the plasma density, Γ is the adiabatic index and $\mu_0 = 4\pi \times 10^{-7}$ N/A^2 is the permeability of free space. Therefore, a shock wave called the bow shock is formed in front of the Earth that slows and heats up solar wind particles as they approach the Earth. Behind the bow shock is the region of shocked solar wind known as the magnetosheath. Figure 5.1 is a simple schematic of the interaction of the Earth's magnetosphere with the solar wind. The magnetosphere, the region of space encompassing the Earth's magnetic field and it is bounded by the magnetopause, is divided to several regions based on the plasma and the magnetic field characteristics. The plasma sheet is usually contained particles of ionospheric or solar wind origin. Depending upon their energies, these particles may precipitate into the high-latitude ionosphere creating auroral. The magnetotail region is adjacent to the plasma sheet where the plasma density is very much reduced. The plasmasphere corotates with the Earth and extends to the plasmapause at approximately 5 Earth's radii (R_E).

At the Earth's magnetosphere, the transported energy by the solar wind can excite magnetohydrodynamic (MHD) waves through the magnetosphere's plasma. MHD theory deals with a compressible, conducting fluid immersed in a magnetic field. In the general case, with the wave propagation in an arbitrary direction with respect to external magnetic field **B**, three MHD wave modes are found: Alfvén wave, slow MHD wave, and fast MHD wave.

The Alfvén wave is a transverse wave that propagates parallel to the magnetic field direction. The maximum phase velocity of the Alfvén wave is given by $V_A = \sqrt{B^2/(\mu_0\rho)}$. The slow compressional MHD wave is a longitudinal wave and propagates parallel to B. Its maximum phase velocity is the adiabatic sound velocity, $C_s = \sqrt{\Gamma p/\rho}$. The fast compressional MHD wave is a longitudinal wave. This wave propagates perpendicular to B with higher phase velocity, $V = \sqrt{V_A^2 + C_s^2}$, than the Alfvén wave and the slow compressional MHD wave.

Field line resonances (FLRs) are the result of an energy transportation involving the propagation of fast compressional MHD waves and their coupling to the local resonant shear Alfvén waves. Physically, the field line resonance mechanism is similar to a propagating transverse wave along a fixed string. In this case, the string is a geomagnetic field line with foot points fixed at each ionosphere. The transverse

wave along the magnetic field lines is produced when the magnetic field perturbations are perpendicular to the background magnetic field. This mode of magnetic waves is called the shear Alfvén wave.

The theory of FLRs was developed by Chen & Hasegawa (1974) and Southwood (1974) who proposed that surface waves on the magnetopause generate compressional waves in the magnetosphere which couple to the standing shear Alfvén FLRs. Observations of FLRs in HF coherent scatter radar data (Ruohoniemi et al., 1991; Walker et al., 1992; Samson et al., 1992) and ground-based magnetometer data (Ziesolleck and McDiarmid, 1994; Samson et al., 1991) have shown that FLRs occur repeatedly at the same frequencies during different magnetospheric conditions. The most commonly observed frequencies were 1.3, 1.9, 2.6, and 3.3 mHz with uncertainties less than 10%.

FLRs have a number of distinguishing properties. There is an inverse relationship between frequency and latitude, i.e. lower frequency FLRs happens at higher latitudes. This behavior can be understood, knowing that the Alfvén wave frequency decreases with radial distance. Since larger distances map to higher latitudes, we can see the inverse relationship between frequency and latitude. For further discussion of the field line resonances see for instance Stix (1992), and for the example of the numerical simulation see Rickard & Wright (1994).

5.2 Observation of the discrete field line resonances

5.2.1 The Super Dual Auroral Radar Network

Recent observational and theoretical investigations in the space plasma physics show that FLRs and observed aurora dynamics in the Eart's magnetosphere are unique phenomena (Samson et al., 1996; Lotko et al., 1998; Rankin et al., 1999; Milan et al., 2001; Samson et al., 2003).

In order to increase the general understanding of the discrete FLR phenomenon, Fenrich et al. (1995) performed observational studies of field line resonance events using the Super Dual Auroral Radar Network (SuperDARN) of high frequency (HF) radars. HF radars produce radio signals that span the band 3-30 MHz (corresponding with wavelengths between 10 meters and 100 meters).

The SuperDARN network currently contains 9 radars in the northern hemisphere and 6 in the southern hemisphere where 4 of them are located in Canada, the

Prince George and Saskatoon radars operated by the University of Saskatchewan and Kapuskasing and Goose Bay radars operated by the Johns Hopkins University. The fields-of-view of these radars in the northern hemisphere are shown in Figure 5.2. The letters T, P, K, and G represent the location of the Saskatoon, Prince George, Kapuskasing, and Goose Bay, respectively. Each of the radars has two sets of antennas operating in the 8-20 MHz band. The primary array consists of sixteen antennas, and the secondary, interferometer array, consists of four towers. The radar transmits a short sequence of pulses in the HF band and samples the returning echoes. At each time, a single beam is formed and advanced through 16 successive azimuths with an angular separation of 3.24 degrees yielding a total azimuthal field of view of about 52 degrees. The beams are numbered 0 to 15, from the westernmost to easternmost beam. A 3.75 s integration time at each beam azimuth results a 60 s complete scanning for all 16-beam. At each beam azimuth, over a period of 100 ms the superDARN radars transmit a 5 to 7 pulse sequences. The return backscatter from the pulse sequence is sampled and processed to determine the backscattered power, the mean Doppler velocity and the width of the Doppler power spectrum for each range gate. Each beam contains a maximum of 75 range gates that are spaced 45 km apart.

The doppler velocities measured by these radars are presenting the bulk motion of the ionospheric plasma. It is obvious that the single beam measurements can only have information about the line-of-sight Doppler velocity, the component of plasma velocity that is along the beam direction. This restriction, however, can be overcome by considering the overlap measurements between SuperDARN radar pairs that provide the Doppler velocities in different directions. Therefore, the total velocity vectors of the plasma flow in the plane perpendicular to the magnetic field lines can be determined.

5.2.2 The observed Doppler velocity data

The SuperDARN radar system provides an excellent tool for observing and studying field line resonances. In the measured line-of-sight Doppler velocities of the plasma flow, some ultra-low frequency oscillations are observable. These oscillations are associated with field line resonances occurring in the plasma flow.

The data we use here is the line-of-sight Doppler velocity taken by the Prince George radar for a 3-hour time interval on Nov. 20-21, 2003 from 22:00 to 01:00 UT.
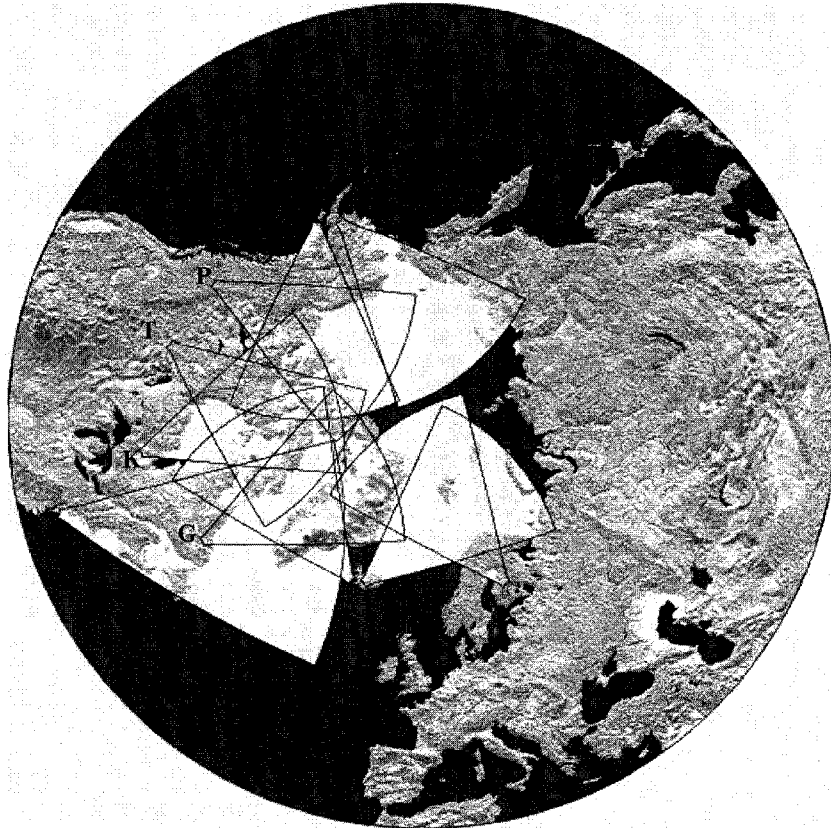
Figure 5.2: Fields-of-view of the Super Dual Auroral Radar Network (Super-DARN) in the northern hemisphere. Four radars are located in Canada at Prince George (P), Saskatoon (T), Kapuskasing (K) and Goose Bay (B). (Taken from http://superdarn.jhuapl.edu/)

The data set contains 16 beams from beam 0 to 15 and each beam has data from 8 range gates, gate 4 to 11. This time and region was chosen as it was previously determined to exhibit field line resonance characteristics. The time resolution of data is 60 s with 180 time points in total. As examples, Figure 5.3 shows beams 7 and 8 that each contains eight channels of data corresponding to range gates 4 to 11, and Figure 5.5 shows gates 6 and 7 that each includes sixteen channels of data corresponding to the sixteen beams at range 0 to 15. In these figures the data are shown with no correction.

In order to make use of the data, we first detrended it by subtracting a 30 minute running average, i.e. at each time point in a beam- range, the data is averaged for 30 minutes centered around that point and then subtracted from the original data value at that point. Every beam and range gate of the data is then despiked by removing any points that were greater than 1.5 times the standard deviation of all points in the 3 hour interval at that particular beam and range gate. The latter provides better result in despiking than a fixed cutoff despiking since different beams and range gates have different wave amplitudes and would require a different cutoff. Finally the data are scaled to reduce the possibility of overflows during filtering. The results are presented in Figures 5.4 and 5.6.

5.3 Temporal and spatial analysis of the discrete field line resonances

In order to extract discrete field line resonance characteristics from the data set, we need to employ a temporal and spatial spectral analysis on the data. The spatial and temporal spectral analysis would help us to single out signals associated with the time series and hence estimate their frequencies and wavenumbers. In general, the spectral analysis (both spatial and temporal) is very dependent on source and detector characteristics. For the temporal analysis of time series, the discrete Fourier transform (DFT) would provide signals' frequency with acceptable resolution. For a the spatial analysis of multichannel time series observed with an array of detectors, however, DFT alone may not be a good choice.

As we discussed in Chap. 4, array signal processing (or multichannel time series analysis) has been used for several decades in radar, sonar and seismic data analysis. A set of detectors that are spatially distributed at specific locations is usually

considered as an array. These detectors receive and record incoming signals from sources in their field of view. Several techniques are proposed to analyze multichannel time series such as Capon's minimum variance and linear prediction method or eigenvector-based techniques such as multiple signal classification (MUSIC). See Pillai (1989) for detail and review about these methods.

In this section we first compute the temporal spectra using the DFT for the Doppler velocity data observed by SuperDARN radars. Then we spatially analyze our data with both DFT and the eigenvector-based method MUSIC .

5.3.1 Temporal analysis using DFT

In this section, following Chatfield (1991), we discuss the temporal power spectrum of the Doppler velocity data given in Figures 5.4 and 5.6.

The spectral density function of a time series $\mathbf{X} = [X(t_0), X(t_1) \ldots , X(t_{N-1})]^T$ with length N is defined as

$$f(\omega) = \frac{1}{\pi} \sum_{\tau=-\infty}^{\infty} \gamma(\tau) e^{-i\omega\tau}, \tag{5.1}$$

where ω is the angular frequency in the range $(0, \pi)$ and τ is the lag value. The lagged autocovariance function $\gamma(\tau)$ of the data $\mathbf{X}$ is defined as

$$\gamma(\tau) = E\{[X(t) - \mu][X(t + \tau) - \mu]^*\}, \tag{5.2}$$

Here $E\{\ \}$ means average over time and $\mu = E\{\mathbf{X}\}$ (Chatfield, 1991). More practically, the autocovariance coefficient $\gamma(\tau)$ can be estimated from

$$\widetilde{\gamma}(\tau) = \frac{1}{N} \sum_{t=0}^{N-\tau-1} [X(t) - \mu][(X(t + \tau) - \mu]^*. \tag{5.3}$$

It is shown that the above estimator is asymptotically unbiased (Priestley, 1981)

$$\lim_{N \to \infty} E\{\widetilde{\gamma}(\tau)\} = \gamma(\tau). \tag{5.4}$$
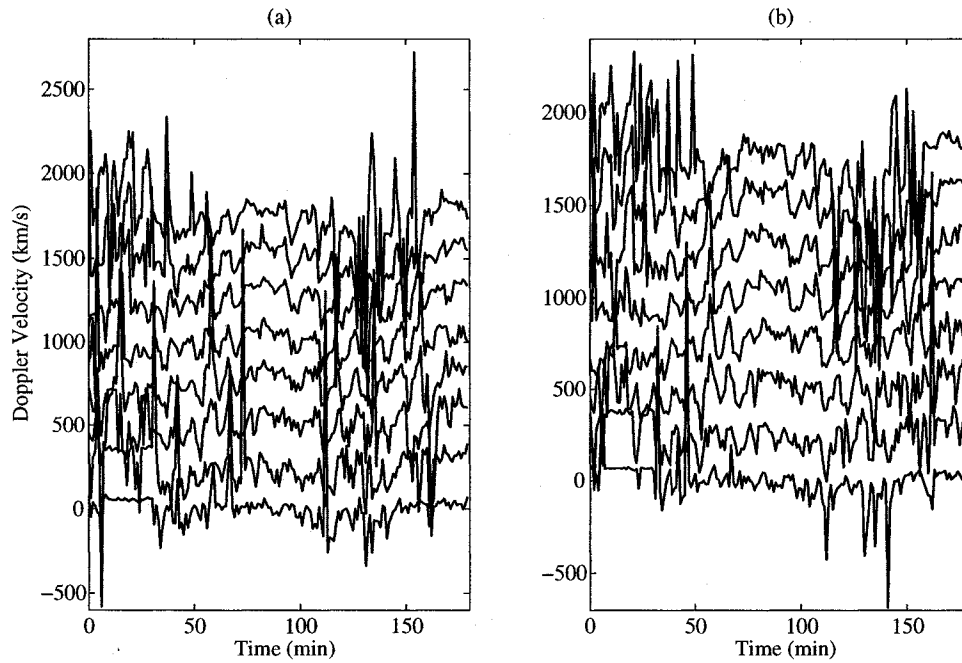
Figure 5.3: Original data. (a) Beam 7 and (b) beam 8 from Prince George radar Doppler velocity data for a 3 hour time interval on Nov. 20-21, 2003 from 22:00 to 01:00 UT. The whole data contains 16 beams from beam 0 to 15 with each beam including data from 8 range gates from gate 4 to 11. The gates 4 to 11 are ordered from bottom to top. The time resolution of data is 60 s with 180 time points in total.
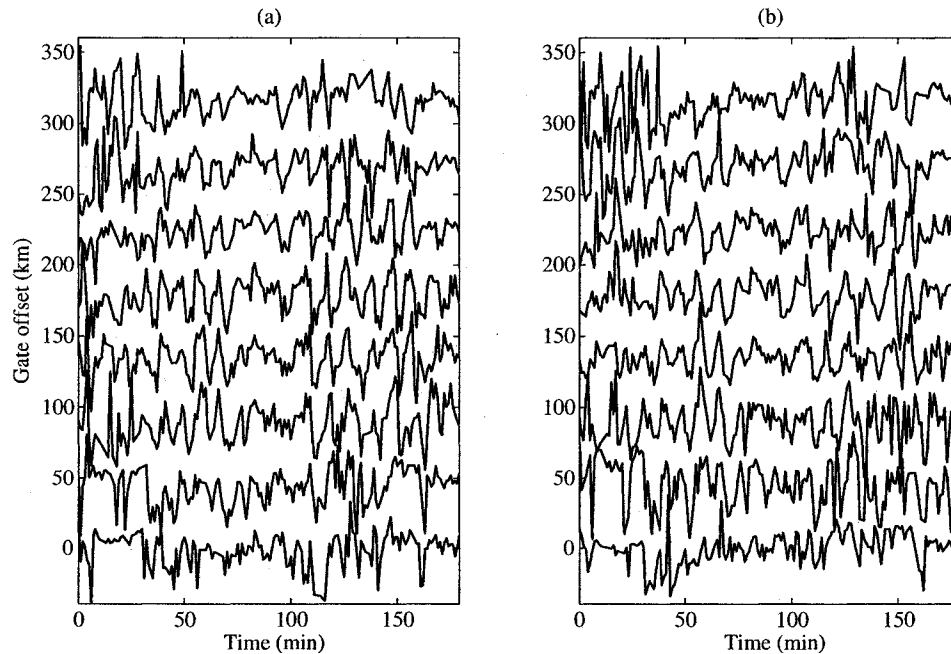
Figure 5.4: (a) Beam 7 and (b) beam 8 after detrending, despiking and scaling. The amplitude in each gate is normalized to its own maximum and scaled with 50% excursion.
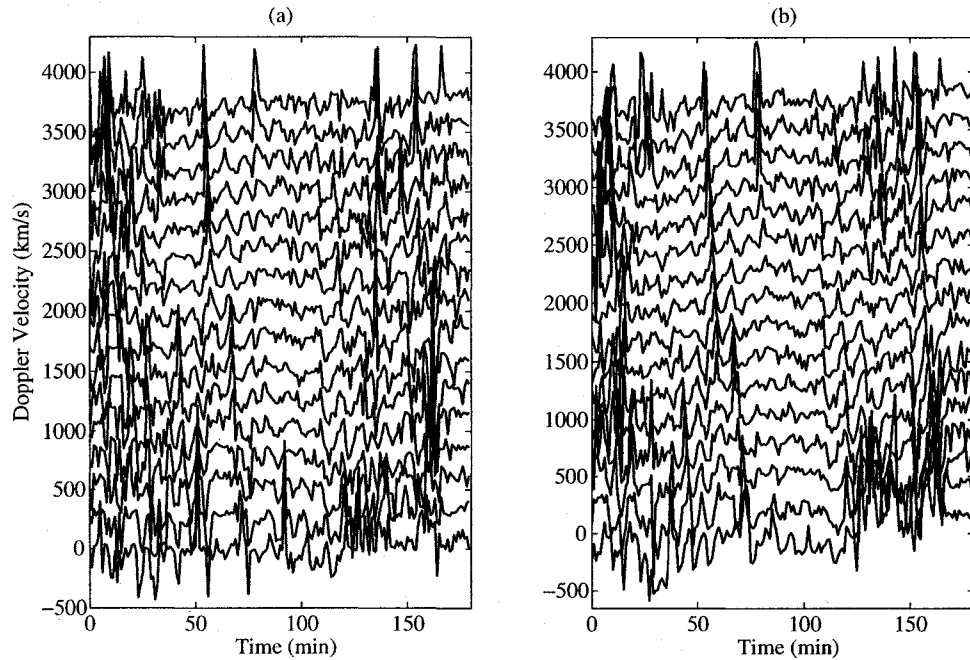
Figure 5.5: Original data. (a) Gate 6 and (b) gate 7 from Prince George radar Doppler velocity data. The whole dataset contains 8 gates from gate 4 to 11 and each one includes data for 16 beams from 0 to 15. The beams 0 to 15 are ordered from bottom to top.
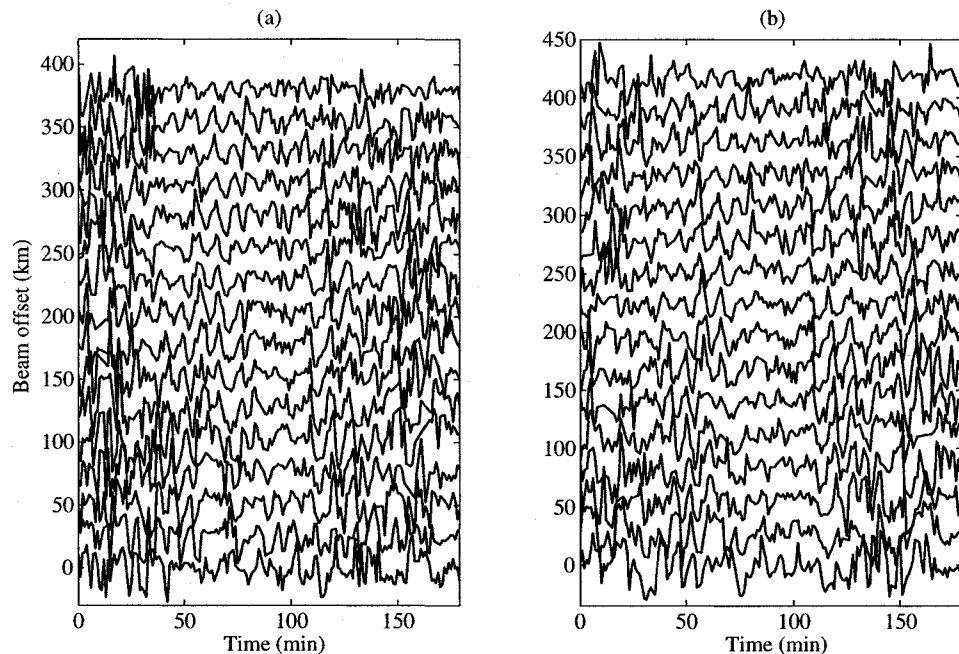
Figure 5.6: (a) Gate 6 and (b) gate 7 after detrending, despiking and scaling. The amplitude in each gate is normalized to its own maximum and scaled with 30% excursion.

Equation (5.1) shows that the power spectrum function is the Fourier transform of the lagged autocovariance function $\gamma(\tau)$. Since $\gamma(\tau)$ is an even function, then equation (5.1) can be written as

$$f(\omega) = \frac{1}{\pi} \left[\gamma(0) + 2 \sum_{\tau=1}^{\infty} \gamma(\tau) \cos \omega\tau \right].$$
(5.5)

Using the autocovariance estimate (5.3) the power spectral density function can be estimated

$$\widetilde{f}(\omega) = \frac{1}{\pi} \left[\widetilde{\gamma}(0) + 2 \sum_{\tau=1}^{N-1} \widetilde{\gamma}(\tau) \cos \omega\tau \right].$$
(5.6)

The estimated power spectral density $\widetilde{f}(\omega)$ is also called the periodogram, $I(\omega)$. Similar to the autocovariance estimator, equation (5.3), the estimated power spectrum or periodogram is also asymptotically unbiased

$$\lim_{N \to \infty} E\{I(\omega)\} = f(\omega).$$
(5.7)

However, since the variance of $I(\omega)$ does not decreases as N increases, the $I(\omega)$ is not a consistent estimator for $f(\omega)$. See Chatfield (1991) for detail.

Several smoothing procedures are proposed to provide a consistent estimate of the power spectral density function from the periodogram (5.6). The general idea in these smoothing procedures is to give less weight to the autocovariance coefficient $\widetilde{\gamma}(\tau)$ as τ increases. Therefore, instead of the periodogram (5.6), one may consider a weighted periodogram such as

$$\widetilde{f}(\omega) = \frac{1}{\pi} \left[\xi_0 \widetilde{\gamma}(0) + 2 \sum_{\tau=1}^{\tau_{\max}} \xi_\tau \widetilde{\gamma}(\tau) \cos \omega\tau \right],$$
(5.8)

where $\{\xi_\tau\}$ are a set of weights called the lag window and $\tau_{\max}(< N)$ is called the truncation point. Comparing equations (5.6) and (5.8) reveals that the autocovariance coefficients $\gamma(\tau)$ for $\tau > \tau_{\max}$ are no longer used.

It is clear that the above smoothing procedure highly depends upon the choice of the lag window and the truncation point. There are several lag windows proposed for different data structures. The most popular lag windows is known as the Tukey window

$$\xi_\tau = \frac{1}{2} \left(1 + \cos \frac{\pi\tau}{\tau_{\max}} \right), \quad \tau = 0, 1, \ldots, \tau_{\max}.$$
(5.9)

This window is also known as the Tukey-Hanning or Blackman-Tukey window (Chatfield, 1991).

The value for the maximum lag, τ_{max}, should be optimized to get a smooth result with small variance and good resolution. The bigger τ_{max} the higher the resolution and the larger the variance. $\tau_{max} \approx N$ provides high resolution results but with large variance and therefore are not trustable. In contrast, if τ_{max} is too small, the important features of the power spectral function $f(\omega)$ may be smoothed out. In practice, $\tau_{max} \approx 2\sqrt{N}$ gives a smooth result with small variance and more or less a good resolution. This choice also well behaves asymptotically that as $N \to \infty$, so does $\tau_{max} \to \infty$, but such that $\tau_{max}/N \to 0$. The latter ensures the variance of the smoothed periodogram decreases as N increases.

Julius Von Hann introduced an alternative smoothing procedure that turned out to be equivalent to the Tukey window. He first calculates the truncated unweighted periodogram from equation (5.6) as

$$\widetilde{f}_1(\omega) = \frac{1}{\pi}\left[\widetilde{\gamma}(0) + 2\sum_{\tau=1}^{\tau_{max}}\widetilde{\gamma}(\tau)\cos\omega\tau\right],\tag{5.10}$$

and then smooths it using the weights $(\frac{1}{4}, \frac{1}{2}, \frac{1}{4})$ as

$$\widetilde{f}(\omega_j) = \frac{1}{4}\widetilde{f}_1(\omega_j - \pi/\tau_{max}) + \frac{1}{2}\widetilde{f}_1(\omega_j) + \frac{1}{4}\widetilde{f}_1(\omega_j + \pi/\tau_{max}),\tag{5.11}$$

where $\omega_j = \pi j/\tau_{max}$ for $j = 1, 2, \ldots, \tau_{max} - 1$. Equation (5.11) is known as Hanning smoothing method or Hanning window. Substituting equation (5.10) into (5.11), one can easily show that the the Hanning window is equivalent with Tukey window. Although both procedures produce the same results, the Hanning window is slightly more efficient for computational manners.

Another well known technique that is very similar to Hanning method is so called Hamming, named after R. W. Hamming. The Hamming method is nearly identical to the Hanning technique except that the weights that are $(0.23, 0.54, 0.23)$. In this chapter we calculate the smoothed power spectral function using the Hamming technique.

Figure 5.7 represents the temporal periodograms of Doppler velocity for the beams 7 and 8. Gates 4 to 11 are arranged from bottom to top. Each channel is scaled by its maximum amplitude value times half of mean offset. Two dominant frequencies with relatively large amplitudes can be seen at ~ 0.8 mHz and $\sim 1.6 - 2$
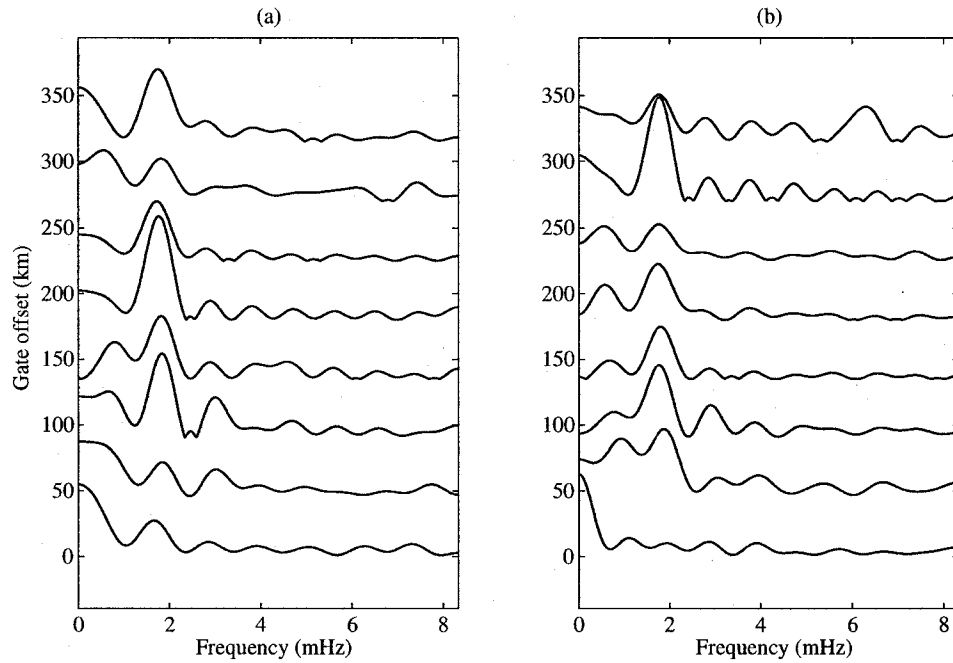
Figure 5.7: Smoothed power spectra of the (a) beam 7 and (b) beam 8 for gates 4 to 11 (from bottom to top). Each channel is scaled by its maximum amplitude value times half of mean offset.
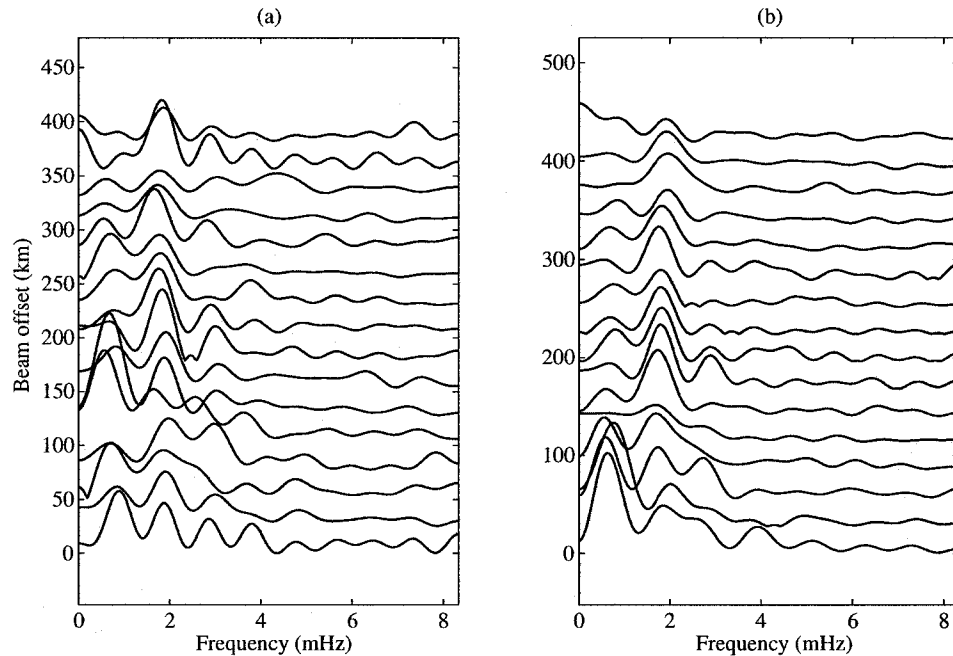
Figure 5.8: Smoothed power spectra of the (a) gate 6 and (b) gate 7 for beams 0 to 15 (from bottom to top). Each channel is scaled by its maximum amplitude value times half of mean offset.

mHz. Similarly, Figure 5.8 shows the smoothed Doppler velocity power spectrum for gates 6 and 7. Beams 0 to 15 are arranged bottom to top. Several dominant frequencies can be seen mainly about $\sim .8$ mHz, $\sim 1.6 - 2$ mHz and ~ 3 mHz.

The above frequencies can be associated to the observed FLRs in the Earth's magnetosphere (Walker et al., 1992).

5.3.2   Spatial analysis using DFT and MUSIC

A 2D FFT is also carried out on the data to locate the signal wavenumbers. As we discussed earlier, each beam is separated from the other by 3.24 degree in azimuthal direction while the range gates are all separated by 45 km. For our data set, there is fixed range from the origin of the coordinate system to gate zero that is 180 km. Therefore, the range to gate n from the origin is given by $180 + 45n$ km. As a result, each beam is separated from the other beam by a distance of

$$d(n) = (3.24\pi/180)(180 + 45n) \text{ km}, \tag{5.12}$$

where n is the gate number.

In Figures 5.9 to 5.12 we plot the 2D power spectrum of the beam 7, beam 8, gate 6 and gate 7, respectively. In each figure, panel (a) represents the original data, panel (b) shows the 2D periodogram (in dB) using DFT and panel (c) presents the power spectrum (in dB) estimated by MUSIC method. It is obvious that the MUSIC spectra provide higher resolution results than that of estimated by DFT method.

Tables 5.1 and 5.2 present signals' frequency (f), latitudinal and azimuthal wavenumber (k_x and k_y, respectively), latitudinal and azimuthal components of phase velocity (V_x and V_y, respectively) of the radar data for the first three power maxima. The phase velocity is defined as

$$V = \frac{\omega}{k}, \tag{5.13}$$

where $\omega = 2\pi f$ is the angular frequency and $k = 2\pi/\lambda$ is the wavenumber. Furthermore, scatter plots of the latitudinal and azimuthal wavenumbers versus frequency are plotted in Figure 5.13. It is clear that the frequency ranges from ~ 0.05 mHz to ~ 2 mHz. The latitudinal and azimuthal wavenumbers also vary between ~ -0.002 and ~ 0.004 km^{-1}. It should be noted that since the spatial scale of a FLR extends

Figure 5.9:   Smoothed f-k power spectra of the beam 7 for gates 4 to 11 (from bottom to top). (a) The observed Doppler velocity data after despiking and detrending. (b) 2D periodogram of the data using DFT. (c) Power spectrum of the data using MUSIC after spatial smoothing ($K = 6$). The wavenumber k_x represents the latitudinal wavenumber.

Figure 5.10:   Similar to Fig(5.9) but for the beam 8.

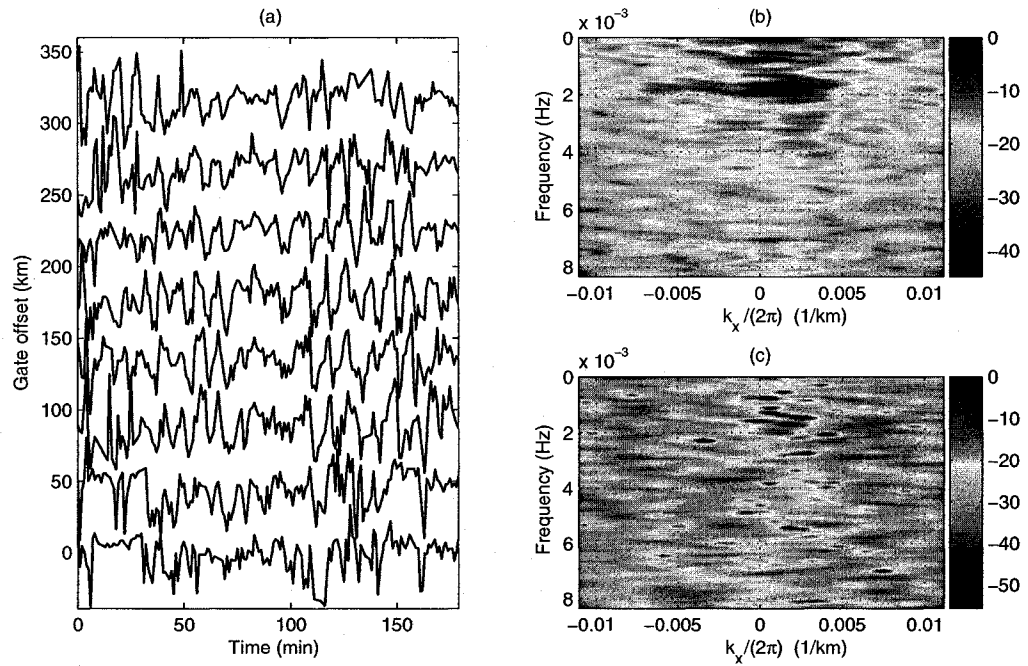Figure 5.11:   Smoothed f-k power spectra of the gate 6 for beams 0 to 15 (from bottom
to top). (a) The observed Doppler velocity data after despiking and detrending. (b) 2D
periodogram of the data using DFT. (c) Power spectrum of the data using MUSIC after
spatial smoothing ($K = 12$). The wavenumber k_y represents the azimuthal (East-West)
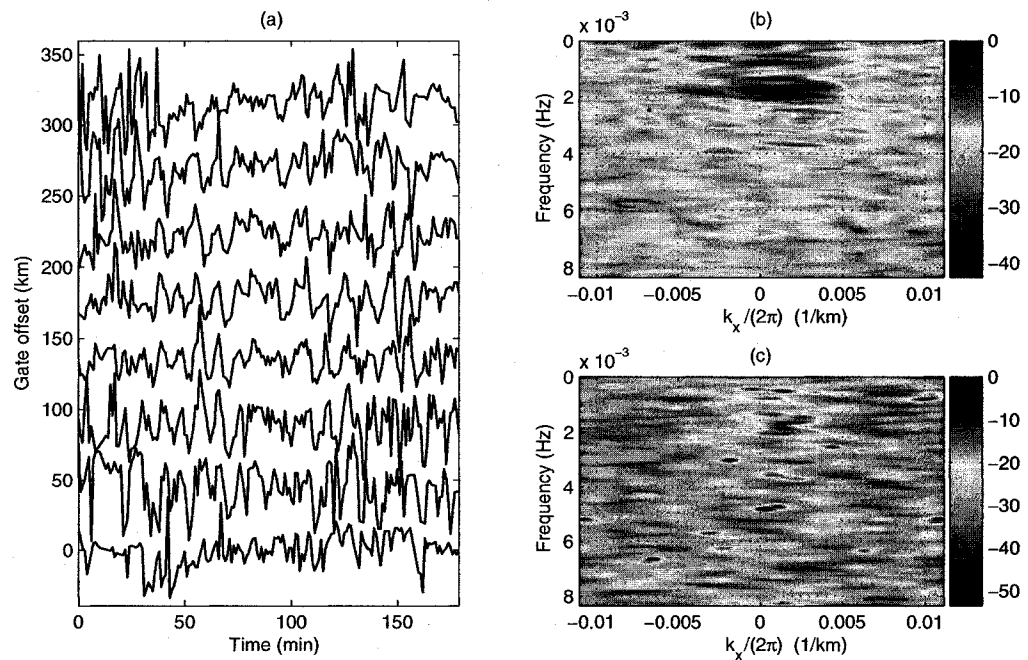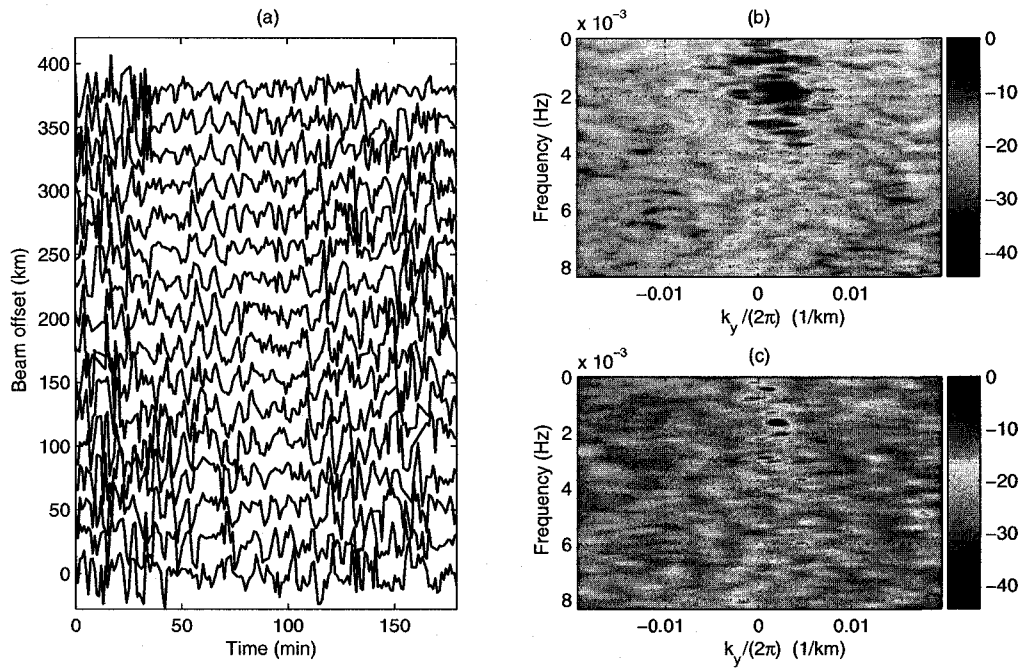wavenumber.
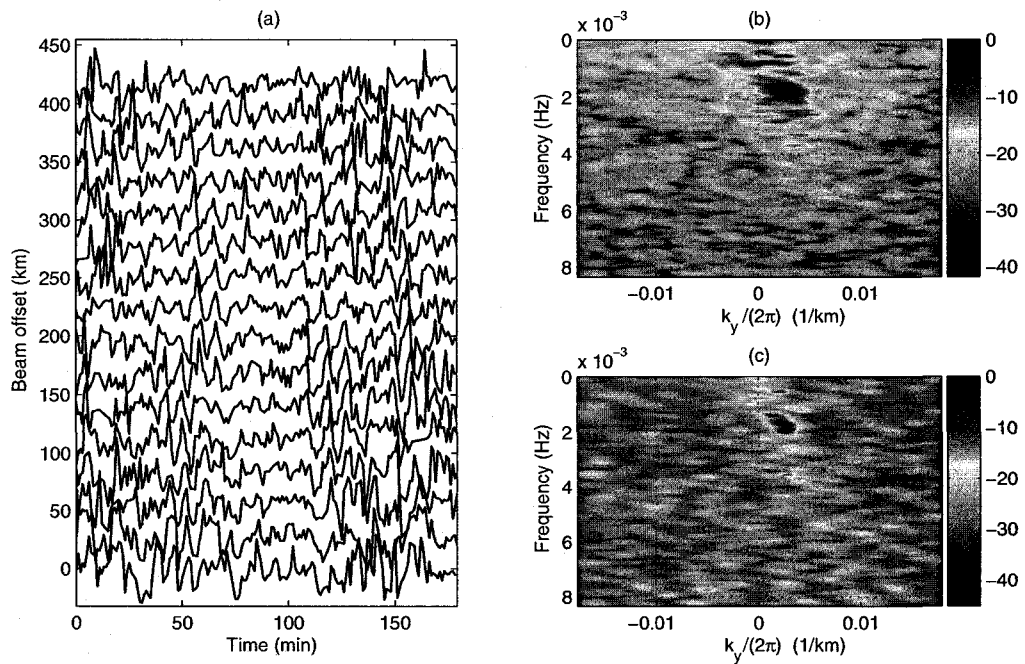
Figure 5.12:   Similar to Fig(5.11) but for the gate 7.

over a large portion of the field of view of a radar only clusters of points at specific frequencies in the scatter plots are significant in terms of being associated with a FLR. Single solitary points would not be associated with a FLR and may be due to noise or a transient wave.

As we mentioned $k_x/(2\pi)$ represents the inverse wavelength of the wave in the latitudinal direction. Based on theory of the coupling between outer magnetospheric compression waves to the FLRs (which is beyond the scope of this thesis), there is a 180 degree phase change with latitude across the resonance. Radar observations have shown the latitudinal width of the FLRs to vary from $\sim 100 - 400$ km which given the 180 degree phase change would correspond to one-half of a spatial wavelength (Fenrich et al., 1995). So latitudinal wavelengths of the FLRs should be $\sim 200 - 800$ km which correspond to $k_x/(2\pi)$ values of 1/wavelength $\simeq 0.001 - 0.005$ km^{-1} which is consistent with the listed values of $k_x/(2\pi)$ in Table 5.1. The $k_x/(2\pi)$ values < 0.001 km^{-1} indicate a small phase variation with latitude which may indicate wave modes that are not a FLR or may be due to a radar line of sight effect.

The sign of k_x is an indication of where the energy source driving the FLR is coming from. The positive k_x values indicate equatorward phase propagation of the wave which is consistent with an internal energy source provided by wave coupling to energetic particles in the inner magnetosphere. A negative k_x value indicates poleward phase propagation which is consistent with an external energy source provided by coupling to a compressional wave in the outer magnetosphere. In the event presented here, Table 5.1 and Figure 5.13(a), the k_x values are predominantly positive indicating a wave-particle coupling mechanism associated with the FLR. The small positive and negative $k_x/(2\pi)$ values for the points clustered around 0.8 mHz most likely indicate that the wave mode at this frequency is not a FLR.

The variable k_y represents the azimuthal or east-west spatial phase variation. FLRs are typically classified into high and low-m FLRs, where m is the azimuthal wavenumber and is the number of wavelengths that would fit around the circumference of the earth at that latitude. High-m FLRs typically of m values greater than ~ 15 and low-m FLRs typically have m values less than 15 because high-m modes couple to energetic protons in the magnetosphere and these energetic protons have a maximum azimuthal drift speed which determines a minimum m value FLR mode it can couple to. At 70 degrees latitude a simple calculation shows that an m value of 15 corresponds to an azimuthal wavelength of ~ 1000 km or a $k_y/(2\pi)$ value of 0.001 km^{-1}. As seen in Figure 5.13(b), in our event the $k_y/(2\pi)$ values for the peaks

clustered around the $1.7 - 2.1$ mHz typically range from $0.002 - 0.003$ km^{-1} which would correspond to an m value range from $\sim 30 - 45$. So these wave modes would be classified as high-m FLRs and associated with a wave-particle source.

The sign of k_y indicates whether the wave is propagating eastward (negative k_y) or westward (positive k_y). Since the event reported here is at dusk westward is sunward and thus the FLR wave modes seen here are propagating predominantly westward. This is again consistent with a wave-particle source as the most likely particles coupling to the wave are energetic sunward drifting protons in the near earth region of the magnetosphere. These protons drift clockwise around the earth (looking down from north) at speed of ~ 10 km/s due to whats called the gradient curvature drift but this is beyond the scope of this thesis. Again the peaks clustered around 0.8 mHz indicate both eastward and westward propagation which is not typical of an FLR mode.

The latitudinal and azimuthal components of the phase velocity are given in Tables 5.1 and 5.2 and are plotted as function of frequency in Figure 5.14. Figure 5.14(a) shows no obvious variation in latitudinal phase velocity with frequency with most of the points falling between $\sim 0.5 - 5$ km/s which is typical for FLRs. Figure 5.14(b) shows a large variation in azimuthal phase velocity at the low frequencies, which again is not consistent with a FLR wave mode, while the higher frequency modes cluster closely around ~ 1 km/s. Assuming a dipolar magnetic field an azimuthal phase speed of ~ 1 km/s in the ionosphere corresponds to an azimuthal phase speed of ~ 10 km/s in the equatorial plane of the magnetosphere. This phase speed is consistent with the drift speed of 30 keV protons which often populate the dusk side of the magnetosphere during enhanced period of activity as is the case in this event. These results again suggest that the $1.7 - 2.1$ mHz FLR modes are due to a wave-particle source mechanism.

5.4 Concluding Remarks

In this chapter, we study the spatial and temporal analysis of the Doppler velocity data observed by the Super Dual Auroral Radar Network. These radars that operate in the high frequency (HF) band monitor ionospheric plasma convection over the
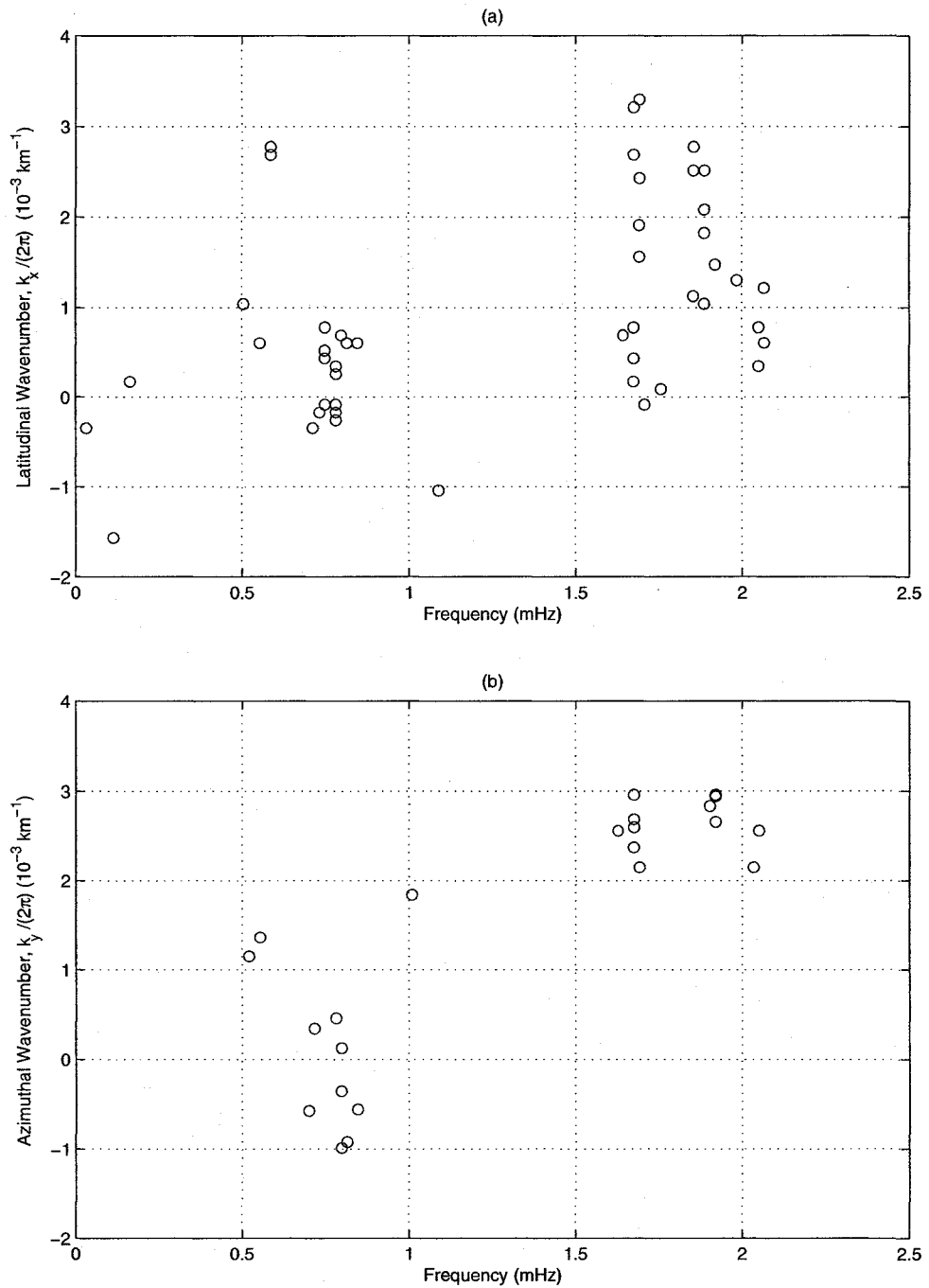
Figure 5.13:   (a) Latitudinal and (b) azimuthal wavenumber as function of frequency.
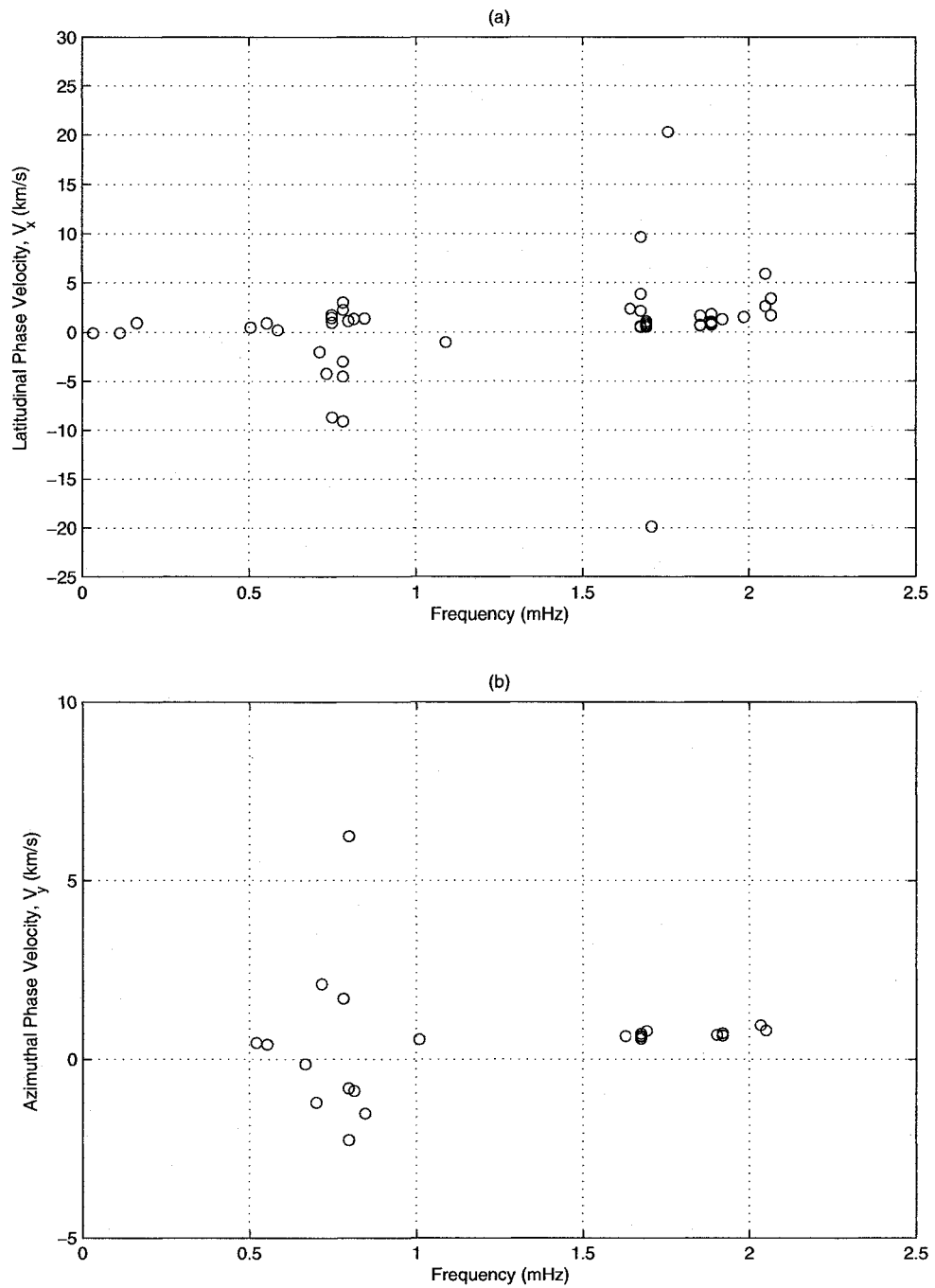
Figure 5.14: a) Latitudinal and (b) azimuthal phase velocity as function of frequency.

Table 5.1: Signals' frequency f (mHz), latitudinal wavenumber $k_x/(2\pi)$ (10^{-3} km^{-1}) and the latitudinal component of the phase velocity $V_x = \omega/k_x$ (km/s) of all beams for the first three maxima in power P (dB).

f	$k_x/(2\pi)$	V_x	P	f	$k_x/(2\pi)$	V_x	P
Beam 0				Beam 1			
0.0326	-0.347	-0.094	-0.294	1.7090	-0.086	-19.86	-0.0041
1.7580	0.0868	20.254	-1.618	0.5534	0.6076	0.9108	-1.06
0.7487	-0.086	-8.706	-1.865	0.1139	-1.562	-0.073	-1.275
Beam 2				Beam 3			
0.8464	0.6076	1.3930	0.0	0.1644	0.1736	0.9470	-0.0954
1.6760	0.4340	3.8617	-0.115	0.8138	0.6076	1.3394	-1.283
2.0500	0.3472	5.9043	-2.691	2.0670	0.6076	3.4019	-2.216
Beam 4				Beam 5			
1.6760	0.1736	9.6543	-0.137	1.6440	0.6944	2.3674	-0.0349
0.7813	-0.173	-4.499	-0.776	0.7813	0.3474	2.2490	-2.358
2.0670	0.6076	3.4019	-1.805	2.0501	0.7812	2.6254	-3.717
Beam 6				Beam 7			
1.6760	0.7812	2.1454	-0.0508	1.6930	1.5620	1.0838	0.0
0.7813	-0.260	-3.005	-1.180	1.8550	1.1280	1.6441	-0.725
2.0670	1.2150	1.7012	-1.971	0.7813	0.2604	3.0000	-2.348
Beam 8				Beam 9			
1.6930	1.9100	0.8863	-0.212	1.6930	2.4310	0.6947	0.0
1.8880	1.0420	0.4529	-1.238	1.9210	1.4760	1.3015	-1.428
0.7478	0.4340	1.7230	-2.190	0.5046	1.0420	0.4843	-3.30
Beam 10				Beam 11			
1.6760	2.6910	0.6228	0.0	1.8550	2.5170	0.7369	-0.177
0.7478	0.5208	1.4358	-1.591	1.6930	3.2990	0.5132	-0.403
1.9860	1.3020	1.5253	-3.126	0.7975	0.6944	1.1485	-1.284
Beam 12				Beam 13			
0.7324	-0.173	4.2335	-0.070	1.8880	2.5170	0.7501	-0.209
1.6760	3.2120	0.5218	-2.058	0.7116	-0.347	-2.049	-2.475
1.8550	2.7780	0.6678	-2.367	1.0900	-1.042	-1.046	-4.518
Beam 14				Beam 15			
1.8880	1.8230	1.0357	0.0	1.8880	2.0830	0.9064	-0.109
0.7487	0.7813	0.9583	-0.868	0.7813	-0.086	-9.085	-0.477
0.5859	2.7780	0.2108	-2.659	0.5859	2.6910	0.2177	-2.143

Table 5.2: Signals' frequency f (mHz), azimuthal wavenumber $k_y/(2\pi)$ $(10^{-3}\ \mathrm{km}^{-1})$ and azimuthal component of the phase velocity $V_y = \omega/k_y$ (km/s) of all gates for the first three maxima in power P (dB).

f	$k_y/(2\pi)$	V_y	P	f	$k_y/(2\pi)$	V_y	P
Gate 4				Gate 5			
0.6999	-0.576	-1.215	-0.214	2.0510	2.5580	0.8018	0.0
0.5208	1.1510	0.1440	-3.779	0.7161	0.3411	2.1873	-0.461
0.6673	-4.989	-0.134	-7.872	0.5534	1.3640	0.4057	-0.517
Gate 6				Gate 7			
1.6930	2.1490	0.7878	-0.058	1.6760	2.3720	0.7066	0.0
2.0350	2.1490	0.9470	-1.80	1.9210	2.6580	0.7227	-2.220
0.7813	0.4605	1.6966	-2.281	0.8464	-0.558	-1.439	-3.268
Gate 8				Gate 9			
1.6760	2.6860	0.6239	-0.015	1.6760	2.5980	0.6451	-0.031
1.9210	2.9420	0.6529	-2.264	0.7975	-0.354	-2.250	-1.157
0.7975	0.1279	6.2354	-7.610	1.9040	2.8340	0.6718	-2.350
Gate 10				Gate 11			
1.6760	2.9600	0.5662	-0.038	1.6280	2.5580	0.6364	-0.011
0.7975	-0.986	-0.808	-3.336	0.8138	-0.921	-0.884	-2.974
1.9210	2.9600	0.6489	-4.50	1.0090	1.8420	0.5478	-3.040

majority of the northern and southern polar regions. The data from one particular radar is used and the frequencies and wavenumbers of a field line resonance event are determined. Such spatial and temporal analysis can be used to understand the driving mechanism of the FLRs. Anti-sunward wave propagation (i.e. eastward at dusk or westward at dawn) are typical of solar wind driven mechanisms that generate compressional waves in the magnetosphere. These waves are believed to couple to the FLR with large azimuthal wavelengths. On the other hand sunward propagation generally means the FLR is coupled to energetic particles drifting around the Earth trapped within the Earth's magnetic field. For field line resonances to couple to energetic particle motions the azimuthal phase speed which is related to the azimuthal wave length must match the drift speed of the particles. Thus a measure of the azimuthal wave length and propagation direction can indicate if coupling to energetic particles is possible and what the energies of those particles might be. Typically only field line resonances with small azimuthal wavelengths can interact with drifting electrons and ions. Temporal analysis would also provide the coupling frequencies of the FLRs with source mechanisms.

For temporal analysis, a periodogram calculation is carried out. Several dominant frequencies are detected in data that are about $\sim .8$ mHz, $\sim 1.6 - 2$ mHz and

~ 3 mHz. See Figure 5.7 and (5.8) for details.

For spatial analysis two different routines are applied: (a) a 2D periodogram and (b) the multiple signal classification method. We found that the latter provides results with higher resolutions. The results are shown in Figures 5.9 to 5.12 for beams 7 and 8, and gate 6 and 7. Furthermore, using the above analysis, we determine the signals' frequency (f), latitudinal and azimuthal wavenumber (k_x and k_y, respectively), latitudinal and azimuthal components of phase velocity (V_x and V_y, respectively) for each beam and gate of the radar data selecting only the first three power maxima. These are listed in Tables 5.1 and 5.2. We found that the k_x values are predominantly positive within range of $\sim .001 - .005$ km^{-1} that is corresponding to the latitudinal wavelength of $\sim 200 - 800$ km. This is in good agreement with previous observations of FLRs (Fenrich et al., 1995). Values of the azimuthal wavenumber k_y, however, are mostly found greater than 0.001 km^{-1} that is consistent with the presence of high-m FLR events. Furthermore, the overall positive values of k_y reveals that the wave modes are propagating westward at speeds consistent with energetic proton drift speeds. This also confirms a wave-particle source as a major mechanism for the FRLs excitation.

In brief, based on the above results, one can say the $1.7 - 2.1$ mHz wave modes observed here are high-m FLR events associated with the wave-particle coupling mechanism. The ~ 0.8 mHz wave modes observed are likely not a FLR and may be the signatures of a propagating non-resonant wave mode.

Chapter 6

Conclusion

The current project aims to address two major subjects in data processing: noise attenuation/suppression and spatial-temporal analysis of a data structure.

In the first part of this thesis, chapters 2 and 3, noise attenuation using eigen-image decomposition method is discussed. The mathematical framework of singular value decomposition (SVD) for a general matrix is reviewed. Then its application on 2D and 3D synthetic data structure is studied. We show that for a poststack 2D seismic section containing zero dip events the noise compression can be done successfully by SVD decomposition. For prestack data, however, the results are fairly poor. This can be understood through the size of singular values of the data matrix, as for poststack data the magnitude of first few singular values are fairly large comparing to the rest while for prestack data their sizes decreases more or less monotically.

For 3D poststack data, the direct application of SVD would not able to enhance the signal-to-noise ratio (SNR) of the data. As a result, following Trickett (2003), the f-xy eigenimage method that is the SVD decomposition for constant-frequency slice rather than time-constant slice, is introduced. In this method we first transform the data from t-xy domain to f-xy domain. In the frequency domain, we showed that the data matrix can be written as sum of three matrices that multiplied to each other, similar to the SVD decomposition:

$$\mathbf{X}_\omega = \sum_{m=1}^{L} A_m \mathbf{u}_m \mathbf{v}_m^T. \tag{6.1}$$

See equation (3.25) for more detail. Such separability enabled us to reconstruct the

data in the *f-xy* domain with the first few eigenimages. Then, we transformed the reconstructed data to the *t-xy* domain. The application of *f-xy* on a 3D poststack synthetic data with nonzero dip events is studied. We found that the *f-xy* eigenimage method gives a superior result in noise compression for this type of data. The results are plotted in Figure 3.17 in the *t-xy* domain that shows a fairly good SNR enhancement. The flow chart for applying *f-xy* eigenimage decomposition is given in Figure 3.20.

In the second part of the current project, chapters 4 and 5, is devoted to the spatial-temporal analysis of given data structure. For temporal analysis the periodogram can be calculated by discrete Fourier transform (DFT) after a Hanning smoothing. For spatial analysis, however, the DFT power spectrum would not provide high resolution results. This is due to the small number of data points in spatial dimension. In this regard, an eigenstructure based method called multiple signal classification (MUSIC) is reviewed. Both synthetic and real data are analyzed with 2D f-k (DFT) and MUSIC methods. The real data are observed by the Super Dual Auroral Radar Network (SuperDARN) that is a network of high frequency (HF) radars and monitors ionospheric plasma convection over the majority of the northern and southern polar regions.

In case of temporal analysis, a periodogram calculation is carried out. Several dominant frequencies are detected in data that are about $\sim .8$ mHz, $\sim 1.6 - 2$ mHz and ~ 3 mHz. See Figure 5.7 and (5.8) for details.

In case of spatial analysis, we implemented two different routines on the radar data: (a) a 2D periodogram and (b) the multiple signal classification method (MUSIC). Figures 5.9 to 5.12 are shown the results for beams 7 and 8, and gate 6 and 7. It is clear that the MUSIC method provides results with higher resolutions.

Using the above graphs, we calculate signals' frequency (f), latitudinal and azimuthal wavenumber (k_x and k_y, respectively), latitudinal and azimuthal components of phase velocity (V_x and V_y, respectively) of the radar data for the first three power maxima. The results are listed in Tables 5.1 and 5.2 and plotted in Figures 5.13 and 5.14.

The results indicate a number of discrete frequency modes in the radar data set studied here including 0.8 mHz, 1.7 mHz, 1.9 mHz and 2.1 mHz. The lower frequency 0.8 mHz mode exhibits different k_x and k_y values from the other higher frequency modes in terms of both sign and magnitude and is inconsistent with what would be expected for a FLR mode. Thus the 0.8 mHz mode cannot be identified as a FLR.

The higher frequency modes all exhibit positive k_x values and large positive k_y values which are all consistent with a high-m FLR event associated with a wave-particle coupling mechanism. Furthermore, calculation of the azimuthal phase speeds of the high-m FLRs shows good correspondence with typical energetic particle drift speeds.

Overall the MUSIC method could be a powerful tool for studying the FLRs. We have demonstrated that the method can provide frequencies, k_x, k_y and phase velocity values for the different wave modes present in the data. The k values are significant because they indicate direction of propagation and potential source mechanisms. There is currently debate in the space science community about the source of these discrete FLRs, in particular what produces the specific discrete frequencies. The technique may help to answer the source question and whether the high-m modes are purely wave-particle driven or if they are seeded by an external source.

Only a handful of FLRs have been studied with the large SuperDARN data set primarily because it is very time consuming to search for and analyse the data for FLRs using current techniques. The MUSIC technique has the potential to be automated for analysis of a large portion of the SuperDARN data set and thus could provide valuable new information about magnetospheric waves and their role in energy coupling and dynamics in the magnetosphere.

Appendix A

Some definitions

A.1 The matrix rank

The rank of a matrix is the maximum number of linearly independent rows or columns of it, which leads the following properties.

- only the zero matrix has rank 0

- the rank of a $m \times n$ matrix $\mathbf{A}$ is at most $min(m, n)$

A.2 The mean vector and covariance matrix

Let $\mathbf{X}$ is a $(N \times M)$ data matrix with complex elements x_{ij} (row i and column j). The mean of the ith variable is

$$\bar{x}_i = \frac{1}{N} \sum_{r=1}^{N} x_{ri}, \tag{B.1}$$

and the variance of the ith variable, $\text{Var}(x_i)$, is

$$\sigma_i^2 = \frac{1}{N} \sum_{r=1}^{N} (x_{ri} - \bar{x}_i)(x_{ri} - \bar{x}_i)^*; \quad i = 1, 2, \cdots, M, \tag{B.2}$$

where $()^*$ denotes the complex conjugate. The covariance between the ith and j^{th} variables, $\text{Cov}(x_{ij})$, is

$$R_{ij} = \frac{1}{N} \sum_{r=1}^{N} (x_{ri} - \bar{x}_i)(x_{rj} - \bar{x}_j)^*. \tag{B.3}$$

The above relations may also written in matrix notation,

$$\bar{\mathbf{X}} = \frac{1}{N}\sum_{r=1}^{N}\mathbf{X}_r, \tag{B.4}$$

Therefore, equation (B.3) can be written as

$$\mathbf{R} = \frac{1}{N}\sum_{r=1}^{N}(\mathbf{X}_r - \bar{\mathbf{X}})(\mathbf{X}_r - \bar{\mathbf{X}})^{\dagger}, \tag{B.5}$$

where $()^{\dagger}$ is the complex conjugate and matrix transpose.

A.3 Probability

Probability, in mathematics, is a theory that describes the "chance" of a given event will occur. For discrete variables, probability is given by a number. For a continuous variable x, however, the probability is given by a function called probability density function (PDF), $p(x)$. In this case probability is calculated by the area under the PDF. The total area under a PDF is therefore unity

$$\int_{-\infty}^{\infty}p(x)dx = 1. \tag{B.6}$$

Further, the probability of x assuming a value between a and b is given by

$$Pr(a \le x \le b) = \int_{a}^{b}p(x)dx, \tag{B.7}$$

which is the area under the PDF between a and b.

The normal or Gaussian probability density is an example of a PDF for single variable x

$$p(x) \equiv N(x,\mu,\sigma) = \frac{1}{\sqrt{2\pi\sigma^2}}\exp\left(-\frac{(x-\mu)^2}{2\sigma^2}\right), \tag{B.8}$$

where μ and σ^2 are known as the mean and variance, and σ is called the standard deviation.

A.4 Expectation and moments

For a given PDF $p(x)$, the expected value of a function $f(x)$ is defined as

$$E\{f(x)\} \equiv \int_{-\infty}^{\infty} p(x)f(x)dx, \tag{B.9}$$

where $E\{\ \}$ refers to the expectation operator. The nth moment of a distribution is given by

$$E\{x^n\} = \int_{-\infty}^{\infty} x^n\, p(x)dx. \tag{B.10}$$

The mean is therefore the first moment of the distribution

$$E\{x\} = \int_{-\infty}^{\infty} x\, p(x)dx. \tag{B.11}$$

For N independent and identically distributed data points $y = [y_1, y_2, \cdots, y_N]$, the PDF will be

$$p(y) = \prod_{i=1}^{N} p(y_i), \tag{B.12}$$

where $p(y_i)$ is the Gaussian PDF of variable y_i

$$p(y_i) = \frac{1}{\sqrt{2\pi\sigma^2}} \exp\left(-\frac{(y_i - \mu)^2}{2\sigma^2}\right). \tag{B.13}$$

Equation (B.12) is also called the likelihood function of the data set. In statistics, μ and σ^2 are usually defined by maximizing equation (B.12), which leads to

$$\mu = \frac{1}{N} \sum_{i=1}^{N} y_i, \tag{B.14}$$

and

$$\sigma^2 = \frac{1}{N} \sum_{i=1}^{N} (y_i - \mu)^2. \tag{B.15}$$

Bibliography

Ahmed, N., and Rao, K. R., 1975, *Orthogonal Transforms for Digital Signal Processing.* Springer, Berlin.

Anderson, T. W., 1958, *An Introduction to Multivariate Statistical Analysis.* John Wiley, New York.

Anderson, T. W., 1975, in *Picture Processing and Digital Filtering.*, T. S. Huang, ed., Springer, Berlin.

Andrews, H. C., and Hunt, B. R., 1977, *Digital image restoration* Printice-Hall, Signal Processing Series.

Andrews, H. C., and Patterson, C. L., 1976, Singular value decompositions and digital image processing, IEEE Trans. Acous., Speech, and Sig. Proc., **24**, 26.

Bienvenu G., and Kopp, L., 1980, Adaptivity to background noise spatial coherence for high resolution passive methods, in Proc. IEEE ICASSP 80, Debver, CO, 307.

Bienvenu G., and Kopp, L., 1981, Source power estimation method associated with high resolution bearing estimation, in Proc. IEEE ICASSP 81, Atlanta, GA, 302.

Burg, J. P., 1975, Maximum entropy spectral estimation, Ph. D. dissertation, Standford Univ., Standford, CA.

Capon, J., 1969, High-resolution frequency-wavenumber spectrum analysis, Porc. IEEE, Vol. 57, 1408.

Chase, M. K., 1992, Random noise reduction by 3D spatial prediction filtering, 62nd Annual Intrernat. Mtg., Soc. Expl. Geophys. Expanded Abstracts, 1152.

Chatfield, C., 1991, *The Analysis of Time Series: An Introduction,* Chapman and Hall, New York.

Chen L., & Hasegawa A., 1974, A Theory of Long Period Magnetic Pulsations, 1. Steady State Excitation of Field Line Resonance, J. Geophys. Res., 79, 1024.

Done, W. J., Kirlin, R. L., and Maghadamjoo, A., 1991, Two-dimensional coherent noise suppression in seismic data using eigendecomposition, IEEE Trans. on Geosci. and Remote Sensing, **29**, 379.

Evans, J. E., Johnson, J. R., and Sun, D. F., 1982, Application of Advanced Signal Processing Techniques to Angle of Arrival Estimation in ATC Navigation and Surveillance Systems, Technical report, MIT Lincoln Laboratory.

Fenrich, F. R., Samson, J. C., Sofko, G., and Greenwald, R. A., 1995, ULF high- and low-m field line resonances observed with the Super Dual Auroral Radar Network, J. Geophys. Res., 100, 21535.

Fenrich, F. R., 1997, Field line resonance: observation and theory, Ph. D. Thesis, University of Alberta.

Frost, O., L., and Sullivan, T. M., 1979, High resolution two-dimensional spectral analysis, in Proc. ICASSP 79, Washington, DC., 673.

Freire, S. L. M, and Ulrych, T. J., 1988, Application of singular value decmposition to vertical seismic profiling, Geophysics, **53**, 778.

Freire, S. L. M., and Ulrych, T. J., 1990, An eigenimage appraoch to the attenuation of multiple reflections, Butsuri-Tanas, **43**, 1.

Friedlander, B., and Weiss, A., 1992, Direction Finding Using Spatial Smooth- ing with Interpolated Arrays. IEEE Trans. AES, 28:574.

Gerbrands, J. J., 1981, On the Relationships between SVD, KLT and PCA., Pattern Recognition, Vol. 14, 375.

Gnanadesikan, R., 1977, *Methods for Statistical Data Analysis of Multivariate Observations*. John Wiley, New York.

Goldstein, P., and Archleta, R., 1987, Array analysis of signals, Geophys. Res. Lett., 14, 13.

Good, I. J., 1963, Weighted covariance for estimating the direction of a Gaussian source, in Time Series Analyis, M. Rosenlatt, Ed., Wiley, New York

Hahn, W. R., and Tretter, S. A., 1973, Optimum processing for delay vector estimation in passive signal array, IEEE Trans. Inform. Theory, Vol. IT-19, No. 5, 608.

Hasegawa A., 1976, Particle acceleration by MHD surface wave and formation of aurora, J. Geophys. Res., 81, 5083.

Hemon, C. H., and Mace, D., 1978, Essai D'une application de la transformation de Karhunen-Loéve au traitement sismique, Geophyscal Prospecting, **26**, 600.

Huang, D. C., and Narendra, P. M., 1975, Image reconstruction by singular value decomposition, Applied Optics, **14**, 2213.

Iwata, T., Goto, Y., and Susaki, H., 2001, Application of the multiple signal classification (MUSIC) method for one-pulse burst-echo Doppler sonar data, Meas. Sci. Technol., 12, 2178.

Jackson, L. B., and Chien, C. H., Frequency and bearing estimation by two-dimesional linear prediction, in Proc. IEEE ICASSP 79, Washington, DC., 665.

Jackson, G. M, Mason, I. M., and Greenhalgh, S. A., 1991, Principal component transformations of triaxial recordings by singular value decomposition, Geophysics, **56**, 528.

Jain, A. K., and Raganath, S., 1978, Two-dimensional spectral estimation, in Proc. RADC Spectrum Est. Workshop, Rome, NY, 151.

Johnson, D. H., and Degraff, S. R., 1982, Improving the resolution of the bearing in passive sonar arrays by eigenvalue analysis, IEEE Trans. Acoust., Speech, Signal Processing, Vol. ASSP-29, 401.

Jones, I. F., and Levy, S., 1987, Signal-to-noise ratio enhancement in multichannel seismic data via the Karhunen-Love transform, Geophys. Prosp, **35**, 12.

Krim, H., and Viberg, M., 1996, Two decades of array signal processing research: the parametric approach, IEEE Signal Processing Magazine, Vol. 13, 67.

Krim, H., and Proakis, J. G., 1994, Smoothed Eigenspace-Based Paramerter Estimation, Automatica, Special Issue on Statistical Signal Procssing and Control.

Kumaresan, R., and Tufts, D. W., 1981, A two-dimensional technique for frequency-wavenumber estimation, Proc. IEEE, Vol. 69, 1515.

Kumaresan, R., and Tufts, D. W., 1983, Estimation of arrival of mutiple plane waves, IEEE Trans. Aerosp. Electron. Syst., Vol. AES-19, 134.

Levy, S., Jones, I. F., Ulrych, T. J., and Oldenburg, D. W., 1983, Application of common signal analysis in exploration seismology, 53rd Ann. Internat. Mtg., Soc. Expl., Geophys., Expanded Abstracts, 325.

Lanczos, C., 1961, *Linear Differential Operators*, D. Van Nostrand Co.

Lim, J. S., and Malik, N. L., 1981, A new algorithm for two-dimensional maximum entropy power spectrum estimation, IEEE Trans. Acoust., Speech, Signal Processing, Vol. ASSP-29, 401.

Lotko, W., Streltsov, A. V., and Carlson, C. W., 1998, Discrete auroral arc, electrostatic shock and suprathermal electrons powered by dispersive, anomalously resistive field line resonance, Geophys. Res. Lett., 25(24), 4449.

McClellan, J. H., 1982, Multidimensional spectral estimation, Proc. IEEE, Vol. 70, 1029.

Milan, S. E., Sato, N., Ejiri, S., and Moen, J., 2001, Auroral forms and the field-aligned current structure associated with field line resonances, J. Geophys. Res., 106(A11), 25825.

Mossop, G., and Shetsen, S., 1994, Geological Atlas of the Western Canada Sedimentary Basin, Online Version, Published jointly by the Canadian Society of Petroleum Geologists and the Alberta Research Council, in sponsorship association with the Alberta Department of Energy and the Geological Survey of Canada.

Ozdemir, A., Ozbek, A., Ferber, R., and Zerouk, K., 1999, $F - xy$ projection filtering using helical transformation, 69nd Annual Intrernat. Mtg., Soc. Expl. Geophys. Expanded Abstracts, 1231.

Pillai, S. U., 1989, *Array Signal Processing*, Springer-Verlag, New York. 13455.

Pisarenko, V., F., 1972, On the estimation of spectra by means of non-linear functions of the covariance matrix, Geophys. J. Roy. Astron. Soc., Vol. 28, 511.

Priestley, M. B., 1981, *Spectral Analysis and Time Series*, Academic Press, New York.

Rankin, R., Samson, J. C., and Tikhonchuk, V. T., 1999, Discrete auroral arcs and nonlinear dispersive field line resonances, Geophys. Res. Lett., 26(6), 663.

Reddi, S. S., 1979, Multiple source location-A digital approach, IEEE Trans. Aerosp. Electron. Syst., Vol. AES-15, 95.

Rickard G. J., & Wright A. N., 1994, Alfven resonance excitation and fast wave propagation in magnetospheric waveguides, J. Geophys. Res., 99, 13455.

Roucos, S., and Childers, D. G., 1980, A two-dimensional maximum entropy spectral estimator, IEEE Trans. Infor. Theory, Vol. IT-26, 554.

Ruohoniemi, J. M., Greenwald, R. A., Baker, K. B., and Samson, J. C., 1991, HF radar observations of Pc 5 field line resonances in the midnight/early morning MLT sector, J. Geophys. Res., vol. 96, 15697.

Samson, J. C., Greenwald, R. A., Ruohoniemi, J. M., Hughes, T. J., and Wallis, D. D., 1991, Magnetometer and radar observations of magnetohydrodynamic cavity modes in the Earth's magnetosphere, Canadian Journal of Physics, vol. 69, 929.

Samson, J. C., Harrold, B. G., Ruohoniemi, J. M., Greenwald, R. A., and Walker, A. D. M., 1992, Field line resonances associated with MHD waveguides in the magnetosphere, Geophys. Res. Letters, vol. 19, 441.

Samson, J. C., Cogger L. L., & Pao Q.,1996, Observations of field line resonances, auroral arcs, and auroral vortex structures, J. Geophys. Res., 101, 17373.

Samson, J. C., Rankin R., & Tikhonchuk V. T., 2003, Optical signatures of auroral arcs produced by field line resonances: comparison with satellite observations and modeling, Annales Geophysicae, 21, 933.

Schmidt, R. O., 1979, Multiple emitter location and signal parameter estimation, in Proc. RADC Spectrum Est. Workshop, Rome, NY, 243.

Schmidt, R. O., 1979, A signal subspace approach to multiple emitter location and parameter estimation, Ph. D. dissertation, Stanford Univ., Stanford, CA.

Schmidt, R. O., 1986, Multiple emitter location and signal parameter estimation, IEEE Treans. on Antennas and Propagation, Vol. 34, 276.

Schweppe, F. C., 1968, Sensor array data processing for multiple signal sources, IEEE Trans. Inform. Theory, Vol. IT-14, 294.

Shan, T. J., Wax, M., and Kailath, T., 1985, On spatial smoothing for directions of arrival estimation of coherent signals, IEEE Trans. on Acoustics, Speech and Signal Processing, ASSp33(4), 806.

Soubaras, R., 2000, 3-D projection filtering for noise attenuation and interpolation: 70th Annual Internat. Mtg., Soc. Expl. Geophys., Expanded Abstracts, session SP 6.7.

Southwood, D. J., 1974, Some features of field line resonances in the magnetosphere, Space Sci. Rev., 22, 483.

Stix, T. H., 1992, *Waves in Plasma*, AIP

Taylor, C. C., 1977, *Pronciple Component and Factor Analysis, The Analysis of Survey Data*, Vol. I, *Exploring Data Structures*, C. A. ÒMuricheartaigh and C. Payne, eds., John Wiley, New York.

Trickett, S. R., 2003, *F-xy* eigenimage noise suppression, Geophysics, **68**, 751.

Ulrych, T. J., Levy, S., Oldenburg, D. W., and Jones, I. F., 1983, Application of the Karhunen-Loève Transformation in reflection seismology, 53rd Ann. Internat. Mtg., Soc. Expl., Geophys., Expanded Abstracts, 323.

Ulrych, T. J., Freire, S. L. M, and Siston, P., 1988, Eigenimage Processing of Seismic Sections, 58th Ann. Internat. Mtg., Soc. Expl., Geophys., Expanded Abstracts, 1261.

Ulrych, T. J., Sacchi, M. D., and Freire, S. L. M, 1999, Eigenimage Processing of Seismic Sections, Covariance Analysis for Seismic Signal Processing, Geophysical Developement Series, No. 8, Edited by R. L. Kirlin and W. J. Done, Society of Exploration Geophysics.

Walker, A. D. M., Ruohoniemi, J. M., Baker, K. B., Greenwald, R. A., and Samson, J. C., 1992, Spatial and temporal behavior of ULF pulsations observed by the Goose Bay HF radar, J. Geophys. Res., vol. 97, no. A8, 12187.

Waters, C. L., Menk, F. W., and Fraser, B. J., 1994, Low latitude geomagnetic field line resonance: Experiment and modeling, J. Geophys. Res., vol. 99, no. A9, 17547.

Wax, M., and Kailath, T., 1983, Optimum localization of multiple sources by passive arrays, IEEE Trans. Acoust., Speech, Signal Processing, Vol. ASSP-31, 1210.

Wax, M., Shan, T., and Kailath, T., 1984, Spatio-temporal spectral analysis by eigenstructure methods, IEEE trans. Acoust., speech, Signal Processing, Vol. ASSP-32, 817.

Wiener, N., 1949, Extrapolation, Interpolation and Smoothing of Stationary Time Series, MIT Press, Cambridge, MA.

Yilmaz, O., 1999, Seismic Data Processing, Edited by S.M. Doherty, Society of Exploration Geophysicists, Tulsa, Oklahoma.

Ziesolleck, C. W. S., and McDiarmid, D. R., 1994, Auroral latitude Pc 5 field line resonances: Quantized frequencies, spatial characteristics, and diurnal variation, J. Geophys. Res., vol. 99, no. A4, 5817.